Technische Universität München

Fakultät für Chemie

Mechanistic studies of GID/CTLH E3 ubiquitin ligases

Jakub Chrustowicz

Vollständiger Abdruck der von der Fakultät für Chemie der Technischen Universität München zur Erlangung des akademischen Grades eines

Doktors der Naturwissenschaften (Dr. rer. nat.)

genehmigten Dissertation.

Vorsitzender:	Priv.-Doz. Dr. Gerd Gemmecker
Prüfer der Dissertation:	1. Hon.-Prof. Brenda Schulman, Ph.D.
	2. Prof. Dr. Michael Sattler
	3. Prof. Ivan Đikić, Ph.D.

Die Dissertation wurde am 23.11.2021 bei der Technischen Universität München eingereicht und durch die Fakultät für Chemie am 04.02.2022 angenommen.

ABSTRACT

The integrative structural, biochemical, and cell biology data revealed mechanistic principles of substrate targeting by evolutionarily conserved GID/CTLH E3 ubiquitin ligases. The pliable substrate receptors adapt their conformations to recognize various N-terminal peptide/degron sequences, whereas the chelator-like supramolecular assembly of a catalytically active E3 ligase core configures multi-pronged targeting of oligomeric substrates. The revealed principles provide a conceptual framework for understanding the emerging complexity of the GID E3 ligase family.

Table of Contents

1. Introduction

1.1. Discovery of the ubiquitin field

Change is an inherent element of life that triggers evolution but also poses a challenge to living organisms. In a highly dynamic environment, the survival of every living cell is dependent on its ability to constantly remodel its proteome to regulate metabolic processes and maintain homeostasis. Although the concept of continuous synthesis and degradation of proteins is a well-established paradigm of modern biology, it started to be appreciated only 80 years ago, when protein constituents of the body were shown to be extensively turned over [1, 2].

The realization of a dynamic state of the proteome has been substantiated by the discovery of the lysosome [3, 4], which, at that time, was considered the primary site of intracellular proteostasis [1]. Subsequently, a series of Nobel Prize-winning studies led by Hershko and Ciechanover concluded several years of research indicating that selective degradation of most cellular proteins follows a non-lysosomal pathway [1]. By studying the cell-free proteolytic system from rabbit reticulocytes, they have uncovered an energy-dependent process of protein degradation that is mediated by modification of target substrates with a small heat-stable protein [5-8], later identified as ubiquitin [9, 10]. A few years later, the physiological significance of protein ubiquitylation as a destruction signal has been demonstrated in the Varshavsky's lab by linking inactivation of one of the enzymes in the ubiquitin conjugation cascade to accumulation of normally short-lived proteins in a cell [11, 12]. Finally, characterization of a gigantic ATP-dependent protease degrading ubiquitylated substrates, the 26S proteasome, concluded the dissection of the major cellular proteolytic pathway, known as the ubiquitin-proteasome system (UPS) [13, 14].

After the discovery of the UPS, it has become evident that covalent conjugation of ubiquitin to proteins, or in some cases lipids [15] or even sugars [16], is one of their most prevalent post-translational modifications (PTMs) involved in nearly every aspect of eukaryotic cell biology. Beyond serving as a destruction signal, ubiquitylation regulates numerous non-proteolytic processes, such as interaction of substrates with other macromolecules, their cellular localization, and activity [17]. Moreover, ubiquitin has become a founding member of a large family of small posttranslational modifiers that share the conserved ubiquitin fold, like SUMO or NEDD8, called the ubiquitin-like proteins (UBLs) [18].

1.2. The ubiquitin code

Ubiquitin is a small 76-amino acid protein whose sequence is almost absolutely conserved across eukaryotes [19]. The structure of ubiquitin is highly compact, with a core adopting the β-grasp fold, wherein a five-stranded β-sheet essentially "grasps" a central α-helix [20] (Fig. 1). The globular core features several hydrophobic patches mediating interactions with other proteins containing ubiquitin-binding domains [21]. Aside from the folded domain, ubiquitin has a flexible C-terminal tail, which ends with a characteristic Gly-Gly motif required for substrate modification.

The C-terminal carboxyl group of ubiquitin is most commonly linked to a protein substrate via an isopeptide bond with an ε-amine group of a lysine sidechain (Fig. 1), but the conjugation of ubiquitin to an N-terminal α-amine group, hydroxyl groups of Ser and Thr, and a thiol group of Cys has also been reported [22-24]. Although attachment of a single ubiquitin molecule may significantly change substrate properties, proteins are often decorated with polyubiquitin chains, in which ubiquitin moieties are linked to each other through one of their seven lysine residues (K6, K11, K27, K29, K33, K48, and K63) or a free N-terminus [19] (Fig. 1). Since the linkage type determines the relative orientation of ubiquitin moieties in a chain, different chain types have various topologies and properties. Moreover, ubiquitin polymers can be further diversified by their modifications with numerous PTMs, such as phosphates, acetyl groups, or even other UBLs [25, 26]. Recognition of ubiquitylation patterns by specific ubiquitin-binding domains translates ubiquitin signals into various cellular outcomes, e.g., binding of proteins modified with K48- and K11-linked polyubiquitin chains by ubiquitin receptors of the 26S proteasome recruits them for degradation.

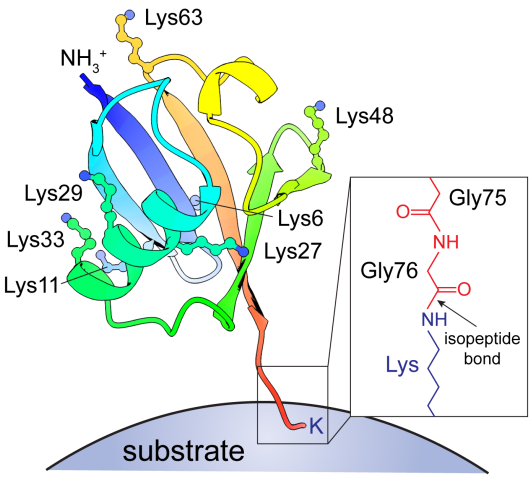

Figure 1. Structural features of ubiquitin conjugation

Ubiquitin (PDB ID: 1UBQ, colored rainbow from the N- (blue) to C-terminus (red)) is conjugated to substrates via an isopeptide linkage. Then, one or more of its seven lysines or an N-terminal amine group (marked NH_3^+) can serve as an acceptor for subsequent ubiquitin molecules to form polyubiquitin chains of various topologies.

Since the downstream effect of ubiquitylation is specified by the type of a polyubiquitin linkage, a multitude of ubiquitin signals have been referred to as the "ubiquitin code" [19]. Due to the proteinaceous nature of ubiquitin and its ability to form a countless number of chain types, the ubiquitin code has a potential to "encode" a far greater amount of information than all other known PTMs.

1.3. Machinery of ubiquitin conjugation

1.3.1. Ubiquitylation cascade

Unlike post-translational modification of proteins with small chemical groups, which typically involves the activity of a single enzyme, ubiquitylation is a result of a multistep enzymatic cascade comprised of concerted action of three distinct players [5, 8] (Fig. 2). At the apex of the pathway, one of the two ubiquitin-activating enzymes (E1) consumes ATP to form a high-energy thioester bond (denoted '~' hereafter) between its active site cysteine and the ubiquitin's C-terminus [27]. Subsequently, the activated ubiquitin is handed over to the active site cysteine of the second enzyme in the cascade, the ubiquitin-conjugating enzyme (E2), by thioesterification [28]. Although humans possess around 40 distinct E2s, they all have a conserved catalytic core adopting the same fold, termed the UBC domain. This universal domain harbors the active site Cys, as well as residues promoting catalysis and non-covalent interactions with other constituents of the pathway. E2s not only carry ubiquitin but often specify the type of polyubiquitin chains synthesized on substrates. Finally, one of over 600 ubiquitin ligases (E3s) mediates the last step of ubiquitin transfer by interacting with both the E2~ubiquitin (E2~Ub) conjugate and a target protein [29]. Since E3s recruit substrates for ubiquitylation, they confer substrate specificity to the ubiquitin system. The unique pairing between E2s and E3s ensures modification of correct substrates with desired ubiquitin signals.

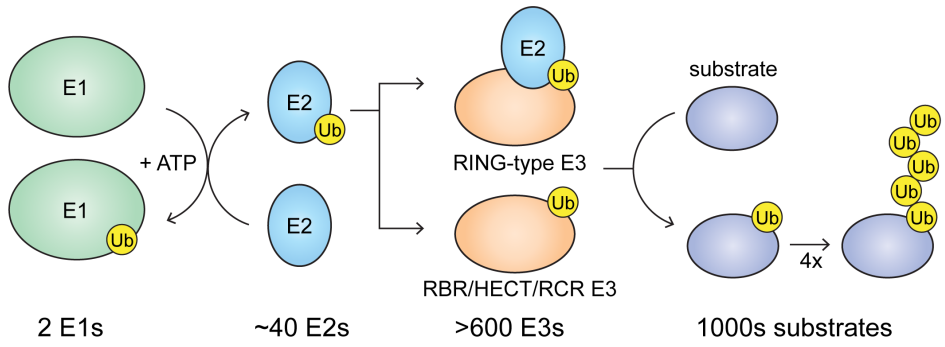

Figure 2. Schematic of ubiquitin conjugation

Covalent attachment of ubiquitin (Ub) to substrates involves the action of E1 Ub-activating enzymes, E2 Ub-conjugating enzymes, and E3 Ub ligases. The iterative cycles of Ub transfer may result in the synthesis of polyubiquitin chains.

1.3.2. Classification of E3 ligases

Ubiquitin ligases constitute the most numerous and structurally variable group of enzymes in the ubiquitylation cascade [23]. Despite their tremendous diversity, all E3s employ one of the four characterized ubiquitin transfer mechanisms [30]. The bulk of E3 ligases, referred to as the RING-type E3s, catalyze a direct transfer of ubiquitin to the substrate. Devoid of a catalytic cysteine, they do not form a thioester intermediate but rather induce proximity between the substrate's lysine and the E2~Ub catalytic center. In contrast, HECT-type E3s first conjugate ubiquitin from E2~Ub to their own catalytic Cys and only then transfer it to target proteins. These two mechanisms are amalgamated in RBR (RING-IBR-RING) ubiquitin ligases, which, similar to HECT-type E3s, form E3~Ub intermediates, but the transfer of ubiquitin to their catalytic Cys is mediated by the RING domain. Recently, the RING-Cys-Relay (RCR) ubiquitin transfer mechanism has been discovered, wherein ubiquitin is shuttled between two catalytic Cys of an E3 [9, 31]. Finally, E3 ligases falling into two distinct classes, such as RING- and RBR-type, can work together in a superassembly [32, 33], thus extending the mechanistic diversity and flexibility of the ubiquitin-conjugating machinery.

1.3.3. E2~Ub priming by the RING domain

Since E1- and E3-binding sites of E2s partially overlap, the charged E2~Ub has to dissociate from E1 before being engaged in a complex with E3 [34]. Therefore, between these two spatially separated events, E2~Ub conjugates carrying high-energy thioester bonds must co-exist with thousands of proteins in a crowded environment of the cell. To prevent unproductive and non-selective ubiquitin transfer, E2~Ub on its own is relatively inactive towards nucleophilic attack of the substrate's amine groups and becomes activated only after binding to E3 [28].

For the vast majority of E3 ligases, recruitment and activation of E2~Ub is carried out by their RING domain, which coordinates two zinc ions in a characteristic cross-braced configuration [30]. RING domains function in various structural contexts – while some work as monomers, many RINGs have to dimerize to be active or even be embedded in large multi-protein E3 ligase complexes, such as the anaphase-promoting complex/cyclosome (APC/C) or a family of cullin-RING ligases (CRLs). NMR experiments and several crystal structures of stable E2~Ub derivatives bound to RING domains revealed the molecular mechanism of RING-mediated E2~Ub activation [35]. When not bound to E3, E2~Ub samples an ensemble of largely 'open' conformations, with no or minimal interactions between ubiquitin and the E2 (Fig. 3A). Binding of E2~Ub to E3 induces adoption of a 'closed' conformation, wherein ubiquitin is folded back on the UBC domain of E2, with its C-terminal tail positioned along the E2's active site groove (Fig. 3B). In the closed conformation, E2~Ub is poised for ubiquitin transfer thanks

to E2 residues promoting catalysis, including activation and proper positioning of an incoming lysine amine for nucleophilic attack. In addition to this allosteric mechanism, many E2-RING E3 pairs have additional features that contribute to catalysis, such as domains enhancing protein-protein interactions or facilitating the synthesis of specific polyubiquitin chains.

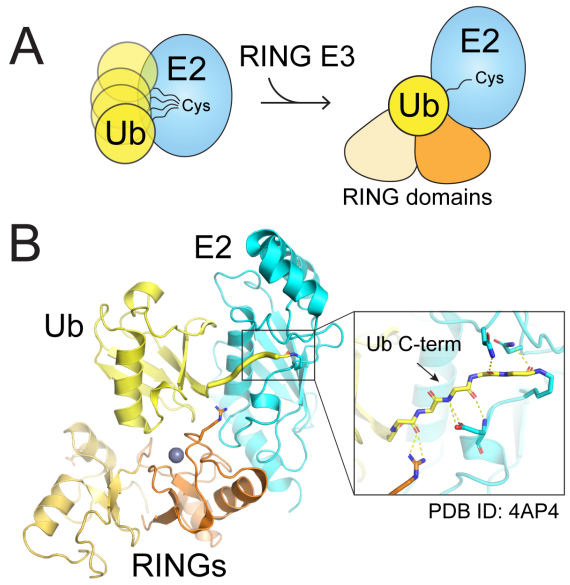

Figure 3. RING-mediated activation of the E2~Ub conjugate

A. Binding of E2~Ub to the RING domain primes it for catalysis by stabilizing its closed conformation.

B. Structural model of the primed E2~Ub conformation (PDB ID: 4AP4). In the closed conformation, ubiquitin establishes extensive contacts with both E2 and the heterodimeric RING domain, which position its C-terminus along the E2 active site groove.

1.3.4. Substrate recognition through terminal degrons

Apart from recruitment and priming of cognate E2~Ub intermediates, another essential functionality of E3 ligases is to selectively recruit ubiquitylation targets. The specificity of ubiquitylation relies on recognizing typically short and disordered sequence motifs within substrates called ‘degrons’ [36] by corresponding E3 ligases referred to as ‘recognins’ [37]. Whereas many degrons are located in the middle of a protein, termini of proteins are especially well-suited for harboring diverse degron motifs since they are usually accessible, disordered, and subject to less evolutionary constraints to preserve the 3D structure of a protein than its internal parts [38]. Indeed, the first identified determinants of substrate degradation were located at extreme N-termini of proteins. In the seminal study carried out in the Varshavsky’s lab, cellular half-time of model substrates was related to the identity of their N-terminal residues, a mechanism commonly known as the N-degron pathway (initially termed the N-end rule) [39].

The N-degron pathway has its roots in bacteria, which employ an adaptor protein ClpS to recognize proteins bearing N-terminal degradation signals and deliver them directly to the AAA+ protease in a ubiquitylation-independent manner [40]. Evolution has diversified the N-terminal proteolytic system, giving rise to several branches of the eukaryotic N-degron pathway that render all 20 amino acids destabilizing in specific cognate sequence

contexts [41]. The most extensively studied, and the first to be discovered, has been the Arg/N-degron pathway, which targets unmodified N-termini initiating with basic (Arg, Lys, His) and hydrophobic (Trp, Leu, Phe, Tyr, Ile) residues through the UBR family of E3s [42]. Another major branch of the eukaryotic degradation pathway recognizes N-termini modified with an acetyl group (the Ac/N-degron pathway) [43]. Recently, C-terminal regions of proteins have been identified to harbor degradation signals conceptually analogous to N-degrons, thus completing the discovery of terminal degrons [38, 44, 45].

Although ubiquitylation of many substrates is regulated by the availability or activity of a corresponding recognin, cellular proteins can also be converted into ubiquitin ligase targets by conditional activation of pro-degrons. One way to generate viable E3-binding signals involves the action of proteases, which can process either an extreme N-terminus of proteins or cleave internally, exposing a cryptic N- and/or C-degron [42]. Alternatively, protein N-termini can be enzymatically modified. Apart from N-terminal acetylation, which affects ~80-90% of proteins in a human cell [46, 47] and activates the Ac/N-degron substrates, the composition of an N-terminus is frequently modified by deamidation and non-ribosomal conjugation of amino acids. The latter two mechanisms are responsible for channeling proteins to the Arg/N-degron pathway.

1.4. GID E3s – the family of evolutionarily conserved ubiquitin ligases

1.4.1. Metabolic regulation as a model to investigate ubiquitin targeting of diverse substrates

E3 ligases constitute the most abundant group of enzymes in the ubiquitylation cascade, reflecting the diversity of ubiquitylation targets. First, E3 substrates adopt various quaternary structures, which determine their global properties, such as dimensions, the number of degrons and the constellation of ubiquitylation sites. Although most cellular proteins oligomerize, the understanding of strategies employed by E3s to efficiently target oligomeric substrates remains rudimentary. Second, E3 ligase substrates harbor different degrons and thus often, to target a collection of proteins destined for degradation at a given environmental condition, a single substrate receptor evolved to recognize a range of degron sequences. However, the extent of substrate receptor versatility, as well as its mechanistic basis, is a largely unexplored concept.

A process that can serve as a model to fill the gap in our understanding of substrate targeting by ubiquitin ligases is the regulation of metabolic pathways in response to changes in the internal and external environment of the cell. The flux of metabolites through these

pathways relies on activities of enzymes that typically oligomerize to acquire sophisticated regulatory properties, such as allosteric control or cooperative substrate binding [48]. One of the mechanisms orchestrating metabolic fluxes relies on instantaneous modulation of activities of existing metabolic enzymes through various means, such as post-translational modification or allosteric inhibition [49]. A more long-term mode of metabolic control involves changes in the global level of enzymes by altering the relative rates of their expression and UPS-dependent degradation.

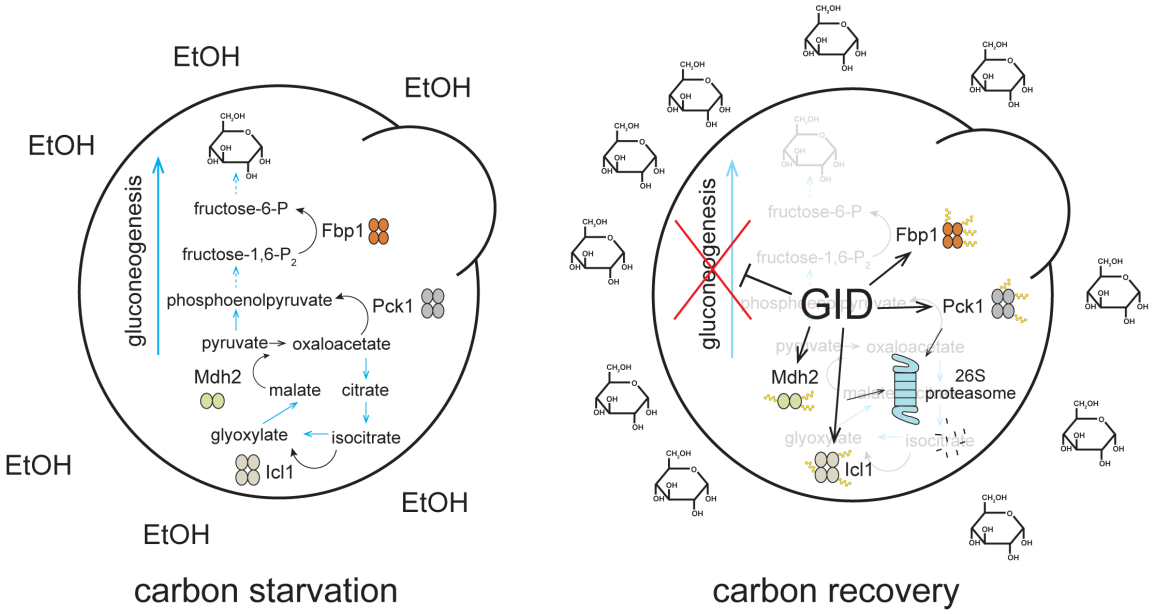

Figure 4. Ubiquitin-mediated catabolite inactivation by GID

During the recovery of yeast from carbon stress, i.e. growth on non-fermentable carbon sources such as ethanol (EtOH), gluconeogenesis has to be terminated by a multifaceted mechanism called catabolite inactivation. On top of other means of inhibition, gluconeogenic enzymes Fbp1, Mdh2, Pck1, and Icl1 are polyubiquitylated by a multi-subunit E3 ligase called GID, which induces their proteasomal degradation. The dashed arrows represent several enzymatic steps.

A classic example of metabolic rewiring that encompasses all of the aforementioned mechanisms is the acclimation of budding yeast, *S. cerevisiae*, to fluctuations in glucose availability. Like all unicellular microorganisms, yeasts have evolved to utilize available nutrients optimally and survive under various, often stressful environmental conditions [50]. When grown in a rich environment, yeasts employ glucose as a preferred energy and carbon source [51]. In the absence of sugars, they need to resort to non-fermentable carbon sources, such as ethanol or acetate. Moreover, sugar-starved yeasts synthesize glucose through gluconeogenesis to provide essential metabolic building blocks for anabolic processes (Fig. 4). After glucose replenishment, gluconeogenesis becomes superfluous and has to be terminated to save cellular energy. On top of transcriptional repression of a rate-limiting gluconeogenic

enzyme fructose-1,6-bisphosphatase (Fbp1), the restored glucose availability triggers its allosteric inhibition, repressive phosphorylation, and, finally, turnover – a phenomenon called catabolite inactivation [52, 53]. An E3 ligase that mediates degradation of Fbp1 and other pivotal gluconeogenic enzymes – malate dehydrogenase (Mdh2), isocitrate lyase (Icl1), and phosphoenolpyruvate carboxykinase 1 (Pck1) – is known as GID, reflecting its mutations rendering yeast **g**lucose-**i**nduced degradation **d**eficient.

1.4.2. Architecture of GID E3

The discovery of GID E3 dates back to 1998 when the group of Dieter Wolf performed the first yeast genetic screen to identify mutants impairing glucose-induced degradation of Fbp1 [54]. In conjunction with several later studies, they have characterized nine genes affecting Fbp1 turnover: *GID1, GID2, GID4, GID5, GID7, GID8,* and *GID9* that encode proteins assembling into a multi-subunit GID E3 complex [55-57]; *GID3*, encoding an E2 enzyme Ubc8 [58]; and *GID6*, whose product Ubp14 is a deubiquitylating enzyme responsible for the disassembly of polyubiquitin chains before proteasomal degradation [55, 59]. Notably, the newly discovered GID possessed all hallmark features of a RING-type E3 ligase – degenerated RING domains harbored by Gid2 and Gid9 that activate Ubc8~ubiquitin [56, 60], and a substrate recognition component Gid4 (denoted “yGid4” for yeast Gid4 hereafter) [61].

21 years after its discovery, a combination of cryoelectron microscopy (cryoEM), biochemistry, and yeast genetics delivered first mechanistic insights into GID-mediated catalysis [62]. The obtained structures revealed a modular core assembly of GID termed GID^{SR4} (where SR4 refers to the substrate receptor yGid4). The clamp-like GID^{SR4} fastens ubiquitylation substrates between its two jaws – yGid4 recruiting disordered degrons, and Ubc8~Ub poised for ubiquitin transfer to the substrate’s lysine (Fig. 5A). The jaws of the clamp are kept at an appropriate orientation and distance by interacting with the scaffold comprised of Gid1, Gid8, and Gid5. Gid1 and Gid8 form an interdigitated base of the scaffold projecting their CTLH-CRA^N protein-protein interaction domains in the opposite directions (Fig. 5B). The CTLH-CRA^N domain of Gid8 binds the corresponding domain in the Gid2-Gid9 catalytic module. Gid5, in turn, contains multiple armadillo repeats that adopt a helical solenoid structure. Whereas the N-terminal domain of Gid5 anchors it to the complex by binding the Gid1-Gid8 platform, the C-terminal domain forms a concave surface accommodating the globular substrate receptor.

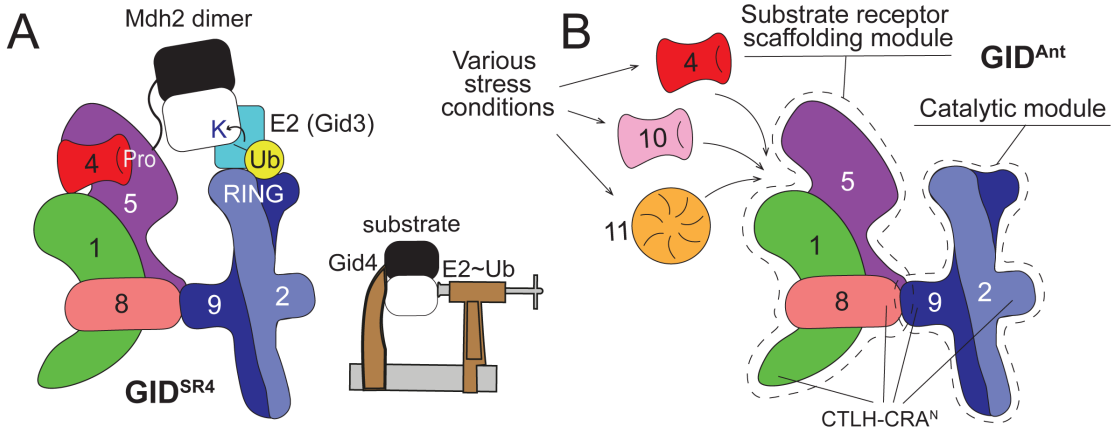

Figure 5. The assembly of GID

A. Cartoon of GID^{SR4} "clamping" its dimeric substrate Mdh2 between the substrate receptor yGid4 and the RING-Ubc8~Ub catalytic center

B. Cartoon of the anticipatory GID^{Ant} complex that is activated by association with various stress-induced substrate receptors. Intermodular connections are mediated by CTLH-CRA^{N} domains located at the edge of each module.

The structure of GID^{SR4} has shed light on glucose-mediated regulation of GID activity. Glucose starvation triggers expression of the anticipatory inactive complex (GID^{Ant}), which lacks a substrate receptor but is poised to an ensuing future shift of conditions (Fig. 5B). Glycolytic switch induces expression of yGid4 that binds and activates the complex towards gluconeogenic substrates. After glucose recovery, when the activity of GID is no longer needed, yGid4 is degraded in a GID E3-dependent manner, indicating a negative feedback loop [56, 63].

The function of GID is not limited to catabolite inactivation. The extended functionality of GID has become evident by the identification of two alternative substrate receptors: a yGid4 homolog – Gid10 (referred to as yGid10 hereafter) [62, 64], and Gid11 (yGid11 hereafter) [65]. Whereas, much as yGid4, incorporation of yGid10 and yGid11 into the complex relies on interactions with Gid5, their expression is induced by distinct environmental perturbations, such as hyperosmotic stress, heat shock, as well as carbon, nitrogen, and amino acid starvation [62, 64, 65]. GID is thus not a singular complex but rather a family of related complexes with conditionally expressed swappable substrate receptors (Fig. 5B). Therefore, energy expenses related to the production of an inactive molecular machine in the absence of stress are likely offset by bestowing yeasts with the ability to quickly respond to various perturbations and survive in an ever-changing environment.

1.4.3. N-degron recognition by GID substrate receptors

A unifying feature of gluconeogenic GID substrates is the presence of intrinsically disordered stretches of several N-terminal residues that are recognized by yGid4 and, therefore, serve as N-degrons [54, 61]. Together with cognate downstream sequences, the principal determinant mediating binding of these N-degrons to yGid4 is N-terminal Pro, which becomes natively exposed upon co-translational removal of initiator Met1 by methionine aminopeptidases [66] and, in the case of Pck1, consecutive exoproteolytic removal of Ser2 [67]. Since Pro is neither acetylated nor recognized by the Arg/N-degron pathway, the identification of yGid4-mediated targeting of gluconeogenic substrates gave rise to a novel branch of N-degron pathways termed the Pro/N-degron pathway [61]. As revealed by a structural study of its human homolog (denoted hGid4 hereafter), the substrate-binding domain of Gid4 is uniquely suited to recognize terminal degrons, as its β-barrel domain together with four flexible hairpin loops surrounding its entrance form a deep and narrow tunnel accommodating several N-terminal residues [68].

Although initially characterized as a Pro/N-degron E3, the specificity of GID extends well beyond Pro-initiating sequences. For example, hGid4 was recently shown to recognize peptides initiated with non-Pro hydrophobic residues [69], and yGid10, which is structurally homologous to yGid4, can bind both Pro and various non-Pro N-termini [64]. Furthermore, the recently identified yGid11, which is thought to adopt a β-propeller structure, is specific towards proteins with N-terminal Thr [65]. An extended specificity of GID, together with an increasing number of characterized substrate receptors, suggests that the realm of GID substrates, and hence its physiological significance, is only beginning to emerge.

1.4.4. Evolutionary conservation of GID

All subunits of the yeast GID have their homologs in higher eukaryotes, namely RANBP9/10 (Gid1), TWA1 (Gid8), ARMC8 (Gid5), hGid4, RMND5A (Gid2), MAEA (Gid9), and WDR26/MKLN1 (Gid7), which form a complex with intrinsic E3 ligase activity collaborating with its cognate E2 enzyme Ube2H [70-72]. Since, like their yeast homologs, most of these proteins contain the CTLH domain mediating inter-subunit interactions [57], the resulting complex has been referred to as the CTLH E3 [73].

Although the substrates of CTLH have not been unambiguously identified, many studies implicated it in the multitude of physiologically fundamental processes. For example, in leguminous plants, CTLH controls the root nodule formation essential for nitrogen fixation [74]. In animals, the role of CTLH E3 begins already at the onset of embryogenesis, as it targets a translation repressor complex during the maternal-to-zygotic transition in fly embryos

[75, 76] and is indispensable for proper brain formation in frogs [77]. Later in development, CTLH plays a vital role in erythropoiesis, specifically in its final stages related to nuclear condensation and enucleation [78, 79]. Moreover, while CTLH does not directly target human gluconeogenic enzymes [70], the metabolic function of CTLH seems to be evolutionarily preserved as it regulates renal gluconeogenesis [80], glycolysis [81] and targets a major metabolic status sensor AMPK [82]. Finally, since CTLH affects cell proliferation [70, 83] and migration [84] its dysregulation may potentially lead to cancer. Indeed, many CTLH subunits are known to be overexpressed in various human tumors [85].

2. Methods

2.1 Protein preparation

Plasmid preparation and mutagenesis

The genes encoding subunits and substrates of yeast GID were amplified from *S. cerevisiae* BY4741 genomic DNA. All genes coding for human CTLH subunits were obtained from the MPIB cDNA library, except for hGid4, whose gene was codon-optimized for the *E. coli* expression system and ordered from GeneArt (Thermo Fisher Scientific). The sequences of all expressed proteins correspond to the canonical UniProt sequences, besides ARMC8, for which isoform 2 (missing the residues 2-15 of the canonical sequence) was used based on the prior literature [73].

The genes for bacterial expression were cloned into pGEX or pRSF vectors using the Gibson assembly method [86]. To express GID/CTLH complexes in insect cells, the genes encoding their single subunits were firstly cloned into a pLIB vector and then combined into a single baculovirus expression construct using the biGBac assembly method [87]. Mutagenesis was performed with the QuickChange protocol (Stratagene). All final constructs were verified by DNA sequencing.

Bacterial protein expression and purification

All bacterial expressions were carried out in *E. coli* BL21 (DE3) pRIL. To set up protein expression, 1 L of a Terrific Broth medium [88] was inoculated with 10 mL of bacterial pre-culture and incubated at 37°C and 180 rpm until OD_{600} of 0.6. Then, the culture was cooled-down down to 18°C and mixed with 0.4 mM IPTG to induce protein expression. After overnight incubation, bacterial cultures were harvested by centrifugation, resuspended in the lysis buffer (50 mM Tris pH 8, 200 mM NaCl, 5 mM DTT, and 1 mM PMSF for GST-tagged proteins or 50 mM Tris pH 8, 200 mM NaCl, 5 mM β-mercaptoethanol, 10 mM imidazole and 1 mM PMSF for 6xHis-tagged proteins) and disrupted by sonication. The cleared lysates were incubated with either GST-affinity (Cytiva) or 6xHis-affinity Ni-NTA (Sigma) resin for 1 hour at 4°C. Subsequently, the resin was extensively washed with buffer containing 50 mM HEPES pH 7.5, 200 mM NaCl, 5 mM DTT or 5 mM β-mercaptoethanol and proteins were eluted. Most proteins expressed as GST fusions were incubated with TEV or HRV-3C protease overnight to cleave off the GST tag. After tag cleavage, proteins destined for crystal trials were additionally purified with anion exchange chromatography using HiTrap Q column (Cytiva). Final purification of all proteins was performed with size exclusion chromatography (SEC) in the final buffer containing 50 mM HEPES pH 7.5, 200 mM NaCl and 1 mM or 5 mM DTT (for assays and crystal trials,

respectively), or 0.5 mM TCEP (for ITC binding assay). Additionally, pass-back over GST-affinity resin was performed to remove the uncleaved GST-fusion protein and free GST.

To purify FDITGFSW-Fbp1$^{(\Delta 1\text{-}9)}$, whose bulky N-terminus may interfere with the cleavage of initiator methionine during protein synthesis [66], it was expressed as a GST-SUMO fusion. After GST-affinity chromatography, N-terminal Phe was exposed by cleavage of the GST-SUMO tag with SENP2 protease, which was then removed by pass-back over the GST-affinity resin after final SEC.

Untagged WT ubiquitin used for *in vitro* assays was purified with the glacial acetic acid method [89], followed by gravity S column cation exchange chromatography (GE Healthcare) and SEC.

Insect cell protein expression and purification

The GID and CTLH complexes were expressed in insect cells with a Twin-Strep-tag fused to the C-terminus of Gid8/TWA1. All bacmids were generated in *E. coli* DH10Bac emBacY and used for transfection of Sf9 insect cells to generate baculovirus variants carrying the respective protein-coding sequences. For protein expression, Hi5 insect cells were infected with the recombinant baculoviruses and grown for 60 to 72 hours in EX-CELL 420 Serum-Free Medium at 27°C. Insect cell cultures were harvested by centrifugation, resuspended in the lysis buffer (50 mM Tris pH 8, 200 mM NaCl, 5 mM DTT, 10 μg/ml leupeptin, 20 μg/ml aprotinin, EDTA-free Complete protease inhibitor tablet (Roche, 1 tablet per 50 ml of buffer) and 1 mM PMSF) and disrupted by sonication. Proteins were purified from the cleared lysates with Strep-Tactin-affinity (IBA Lifesciences) chromatography, followed by anion exchange chromatography using a Mono Q column (Cytiva) and SEC in the final buffer containing 25 mM HEPES pH 7.5, 200 mM NaCl and 1 or 5 mM DTT for biochemical assays and cryoEM, respectively.

Fluorescent labeling of GID substrates for ubiquitylation assays

To monitor the progress of ubiquitylation reactions, the C-termini of GID substrates Mdh2, Fbp1 and Pck1 were fluorescently labeled with fluorescein in a reaction catalyzed by sortase A [90]. The labeling reaction was set up by mixing 50 μM substrate (C-terminally tagged with a sortag (LPETGG) and a 6xHis-tag), 250 μM fluorescent peptide (GGGGGFYVK-FAM) and 50 μM sortase A in the reaction buffer containing 50 mM Tris pH 8, 150 mM NaCl and 10 mM $CaCl_2$. After 30-minute incubation at room temperature, the reaction mix was passed through Ni-NTA resin to remove unreacted substrates, which carried a 6xHis tag. Further purification was done with SEC in the final buffer containing 50 mM HEPES pH 7.5, 200 mM NaCl and 1 mM DTT.

^{15}N labeling of hGid4

To label hGid4 (Δ1-115) with ^{15}N for the NMR experiment, it was expressed as N-terminal 6xHis fusion in a minimal medium containing $^{15}NH_4Cl$ as a sole nitrogen source. To start protein expression, 50 ml of a preculture was pelleted to get rid of the rich medium and resuspended in 1 L of the M9 medium (2 g glucose, 5 mg/ml thiamine chloride, 1 M $MgSO_4$, 1 M $CaCl_2$ and 1 g $^{15}NH_4Cl$) containing all essential ions and antibiotics. The cultures were grown at 37°C and 180 rpm until the OD_{600} of 0.6, cooled down to 23°C, mixed with 0.6 M IPTG to induce protein expression, and further grown overnight. 6xHis-^{15N}hGid4 was purified by 6xHis-affinity chromatography and SEC in the NMR buffer (25 mM phosphate buffer pH 7.8, 150 mM NaCl and 1 mM DTT).

2.2 Biochemical assays

2.2.1. *In vitro* activity assays

Multi-turnover ubiquitylation reactions with yeast GID

All ubiquitylation reactions were run at room temperature in the buffer containing 25 mM HEPES pH 7.5, 150 mM NaCl, 5 mM ATP and 10 mM $MgCl_2$. The reactions were quenched with SDS-PAGE loading dye at indicated timepoints, and reaction substrates and products were separated by SDS-PAGE. To monitor ubiquitylation of fluorescently labeled proteins, the gels were scanned with a Typhoon imager (GE Healthcare).

To test the influence of Gid7 and Gid4 on the GID-mediated ubiquitylation of Fbp1, Mdh2 and Pck1, they were expressed in *E. coli* and exogenously added to the reaction with the anticipatory GID^{Ant} complex (Gid 1-8-5-2-9). The reactions were initiated by mixing 0.2 μM E1 Uba1, 1 μM Ubc8-6xHis, 0.5 μM GID^{Ant}, 0 or 1 μM Gid4, 0 or 2 μM Gid7, 1 μM fluorescent substrate and 20 μM ubiquitin (WT or its lysineless, all Lys>Arg mutant).

The ability of the high-affinity yGid4- and yGid10-binding sequences to promote substrate recruitment for ubiquitylation was probed in a reaction with model peptide substrates C-terminally labeled with fluorescein. The peptides were comprised of N-terminal binding motifs connected to a single acceptor lysine by a flexible linker whose length was designed based on the distance between the substrate receptor and the catalytic center in the cryoEM structure of GID^{SR4}. The reaction mixes contained 0.2 μM E1 Uba1, 1 μM E2 Ubc8-6xHis, 0.5 μM E3 GID^{Ant}, 20 μM ubiquitin, 1 μM yGid4 (Δ1-115) or yGid10 (Δ1-56) and 1 μM peptide substrate.

To analyze the effect of degron strength on ubiquitylation of Fbp1 and Mdh2, we performed assays with their WT and degron-swapped versions (Fbp1$^{Mdh2\ degron}$ and Mdh2$^{Fbp1\ degron}$) by mixing 0.2 μM E1 Uba1, 1 μM E2 Ubc8-6xHis, 1 μM E3 GID^{Ant}, 2 μM yGid4 (Δ1-115),

0.5 μM fluorescent substrates and 20 μM ubiquitin. Similarly, we exchanged the native Fbp1 degron with the high-affinity yGid4-binding motif to test if it promotes ubiquitylation in the context of a full-length substrate. The reaction mix contained 0.2 μM E1 Uba1, 1 μM E2 Ubc8-6xHis, 0.1 μM GID^{SR4} (Gid 1-8-5-2-9-4) or Chelator-GID^{SR4} (Gid 1-8-5-2-9-4-7), 1 μM WT or mutant Fbp1-FAM and 20 μM ubiquitin.

The preferred Fbp1 ubiquitylation sites determined by mass-spectrometry were validated by mutating them to arginines and performing ubiquitylation assays with the resultant Fbp1 variants. The reactions contained 0.2 μM E1 Uba1, 1 μM Ubc8-6xHis, 0.5 μM GID^{Ant}, 1 μM Gid4, 2 μM Gid7, 1 μM Fbp1-6xHis (WT or target Lys>Arg mutants) and 20 μM ubiquitin (WT or the lysineless version). The analogous experiment was performed to analyze the identified ubiquitylation sites in Mdh2, except it was run with 0.1 μM purified Chelator-GID^{SR4} instead of the GID^{Ant}+Gid4+Gid7 mixture. The reaction substrates and products were immunoblotted with primary mouse anti-6xHis and secondary HRP-conjugated anti-mouse antibodies and visualized by chemiluminescence.

Multi-turnover ubiquitylation reactions with human CTLH

Due to a lack of *in vitro*-validated substrates of human CTLH, we employed a 30-residue fluorescent model peptide with the N-terminal hGid4-binding motif PGLW connected to a single lysine with a linker whose length was designed based on the structure of $CTLH^{SR4}$ (as described above for the yeast GID). The established assay served to probe the mechanistic features of the CTLH complex.

The structure-based mode of hGid4 incorporation into $CTLH^{SR4}$ was validated in a reaction initiated by mixing 0.2 μM Uba1, 2 μM Ube2H-6xHis, 1 μM RANBP9-TWA1-ARMC8-RMND5A-MAEA complex, 1 μM WT or mutant hGid4 (Δ1-99), 0.5 μM fluorescent model peptide substrate and 20 μM ubiquitin. The mutants of hGid4 were designed based on its interaction points with ARMC8 and RANBP9 in the model of the $CTLH^{SR4}$ SRS module. Similarly, the catalytic mechanism of CTLH was tested with point mutations of the catalytic subunits RMND5A and MAEA designed based on their homology models and sequence alignments to well-characterized RING domains. The reactions contained 0.2 μM Uba1, 2 μM Ube2H-6xHis, 1 μM RANBP9-TWA1-ARMC8-RMND5A-MAEA complex (containing either WT or mutant RMND5A or MAEA), 1 μM hGid4 (Δ1-99), 0.5 μM fluorescent model peptide substrate and 20 μM ubiquitin.

To characterize the type of ubiquitin chain formed by $CTLH^{SR4}$ in conjunction with Ube2H, the assay was run with single-lysine Ub mutants, in which all but one lysine were mutated to arginines. The reaction contained 0.2 μM Uba1, 2 μM Ube2H-6xHis, 1 μM RANBP9-TWA1-

ARMC8-RMND5A-MAEA, 1 μM hGid4 (Δ1-99), 0.5 μM fluorescent peptide substrate and 20 μM ubiquitin (WT, lysineless or single-lysine mutant).

Substrate-independent discharge assays

To test whether the point mutations of RMND5A and MAEA affect their intrinsic ability to activate E2~Ub, we performed substrate-independent assays that monitor discharge of ubiquitin to unanchored lysine in solution. First, Ube2H was loaded with ubiquitin by mixing 0.5 μM Uba1, 10 μM Ube2H-6xHis, 30 μM ubiquitin, 2.5 mM $MgCl_2$ and 1 mM ATP. After 15-minute incubation at room temperature, the loading reaction was quenched with 50 mM EDTA and combined with an equal volume of the discharge-initiating mixture containing 1 μM RANBP9-TWA1-ARMC8-RMND5A-MAEA (containing either WT or mutant RMND5A or MAEA) and 25 μM lysine pH 8.0. Reactions were quenched with a non-reducing SDS-PAGE loading dye, run on SDS-PAGE and visualized with Coomassie.

Qualitative competitive ubiquitylation assay to test avid substrate binding

To probe avid capture of Mdh2 by Chelator-GID^{SR4}, we competed ubiquitylation of the fluorescently labeled Mdh2-FAM by the monovalent and bivalent form of GID with two types of unlabeled competitors – a monodentate peptide comprised of Mdh2 N-terminal sequence PHSVTPSIEQDSLK and a bidentate unlabeled full-length Mdh2. The reactions were initiated by mixing 0.2 μM Uba1, 1 μM Ubc8-6xHis, 0.5 μM E3 GID^{SR4}, 0 or 2 μM Gid7 (WT or its N-terminal deletion mutant Δ1-284 that does not support the higher-order GID assembly), 0.5 μM Mdh2-FAM, 20 μM unlabeled competitor and 20 μM ubiquitin.

Quantitative competitive ubiquitylation assay to compare yGid4 binders

Since yGid4 is not amenable to biophysical characterization, we rank-ordered the phage-display identified sequences and the native GID substrate degrons based on their ability to inhibit ubiquitylation of Mdh2 by GID^{SR4}. Reactions were started by addition of 20 μM ubiquitin to the mixture of 0.2 μM E1 Uba1, 1 μM E2 Ubc8-6xHis, 0.5 μM E3 GID^{Ant}, 1 μM yGid4 (Δ1-115), 0.25 μM Mdh2-FAM and increasing concentrations of unlabeled peptide competitors. All reactions were run for 3 minutes so that their velocity was still in the linear range. Reaction substrates and products visualized by a fluorescent scan of SDS-PAGE were quantified with ImageQuant (GE Healthcare). The ratios of ubiquitylated Mdh2 fractions in the presence and absence of an inhibitor were plotted against peptide concentration. Fitting the data to [inhibitor] vs. response model in GraphPad Prism yielded the values of half-maximal inhibitory concentration (IC50).

Determination of kinetic parameters of substrate ubiquitylation by GID E3 ligases

To determine the values of a Michaelis-Menten constant (K_m), we titrated E3 (GID^{SR4} or Chelator-GID^{SR4}) at constant concentrations of fluorescently labeled substrates (WT and degron-swapped versions of Fbp1 and Mdh2), which were kept below K_m (0.5 and 0.1 μM for reactions with GID^{SR4} and Chelator-GID^{SR4}, respectively). All reactions were quenched before their rates of product formation exceeded a linear range. Reactions with GID^{SR4} comprised 0.2 μM Uba1, 1 μM Ubc8, 0.25-10 μM GID^{SR4}, 0.5 μM substrate and 20 μM ubiquitin. For Chelator-GID^{SR4}, the reaction mixes contained 0.2 μM Uba1, 1 μM Ubc8, 0.03-1 μM Chelator-GID^{SR4}, 0.1 μM substrate and 20 μM ubiquitin. Fractions of ubiquitylated substrates (quantified with ImageQuant (GE Healthcare)) were plotted as a function of E3 concentration in GraphPad Prism and fit to the Michaelis-Menten equation to estimate K_m.

To calculate the values of a turnover number k_{cat}, time course assays were performed with the ratios of [E3]:K_m and [substrate]:K_m kept the same for all substrates and both E3 versions (2.7 and 0.4, respectively). The fraction of ubiquitylated substrates was plotted in GraphPad Prism as a function of time and reaction rates were estimated by linear regression. The initial velocities were calculated using the following equation: $V_0 = rate \cdot [substrate]$. Then, V_{max} was estimated using a modified form of the Michaelis-Menten equation: $V_{max} = \frac{V_0 \cdot (K_m + [substrate])}{[substrate]}$. Finally, k_{cat} was determined by dividing V_{max} by the E3 concentration: $k_{cat} = \frac{V_{max}}{[E3]}$.

2.2.2. Binding assays

Qualitative binding test to probe binding of hGid4 mutants to CTLH

All hGid4 mutants assessed in ubiquitylation assays were also tested for their ability to bind the CTLH complex. RANBP9-TWA1-ARMC8-RMND5A-MAEA (tagged with a Twin-Strep tag at TWA1 C-terminus) was mixed with a 10-fold molar excess of WT and mutant versions of hGid4 (Δ1-99) in a buffer containing 25 mM HEPES pH 7.5, 150 mM NaCl and 1 mM DTT. After 30 minutes, the mixture was incubated with Strep-affinity resin for 1 hour at 4°C with gentle agitation. After extensive wash of the resin, the proteins were eluted and analyzed with Coomassie-stained SDS-PAGE.

Isothermal titration calorimetry (ITC)

To quantify binding of the phage-display identified sequences by hGid4 (Δ1-115) and yGid10 (Δ1-56), we employed ITC. All peptides were dissolved in the buffer used for final gel filtration of the analyzed substrate receptors containing 25 mM HEPES pH 7.5, 150 mM NaCl and 0.5 mM TCEP. Peptide concentrations were measured by absorbance at 280 nm, which was possible owing to the presence of a single tryptophan residue in all peptides (appended

at peptides' C-termini if not present in the original sequences). Binding experiments were carried out with the MicroCal PEAQ-ITC instrument (Malvern Panalytical) at 25°C with the reference power set to 10 µcal/s. Peptides were titrated to hGid4 or yGid10 as 19 x 2 µl injections, with 4 s injection time and 150 s equilibration time between the injections. Concentrations of peptides and substrate receptors were adjusted based on the estimated affinities. Raw ITC data were analyzed using the One-Set-of-Sites binding model (Malvern Panalytical) to determine a dissociation constant (K_D) and binding stoichiometry (N).

Fluorescence polarization (FP) assays

A direct FP assay was set up by mixing 20 nM fluorescent peptides (an hGid4-binding motif PGLWKS-FAM and a non-binding control GGGGRHDS(P)GLDS(P)MKDEE-FAM) with a 2-fold dilution series of hGid4 (Δ1-115) in the FP buffer containing 25 mM Tris pH 8.0, 150 mM NaCl, 0.5 mM DTT. The mixed samples were transferred to a 384-well flat bottom black plate (Greiner) and scanned with a CLARIOstar microplate reader (BMG LABTECH) to measure fluorescence polarization. For each run, the gain was calibrated against a well containing 20 nM fluorescent peptides in the FP buffer. The data were fit to one-site binding model in GraphPad Prism to determine the K_D value.

To compare binding of low-affinity ligands to hGid4, we performed an FP assay in a competitive format. Based on the plot from the hGid4 titration experiment, we identified hGid4 concentration at which the FP signal reached ~60% saturation. Next, a 2-fold dilution series of unlabeled competitors was prepared in the FP buffer and mixed with 6.8 µM hGid4 and 20 nM PGLWKS-FAM. After 5-minute incubation, the measurement was performed as described above. The data were plotted relative to the FP signal in the absence of an inhibitor (100% FP signal) as a function of log(inhibitor concentration) and analyzed with log(inhibitor) vs. response model to determine IC50 values.

2.3 Structural studies

2.3.1 Structure determination by cryoEM

Sample preparation and imaging

The complexes analyzed by cryoEM were prepared in the following way:

1. Chelator-GID^{SR4}: Gid1, Gid2, Gid5, Gid8-2xS, Gid9 co-expressed in insect cells; bacterially expressed yGid4 (Δ1-116) and Gid7 added before final SEC

2. Fbp1-bound Chelator-GID^{SR4}: Gid1, Gid2, Gid5, Gid8-2xS, Gid9 co-expressed in insect cells; bacterially expressed yGid4 (Δ1-116) and Gid7 added before final SEC; Fbp1-6xHis added directly before cryoEM grids preparation

3. CTLH-WDR26 subcomplex (SA and SRS modules): RANBP9, TWA1, 2xS-ARMC8, WDR26, YPEL5 co-expressed in insect cells; bacterially expressed hGid4 (Δ1-99) added before final SEC

4. CTLH-MKLN1 subcomplex (SA and SRS modules): RANBP9, TWA1-2xS, ARMC8, MKLN1 co-expressed in insect cells; bacterially expressed hGid4 (Δ1-99) added before final SEC

5. $CTLH^{SR4}$: RANBP9, TWA1-2xS, ARMC8, RMND5A, MAEA co-expressed in insect cells; bacterially expressed hGid4 (Δ1-99) added before final SEC

CryoEM grids were prepared using Vitrobot Mark IV (Thermo Fisher Scientific) operated at 4°C and 100% humidity. 3.5 µl of freshly purified proteins at 0.3-0.5 mg/ml were applied to glow-discharged holey carbon R1.2/1.3 grids with 200 copper mesh (Quantifoil). Grids were blotted with Whatman no. 1 filter paper (blot time: 3 s, blot force: 3) and vitrified by plunging into liquid ethane.

Screening of cryoEM grids and low-resolution data collection was performed with 200 kV Talos Arctica or Glacios transmission electron microscopes (Thermo Fisher Scientific) equipped with a Falcon III (Thermo Fisher Scientific) or K2 (Gatan) direct electron detector, respectively. High-resolution datasets were collected with a 300 kV Titan Krios (Thermo Fisher Scientific) microscope equipped with a post-column GIF and a K3 Summit direct electron detector (Gatan) operating in a counting mode. The EPU (Thermo Fisher Scientific) or SerialEM [91] software was used to automate data collection.

Data processing

CryoEM data collected with Titan Krios were pre-processed on the fly with the Focus software [92], which automatically discarded poor-quality images. All the subsequent stages of data processing were carried out with Relion [93-95]. For all datasets, the collected frames were first motion-corrected with MotionCorr2 [96] and subjected to estimation of contrast transfer function parameters with Gctf [97]. Auto-picking of particles was performed with Gautomatch (https://www2.mrc-lmb.cam.ac.uk/download/gautomatch-053/) and, for most datasets, it was aided by provision of low-resolution templates. The picked particles were extracted and subjected to either several rounds of 2D classification, followed by a 3D classification or submitted directly to a masked 3D classification. The chosen subset of particles was auto-refined without and with a mask. To improve map quality, 3D classification without particle alignment was performed and a class having the most complete features was selected and subjected to a final round of auto-refinement. The additional steps involved in the processing of individual high-resolution datasets are summarized below.

High-resolution maps of yeast Chelator-GID modules were obtained from the Fbp1-bound Chelator-GID^{SR4} dataset. For Cat and SA modules, the map of the entire complex was first auto-refined with the C2 symmetry and masks covering each of its halves were created. Then, the signal for each half was separately subtracted and the resulting semi-elliptical particles were merged and aligned by auto-refinement, which doubled the particle number. The SRS module was masked out, and focused 3D classification without particle alignment was performed separately for Cat and SA modules. After one more round of 3D classifications without particle alignment with a higher value of a regularization parameter (T=50 or 100), the CTF parameters were refined and particles were subjected to the final round of local auto-refinement with lower angular sampling.

To obtain the high-resolution map of the human CTLH^{SR4} SRS module (RANBP9-TWA1-ARMC8-hGid4), the entire CTLH^{SR4} complex was first auto-refined and the density corresponding to the catalytic module (RMND5A-MAEA) was masked out due to its mobility relative to the rest of the complex. To visualize high-resolution features of the region spanning RANBP9$^{LisH-CRAC}$-TWA1 as well as the N- and C-termini of ARMC8, several rounds of focused 3D classifications with masks over these regions were carried out. The final auto-refinement was preceded by refinement of CTF parameters.

All maps were post-processed by automatic B-factor weighting and high-resolution noise substitution in Relion. The refined maps of the Chelator-GID^{SR4} SA and CTLH^{SR4} SRS modules were post-processed with DeepEMhancer [98] to facilitate model building. The estimated resolutions of all reconstructions are based on the gold-standard Fourier Shell Correlation (FSC) at 0.143 criterion.

Model building and refinement

All atomic models were built in Coot [99, 100] and subjected to real-space refinement in PHENIX [101-103]. Structure visualization was carried out with Chimera [104], ChimeraX [105] and Pymol (https://pymol.org/2/).

To build an atomic model of the Chelator-GID^{SR4} SA module, the coordinates of Gid1 and Gid8 from the structure of GID^{SR4} (PDB ID:6SWY) were docked in the generated map and the missing or differing parts, such as Gid1 CTLH-CRA^{N}, were built manually. Manual building of Gid7 was aided by secondary structure predictions for the helical LisH-CTLH-CRA domains and the homology model of its β-propeller generated by Phyre^{2} [106].

For the SRS module of CTLH^{SR4}, we first tried automatic model building with Buccaneer [107], which successfully yielded the model of the majority of ARMC8. The crystal structure of hGid4 (PDB ID: 6CDC) was docked into the EM map and extended by manual building of its N- and C-termini. Similarly, the crystal structure of RANBP9 SPRY domain (PDB ID: 5JI7) was fit into

the map and served as a starting point for manual building of its downstream region. Manual building of TWA1 was guided by fitting parts of its homology model generated by SWISS-MODEL [108] and secondary structure prediction obtained from the Phyre^2 server [106].

2.3.1 Structure determination by X-ray crystallography

To gain molecular insight into the recognition of high-affinity peptide binders by hGid4 and yGid10, we determined their crystal structures. All crystal trays were set up in the MPIB Crystallization Facility with a Phoenix crystallization pipetting robot (Art Robbins Instruments). Crystals were grown at room temperature by a vapor diffusion method in a sitting drop format.

For crystals of hGid4, 9.2 mg/mL hGid4 (Δ1-120, Δ294-300) was mixed with 600 μM FDVSWFMG peptide and incubated on ice for 1 h before setting up trays. Final crystals were obtained in 1.1 M sodium malonate, 0.3% Jeffamine ED-2001 pH 7, and 0.1 M HEPES pH 7 and cryoprotected using a mixture of 20% glycerol and 20% ethylene glycol.

Similarly, to obtain yGid10 (Δ1-64, Δ285-292) crystals, it was concentrated to 10 mg/mL and mixed with the peptide FWLPANLW to achieve final protein and peptide concentrations of 262 μM and 760 μM, respectively (~3-fold molar excess of the peptide). Final crystals were obtained in 0.1 M MES pH 6.9 and cryoprotected using 20% ethylene glycol.

X-ray diffraction datasets were recorded at X10SA beamline, Swiss Light Source (SLS) in Villingen, Switzerland. The diffraction data were indexed, integrated, and scaled using the XDS package. Phasing was performed by molecular replacement with PHASER module integrated into the PHENIX software suite [101-103] using previous structures as initial models (PDB ID: 6CDC for hGid4 and PDB ID: 7NS3 (the model of yGid4) for yGid10). Atomic models were built in Coot [99, 100] and refined by real-space refinement in PHENIX.

3. Publications

My PhD work aimed at gaining structural and mechanistic insights into the evolutionarily conserved GID E3 ligase. The projects were highly collaborative and gave rise to two co-first-author publications.

3.1. GID E3 ligase supramolecular chelate assembly configures multipronged ubiquitin targeting of an oligomeric metabolic enzyme.

(Sherpa and Chrustowicz, et al. Molecular Cell. 2021)

Mechanistic dissection of GID^{SR4} and its nutrient-dependent activation [62] has not only shed light on the molecular principles of stress anticipation but also raised new questions regarding complex assembly and additional requirements for targeting oligomeric GID substrates. Perplexingly, GID^{SR4} does not include Gid7, which is known to be a peripheral subunit of GID directly binding Gid1 [56, 57] and is indispensable for glucose-induced degradation of Fbp1 [55]. The essentiality of Gid7 is difficult to reconcile with the fact that GID^{SR4} already contains all hallmark features of a RING-type E3 ligase and promotes robust *in vitro* ubiquitylation of Mdh2 [62]. In Sherpa and Chrustowicz et al. 2021 [109], we set out to fill a gap in our understanding of Fbp1 targeting and discovered a novel form of GID that includes Gid7. CryoEM, biochemistry, and yeast genetics revealed an unprecedented 1.5 MDa chelator-like assembly of an E3 ligase that encapsulates tetrameric Fbp1. Such an arrangement promotes avid Fbp1 binding, simultaneous ubiquitylation of its multiple protomers, and specific targeting of lysines nearby regions important for Fbp1 metabolic activity. The principle of supramolecular assembly has been conserved in the human CTLH complex whose catalytic core is elaborated by two orthologs of yeast Gid7 to form distinct higher-order structures. The findings of our study might be generalizable to other E3 ligases and even other PTM enzymes that target oligomeric proteins.

Apart from designing experiments and preparing the manuscript, my contributions to this project involved: *in vitro* reconstitution of the yeast and human GID complexes, performing *in vitro* biochemical assays (Fig. 1AB, 5A, S6), determination of low-resolution cryoEM structures of apo and Fbp1-bound Chelator-GID^{SR4} as well as WDR26- and MKLN1-mediated CTLH subcomplexes, processing high-resolution cryoEM datasets of Chelator-GID^{SR4} and $CTLH^{SR4}$, building atomic models of Chelator-GID^{SR4} SA module (PDB ID: 7NSB) and $CTLH^{SR4}$ SRS module (PDB ID: 7NSC).

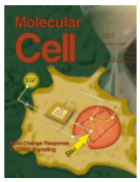

GID E3 ligase supramolecular chelate assembly configures multipronged ubiquitin targeting of an oligomeric metabolic enzyme

Author:
Dawafuti Sherpa,Jakub Chrustowicz,Shuai Qiao,Christine R. Langlois,Laura A. Hehl,Karthik Varma Gottemukkala,Fynn M. Hansen,Ozge Karayel,Susanne von Gronau,J. Rajan Prabu,Matthias Mann,Arno F. Alpi,Brenda A. Schulman

Publication: Molecular Cell

Publisher: Elsevier

Date: 3 June 2021

Molecular Cell

Article

GID E3 ligase supramolecular chelate assembly configures multipronged ubiquitin targeting of an oligomeric metabolic enzyme

Graphical abstract

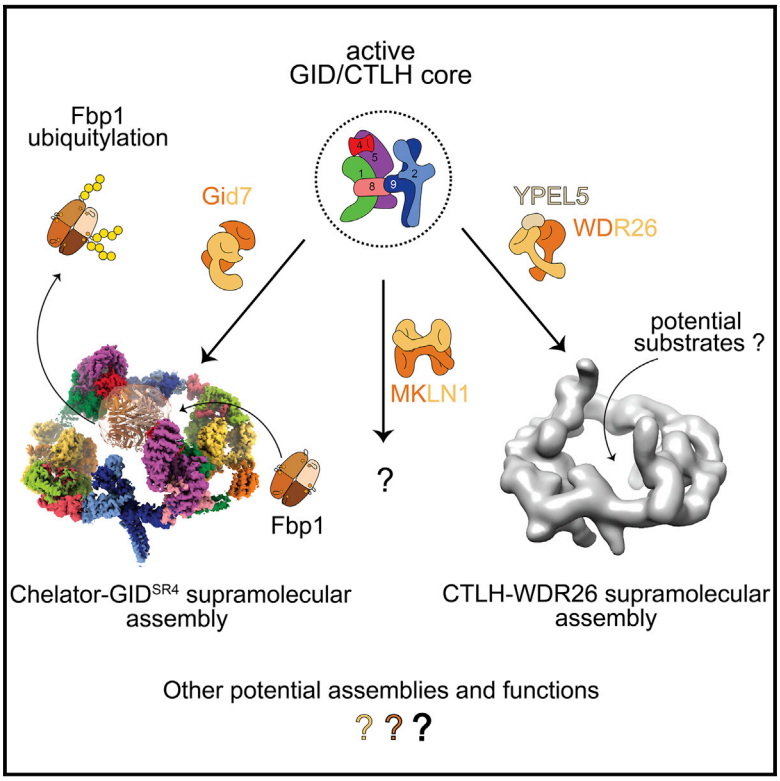

Highlights

- GID E3 ligase assembly resembles a behemoth organometallic supramolecular chelate
- Multipronged targeting of oligomeric structure and metabolic function of substrate
- Yeast Gid7, human WDR26, and MKLN1 mediate supramolecular assembly of GID/CTLH E3s
- Human CTLH E3 structural and mechanistic features parallel yeast GID E3 ligase

Authors

Dawafuti Sherpa, Jakub Chrustowicz, Shuai Qiao, ..., Matthias Mann, Arno F. Alpi, Brenda A. Schulman

Correspondence

schulman@biochem.mpg.de

In brief

Structural, biochemical, and cellular data reveal supramolecular assembly of yeast GID E3 ligase. GID E3 forms a chelate-like structure tailored to target the oligomeric structure and metabolic function of the gluconeogenic enzyme substrate Fbp1. The orthologous human CTLH E3 contains a GID-like core assembly that forms a supramolecular chelate and utilizes a GID-like ubiquitin ligase mechanism.

Sherpa et al., 2021, Molecular Cell *81*, 2445–2459
June 3, 2021
https://doi.org/10.1016/j.molcel.2021.03.025

CellPress

Molecular Cell

CellPress
OPEN ACCESS

Article

GID E3 ligase supramolecular chelate assembly configures multipronged ubiquitin targeting of an oligomeric metabolic enzyme

Dawafuti Sherpa,[1,3] Jakub Chrustowicz,[1,3] Shuai Qiao,[1] Christine R. Langlois,[1] Laura A. Hehl,[1] Karthik Varma Gottemukkala,[1] Fynn M. Hansen,[2] Ozge Karayel,[2] Susanne von Gronau,[1] J. Rajan Prabu,[1] Matthias Mann,[2] Arno F. Alpi,[1] and Brenda A. Schulman[1,4,*]

[1]Department of Molecular Machines and Signaling, Max Planck Institute of Biochemistry, Martinsried 82152, Germany
[2]Department of Proteomics and Signal Transduction, Max Planck Institute of Biochemistry, Martinsried 82152, Germany
[3]These authors contributed equally
[4]Lead contact
*Correspondence: schulman@biochem.mpg.de
https://doi.org/10.1016/j.molcel.2021.03.025

SUMMARY

How are E3 ubiquitin ligases configured to match substrate quaternary structures? Here, by studying the yeast GID complex (mutation of which causes deficiency in glucose-induced degradation of gluconeogenic enzymes), we discover supramolecular chelate assembly as an E3 ligase strategy for targeting an oligomeric substrate. Cryoelectron microscopy (cryo-EM) structures show that, to bind the tetrameric substrate fructose-1,6-bisphosphatase (Fbp1), two minimally functional GID E3s assemble into the 20-protein Chelator-GID^{SR4}, which resembles an organometallic supramolecular chelate. The Chelator-GID^{SR4} assembly avidly binds multiple Fbp1 degrons so that multiple Fbp1 protomers are simultaneously ubiquitylated at lysines near the allosteric and substrate binding sites. Importantly, key structural and biochemical features, including capacity for supramolecular assembly, are preserved in the human ortholog, the CTLH E3. Based on our integrative structural, biochemical, and cell biological data, we propose that higher-order E3 ligase assembly generally enables multipronged targeting, capable of simultaneously incapacitating multiple protomers and functionalities of oligomeric substrates.

INTRODUCTION

Cells rapidly adapt their metabolic pathways in response to nutrient availability (Tu and McKnight, 2006; Zaman et al., 2008; Zhu and Thompson, 2019). Shifts in metabolic enzyme activities are achieved by regulation at every conceivable level. Metabolite-responsive transcriptional programs activate pathways that maximally use available nutrients and repress those rendered unnecessary or counterproductive. For oligomeric enzymes, catalytic activities are subject to metabolite-mediated allosteric control (Koshland, 1963a, 1963b; Monod et al., 1963). In eukaryotes, undesired metabolic activities are often terminated by ubiquitin-mediated degradation (Nakatsukasa et al., 2015).

Degradation is typically controlled by recognition of proteins as substrates of E3 ubiquitin (Ub) ligases. However, little is known about whether or how E3 ligases are specifically tailored for oligomeric assemblies of metabolic enzymes. One of the first identified targets of nutrient-dependent degradation, budding yeast fructose-1,6-bisphosphatase (Fbp1), is an oligomer (Chiang and Schekman, 1991). Fbp1 is a gluconeogenic enzyme essential for yeast growth on non-fermentable carbon sources. A shift from gluconeogenic to glycolytic conditions renders gluconeogenesis superfluous. Accordingly, Fbp1 activity and expression are curtailed (Gancedo, 1971; Schork et al., 1994a, 1994b, 1995). The switch to glycolytic conditions induces Ub-mediated degradation of Fbp1 and other gluconeogenic enzymes, including malate dehydrogenase (Mdh2) and phosphoenolpyruvate carboxykinase (Pck1), mediated by the multiprotein E3 ligase termed "GID"; yeast mutants of Gid subunits are glucose-induced-degradation deficient (Braun et al., 2011; Chiang and Schekman, 1991; Hämmerle et al., 1998; Menssen et al., 2012; Regelmann et al., 2003; Santt et al., 2008; Schork et al., 1994b, 1995). Although the GID E3 is conserved across eukaryotes and regulates important physiology (Lampert et al., 2018; Liu et al., 2020; Liu and Pfirrmann, 2019; Salemi et al., 2017), its regulation and targets are best characterized in budding yeast.

Much like well-studied multiprotein E3 ligases, such as anaphase-promoting complex/cyclosome (APC/C) or cullin-RING ligases, GID is not a singular complex—a core catalytic and scaffolding assembly is modulated by other subunits (Barford, 2020; Karayel et al., 2020; Liu and Pfirrmann, 2019; Melnykov et al., 2019; Qiao et al., 2020; Rusnac and Zheng, 2020; Watson et al., 2019). The constituents of various GID assemblies and how they achieve regulation are beginning to emerge. Previous structural studies have elucidated the core assembly and

recapitulated some GID regulation (Qiao et al., 2020). Briefly, a core inactive complex, GID^{Ant}, contains the heterodimeric E3 ligase RING and RING-like subunits (Gid2 and Gid9) and scaffold subunits (Gid1, Gid5, and Gid8). Coexpression of these subunits in insect cells enables purification of recombinant GID^{Ant} and systematic interrogation of GID functions. Within the GID^{Ant} scaffold, Gid5 can bind the structurally homologous, interchangeable substrate-binding receptors Gid4 and Gid10 (Karayel et al., 2020; Melnykov et al., 2019; Qiao et al., 2020). Of these, the molecular basis of substrate binding by Gid4 is well understood: glucose-induced incorporation of Gid4 into the GID E3 enables recognition of substrate "Pro/N-degron" motifs depending on an N-terminal proline (Chen et al., 2017; Dong et al., 2018; Hämmerle et al., 1998; Regelmann et al., 2003; Santt et al., 2008). Indeed, *in vitro*, adding Gid4 transforms GID^{Ant} into an active GID^{SR4} complex that collaborates with the cognate E2, Ubc8 (also known as Gid3) to ubiquitylate Mdh2, as explained by a structure of GID^{SR4} (Qiao et al., 2020). Mutations probing the GID^{SR4} structure also showed that this assembly is required for glucose-induced Fbp1 degradation *in vivo* (Qiao et al., 2020).

Perplexingly, despite the crucial role of Fbp1 in regulating gluconeogenesis, its ubiquitylation has not been reconstituted *in vitro* using defined GID E3 ligase components. *In vivo*, Fbp1 degradation depends on another protein, Gid7, which associates with other Gid subunits (Menssen et al., 2012; Regelmann et al., 2003; Santt et al., 2008). Gid7 is evolutionarily conserved across eukaryotes. Mammals even have two orthologs, WDR26 and MKLN1, which are subunits of the "CTLH" complex that corresponds to the yeast GID E3 (Boldt et al., 2016; Francis et al., 2013; Kobayashi et al., 2007; Lampert et al., 2018; Liu and Pfirrmann, 2019; Salemi et al., 2017). The CTLH E3, named for the preponderance of CTLH domains (in Gid1, Gid2, Gid7, Gid8, and Gid9 and their orthologs), has intrinsic E3 ligase activity, although Pro/N-degron substrates have not yet been identified despite human Gid4 binding this motif (Cao et al., 2020; Dong et al., 2018; Lampert et al., 2018; Liu et al., 2020; Liu and Pfirrmann, 2019; Maitland et al., 2019; Zavortink et al., 2020).

Here we reconstitute a minimal GID E3 ligase active toward Fbp1 by combining GID^{SR4} and Gid7. Cryoelectron microscopy (cryo-EM) reveals its structure as a 20-protein supramolecular chelate E3 ligase assembly specifically tailored for Fbp1's quaternary structure. Structural and biochemical data suggest that the human Gid7 orthologs likewise transform a GID^{SR4}-like E3 ligase core into higher-order assemblies. Our data reveal supramolecular chelate assembly of a pre-existing, functionally competent E3 ligase complex as a structural and functional principle to achieve multipronged Ub targeting tailored to an oligomeric substrate.

RESULTS

Reconstitution of Fbp1 ubiquitylation

Considering that the Gid7 protein, not visualized previously, is required for glucose-induced Fbp1 degradation *in vivo* (Regelmann et al., 2003), we tested its effect *in vitro*. Our assay setup probes modulation of the core recombinant GID^{Ant} assembly upon adding other purified components individually or in combination. First, adding Gid4 marginally stimulated Fbp1 ubiquitylation despite substantially potentiating ubiquitylation of Mdh2, another canonical Pro/N-degron substrate, and Pck1, whose recognition by the GID E3 remains elusive (Figure 1A). However, adding Gid7 together with Gid4 substantially increased Fbp1 ubiquitylation. Comparing reactions with wild-type (WT) Ub or a Ub version lacking lysines (K0Ub) that cannot form polyUb chains indicated that adding Gid7 increases substrate consumption, the number of modified Fbp1 sites, and the number of Ubs in polyUb chains (Figures 1A and 1B). Second, the remarkable activation upon addition of Gid7 was specific to Fbp1; effects on Pck1 were negligible, and effects on Mdh2 were nuanced in increasing polyUb chain length while attenuating the amount of Mdh2 molecules consumed in the assay (Figure 1A). Third, adding Gid7 actually suppressed intrinsic GID E3 ligase activity, as shown by effects on Ub transfer from a pre-formed Ubc8∼Ub intermediate to free lysine in solution (Figure S1A). Binding of Fbp1's degron per se is insufficient to overcome this inhibition because Gid7 likewise subdued ubiquitylation of a model peptide substrate in which Fbp1's degron sequence, PTLV, is connected to a lysine acceptor through an intervening flexible linker (Figure S1B).

To gain mechanistic insights, we quantified effects of including Gid7 in a chromatographically purified version of the E3 by performing enzyme kinetics. Compared with GID^{SR4}, a version of the E3 complex fully incorporating Gid7 displayed a relatively 10-fold lower Michaelis-Menten constant, K_m, for Fbp1 ubiquitylation and 10-fold increase in the reaction turnover number k_{cat} (Figures 1C, 1D, S1C, and S1D). Adding purified Gid7 to GID^{SR4} had similar effects (Figures 1C and S1C).

Consistent with the biochemical data, glucose-induced ubiquitylation of Fbp1 *in vivo* is impaired by Gid7 deletion (Figure 1E). To examine effects on degradation, we employed a promoter reference technique that monitors degradation of exogenously expressed proteins (here, C-terminally FLAG-tagged Fbp1, Mdh2, or Pck1) while normalizing for effects on expression (Chen et al., 2017; Oh et al., 2017). Our assay agreed with prior studies showing that glucose-induced degradation of Fbp1, Mdh2, and Pck1 depends on Gid4 (Chen et al., 2017; Qiao et al., 2020; Regelmann et al., 2003; Santt et al., 2008). However, Gid7 deletion substantially stabilized only Fbp1 (Figure 1F). This deficit in Fbp1 degradation upon Gid7 deletion was not rescued by Gid4 overexpression (Figure S1E). Also, quantitative mass spectrometry analyses of the yeast proteome confirmed that, of known gluconeogenic GID E3 substrates, Fbp1 was most affected by Gid7 deletion (Figure S1F).

A supramolecular Chelator-GID^{SR4} E3 assembly encapsulates the tetrameric Fbp1 substrate

To understand the mechanism of Fbp1 recognition by the GID E3, we purified an Fbp1-active recombinant complex and analyzed its structure by cryo-EM (Figures S2A and S4; Table S1). A 13-Å-resolution map of the assembly even without the substrate showed a remarkable GID E3 structure: an exterior oval supporting several inward-pointing globular domains. Strikingly, the longest exterior dimension of 305 Å is roughly comparable with that of a singly capped 26S proteasome, 1.3 times that of the multiprotein Fanconi anemia E3 ligase complex and 1.5 times that of APC/C (Figure 2A)

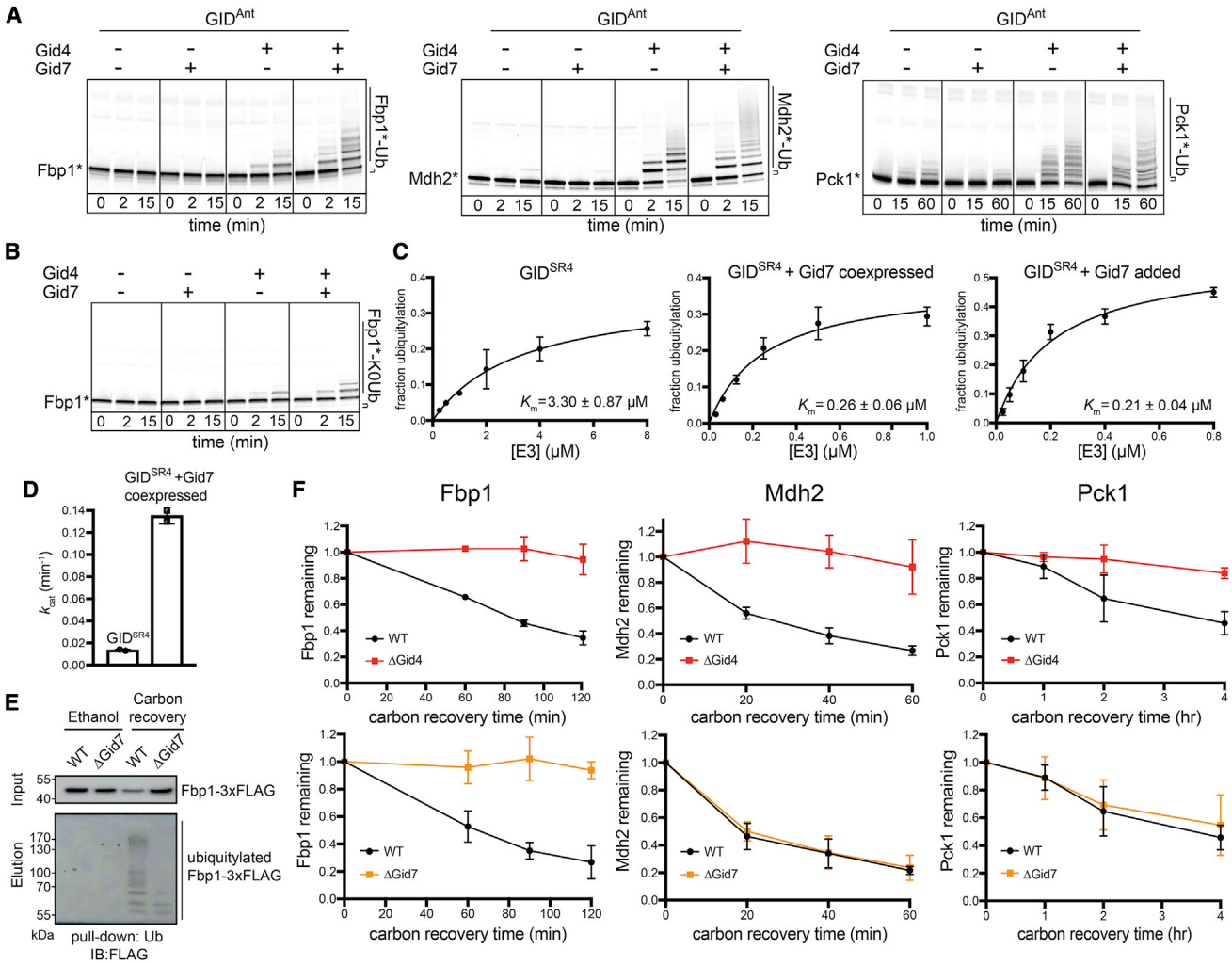

Figure 1. Fbp1 ubiquitylation and degradation require a distinct Gid7-containing GID E3 ligase

(A) Fluorescence scans of SDS-PAGE gels showing *in vitro* ubiquitylation assays. These assays test the roles of Gid4 and Gid7 in ubiquitylation of C-terminally fluorescently labeled Fbp1 (left), Mdh2 (center), and Pck1 (right). GID^{Ant} contains 2 protomers each of Gid1 and Gid8 and 1 of Gid2, Gid5, and Gid9. An asterisk indicates that substrates are fluorescently labeled.

(B) *In vitro* ubiquitylation assay as in (A) but performed with lysine-less Ub (K0Ub) to determine the number of Fbp1 ubiquitylation sites.

(C) Plots showing fraction of Fbp1 ubiquitylation as a function of concentration of GID^{SR4} (left) or its complex with Gid7 (center and right). K_m values were determined by fitting to the Michaelis-Menten equation. Error bars, SD (n = 2).

(D) Comparison of k_{cat} between GID^{SR4} and its complex with Gid7, determined from plots in Figure S1D. Error bars, SD (n = 2).

(E) Assessing *in vivo* ubiquitylation of Fbp1 (C-terminally 3×FLAG-tagged at the endogenous locus) under carbon starvation (ethanol) and after 2 h of carbon recovery in WT and ΔGid7 yeast strains. Following capture of ubiquitylated proteins with TUBEs (tandem ubiquitin binding entities), Fbp1-3×FLAG was visualized by anti-FLAG immunoblotting.

(F) Glucose-induced degradation *in vivo* of exogenously expressed substrates Fbp1 (left), Mdh2 (center), and Pck1 (right), quantified using the promoter reference technique. Substrate levels were quantified as the ratio of substrate detected relative to the level after switching from carbon starvation to carbon recovery conditions in WT, ΔGid4 (top panels), and ΔGid7 (bottom panels) strains. Points represent mean, and error bars represent SD ($n \geq 3$).

See also Figure S1.

(Brown et al., 2016; Chen et al., 2016; Haselbach et al., 2017; Lander et al., 2012; Schweitzer et al., 2016; Shakeel et al., 2019; Wehmer et al., 2017). Unlike these compact assemblies, however, this GID complex displays a behemoth hollow center with interior edges of 270 and 130 Å in the longest and shortest dimensions, respectively—larger than a cullin-RING ligase ubiquitylating a substrate (Baek et al., 2020).

The organization of the oval GID assembly was gleaned from comparison with cryo-EM maps of subcomplexes (Figure 2B; Table S1). Two copies of the previously defined GID^{SR4} structure (Qiao et al., 2020) fit in the large assembly. An additional Gid1-Gid8 subcomplex can be observed bound to GID^{SR4}. These duplicated Gid1 and Gid8 protomers are components of recombinant GID^{Ant} used for biochemical assays (Qiao et al., 2020) but

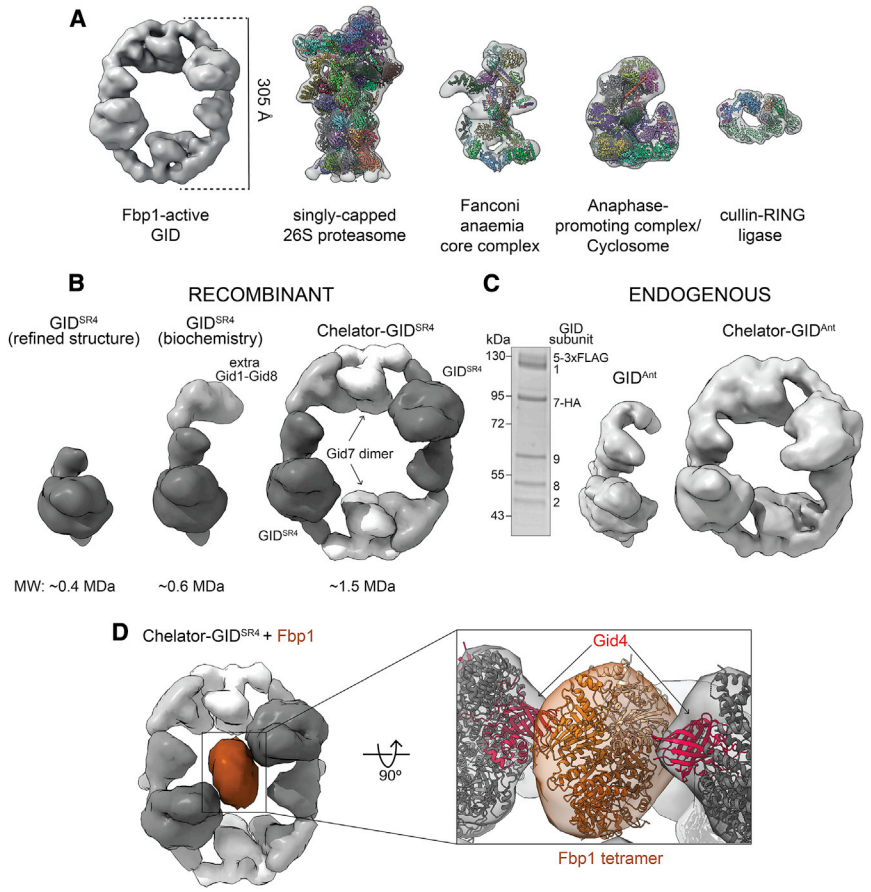

Figure 2. Multidentate capture of the Fbp1 tetramer by the Chelator-GID^{SR4} assembly

(A) Cryo-EM map of GID E3 active toward Fbp1 compared for scale with low-pass-filtered maps of the singly capped 26S proteasome (EMDB: EMD-3536; PDB: 5MPB), Fanconi anemia core complex (EMDB: EMD-10290; PDB: 6SRI), APC/C (EMDB: EMD-3433; PDB: 5L9T), and cullin-RING E3 ubiquitylation complex (EMDB: EMD-10585; PDB: 6TTU).

(B) Cryo-EM maps and molecular weights of recombinant GID assemblies. Structurally determined GID^{SR4} (left, low-pass-filtered, dark gray, EMDB: EMD 10327; PDB: 6SWY) is a stoichiometric complex of Gid1, Gid8, Gid5, Gid4, Gid2, and Gid9. The purification conditions used here include an additional Gid1-Gid8 subcomplex (gray) bound to GID^{SR4} (center, taken for the biochemical assays). The oval higher-order Chelator-GID^{SR4} assembly includes Gid7 dimers (right, white).

(C) Coomassie-stained SDS-PAGE (left) and cryo-EM maps of endogenous yeast GID^{Ant} (center) and Chelator-GID^{Ant} (right) assemblies (prepared by anti-FLAG immunoprecipitation of lysates from yeast with Gid5 3×FLAG tagged and Gid7 hemagglutinin (HA) tagged at their endogenous loci and grown under conditions when Gid4 is not induced).

(D) Cryo-EM map of Chelator-GID^{SR4} (gray) bound to the Fbp1 tetramer (brown). The close up shows 2 red Gid4 protomers (modeled from PDB: 6SWY) simultaneously contacting the docked Fbp1 crystal structure.

See also Figure S2 and Tables S1 and S2.

are not visible upon map refinement to high resolution. We interpreted the remaining density in the large oval GID assembly as Gid7 dimers, one at each vertex, given size exclusion chromatography-multi angle light scattering (SEC-MALS) data indicating that purified Gid7 dimerizes (Figure S2B). The data reveal a 1.5-MDa eicosameric GID assembly composed of 4 Gid1: 2 Gid2: 2 Gid4: 2 Gid5: 4 Gid7: 4 Gid8: 2 Gid9 protomers.

We sought to determine whether this GID assembly might be formed *in vivo*. Prior studies did (Santt et al., 2008) or did not (Qiao et al., 2020) observe Gid7 cosedimenting with other GID proteins in density gradients. This raised the possibility that, like the equally giant 26S proteasome, some subunits or regulatory partners may be prone to dissociation; for example, based on lysis conditions (Leggett et al., 2002). Thus, we examined sedimentation of a core subunit, Gid8 tagged at the endogenous locus, as a marker for a GID assembly because it cosediments with all other GID^{SR4} subunits even under relatively harsh lysis conditions (Qiao et al., 2020). Yeast lysates prepared by cryomilling were subjected to sucrose density gradient fractionation. Anti-FLAG immunoblotting showed Gid8 migrating at a lower molecular weight in a Gid7 deletion compared with the WT, irrespective of whether yeast was grown under carbon starvation or recovery in glucose, which induces GID E3 ligase activity (Figure S2C). Moreover, cryo-EM data of endogenous GID purified from yeast grown under carbon starvation yielded 3D reconstructions corresponding to the recombinant assemblies with and without Gid7 at 14.2- and 9.5-Å resolution, respectively (Figures 2C and S2D).

Why is the minimum E3 ligase for Fbp1 so gigantic and hollow? Given the substantial effect on K_m in our enzyme kinetics analyses, we hypothesized that such an assembly would form to accommodate the substrate. To characterize the substrate, we determined the crystal structure of yeast Fbp1, which confirmed its tetrameric assembly (Figures 2D and S2B; Table S2). We next resolved a cryo-EM structure with Fbp1 bound to the GID E3, which led to several conclusions (Figure 2D; Table S1). First, Fbp1 was readily docked in the center of the large GID E3 oval. Second, two Fbp1 edges approach the substrate binding Gid4 subunits within each GID^{SR4} on opposite sides of the oval. Third, the density attributed to Gid7 does not directly contact Fbp1 but connects two Fbp1-binding GID^{SR4} complexes. Thus, Gid7 activates GID E3 activity toward Fbp1 indirectly by driving supramolecular assembly.

The resultant GID assembly resembles an organometallic supramolecular chelate in which multiple giant organic molecules capture a much smaller ligand through multiple discrete points of contact. Thus, we call the giant oval complex "Chelator-GID^{SR4}" based on its supramolecular assembly in which two GID^{SR4} complexes simultaneously capture degrons displayed from two protomers in the tetrameric Fbp1 substrate.

CellPress
OPEN ACCESS

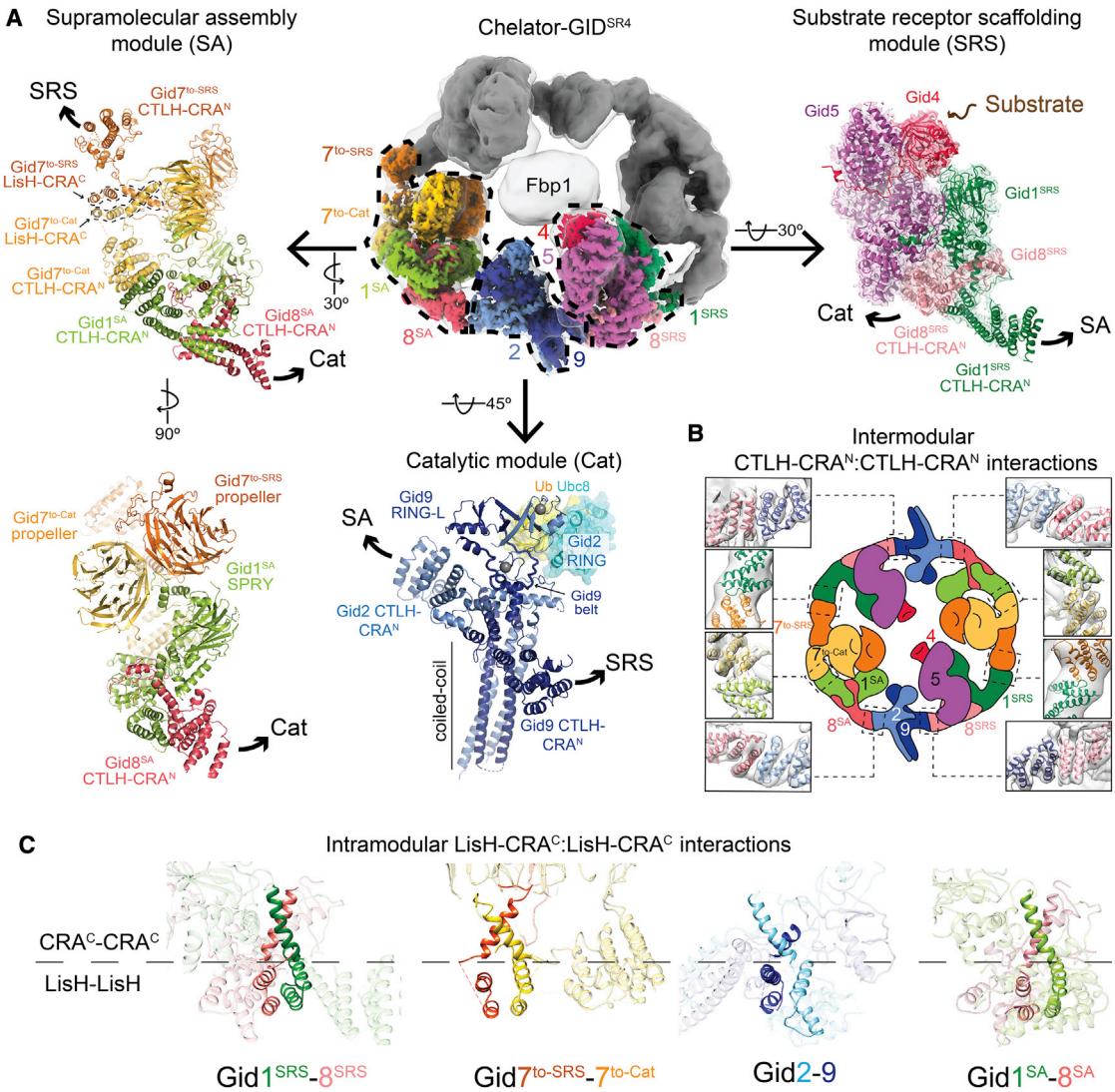

Figure 3. High-resolution details of Chelator-GID^{SR4} modular assembly

(A) Focused refined maps of the substrate receptor scaffolding (SRS), catalytic (Cat), and supramolecular assembly (SA) modules, colored according to subunit identity, fit in half of the overall map of Fbp1-bound Chelator-GID^{SR4} (top center). The GID^{SR4} structure (PDB: 6SWY) fits the SRS module (Gid1^{SRS}, dark green; Gid8^{SRS}, salmon; Gid5, purple; Gid4, red). A brown arrow points to Gid4's substrate binding site (top right). The Cat module comprises Gid2 (sky blue) and Gid9 (navy). Zinc ions are shown as gray spheres. Ubc8~Ub was modeled by aligning Gid2 RING with an E2~Ub-bound RING structure (PDB: 5H7S). The SA module comprises Gid1^{SA} (green), Gid8^{SA} (pink) and 2 Gid7 protomers, Gid7$^{to\text{-}Cat}$ (yellow), and Gid7$^{to\text{-}SRS}$ (orange) facing the Cat or SRS module, respectively. Superscript text refers to a module for a given Gid1 or Gid8 protomer. Arrows point to connected modules.

(B) Cartoon of Chelator-GID^{SR4} with close ups of intermodule CTLH-CRA^N:CTLH-CRA^N interactions fit into the map of Chelator-GID^{SR4} (gray).

(C) Intramodule LisH-CRA^C:LisH-CRA^C (solid ribbon) interactions in Chelator-GID^{SR4}.

See also Figures S3 and S4 and Table S1.

High-resolution structures of modules in Chelator-GID^{SR4}

A series of focused refinements enabled building atomic models of the three functionally distinct modules comprising Chelator-GID^{SR4} (Figures 3A, S2E, S3A, and S4; Table S1): (1) the substrate receptor scaffolding (SRS) module contained in GID^{SR4}, responsible for bridging the substrate receptor to the other E3 ligase subunits; (2) the catalytic (Cat) module, also present in GID^{SR4}, which binds and activates the Ubc8~Ub intermediate; and (3) a previously undescribed supramolecular assembly (SA) module.

A 3.4-Å map of the Chelator-GID^{SR4} SRS module fit the prior coordinates for this region (PDB: 6SWY) (Figures 3A and S4B). As described previously, the globular substrate-binding domain of Gid4 fits snugly in a complementary concave surface of the scaffold subunit Gid5. This arrangement is supported by a base from Gid1^{SRS} and Gid8^{SRS}, which form an intricate heterodimer involving their LisH-CTLH-CRA domains.

Focused refinement over the Cat module yielded a 3.8-Å-resolution reconstruction (Figures 3A and S4C). The map quality permitted *de novo* building and refinement of atomic coordinates for the majority of Gid2 and Gid9 (Figure S3A). The catalytic function is mediated by a region of Gid2 that adopts an E3 ligase RING domain fold (albeit stabilized by a single zinc in the E2∼Ub binding site) together with a portion of Gid9 that adopts a unique RING-like (RING-L) structure (Figure S3B; Braun et al., 2011; Qiao et al., 2020; Regelmann et al., 2003). Folding of the Gid2 RING depends on its incorporation into the intricately configured Gid2-Gid9 heterodimer. The Gid2 RING is embedded in an unprecedented intermolecular heart-shaped domain, stabilized by Gid9 elements, including an intermolecular zinc-binding domain; a belt that encases roughly three quarters of the base of Gid2's RING; the RING-L domain, which packs against the remaining side of Gid2's RING; and the extreme C terminus, which contributes to Gid2's RING in a manner analogous to canonical RING dimers (Budhidarmo et al., 2012). Gid2 and Gid9 are further intertwined by their N termini co-assembling in an ∼70-Å-long 4-helix coiled coil (Figures 3A and S3A).

Within Chelator-GID^{SR4}, the two Gid2-Gid9 E3 ligase domains face the two degron-binding Gid4 subunits. A model of the Gid2 RING-Ubc8∼Ub intermediate based on published isolated RING E3-E2∼Ub complexes shows the Gid2 RING domain recruiting Ubc8, whereas its linked Ub would be activated by Gid2 and Gid9 in the canonically activated conformation (Figures 3A and S3B; Dou et al., 2012; Plechanovová et al., 2012; Pruneda et al., 2012). The model explains the previously reported effects of Gid2 and Gid9 point mutations on Fbp1 degradation (Qiao et al., 2020).

A 3.6-Å resolution map of the SA module within Chelator-GID^{SR4} enabled building of an atomic model (Figures 3A and S4D). The two Gid7 protomers form an asymmetric dimer on one side of the module. Gid1^{SA} and Gid8^{SA} form an interdigitated scaffold that connects the Gid7 dimer to the Cat module.

Each Gid7 protomer consists of an N-terminal LisH-CTLH-CRA motif and an atypical β-propeller. The LisH-CTLH-CRA motifs form elongated helical double-sided dimerization domains (Figure S3C). The LisH and CTLH helices initially progress in one direction. The distal end is capped by the first two CRA helices. The remaining CRA helices reverse and traverse the length of the domain, pack against CTLH helices along the way, and terminate adjacent to the LisH helices. We refer to one side of the LisH-CTLH-CRA structure as "LisH-CRA^{C}" because it contains the LisH and C-terminal CRA helices. Accordingly, the other side is called "CTLH-CRA^{N}." The Gid7 LisH-CRA^{C} motifs mediate homodimerization, much like LisH-CRA^{C} motifs mediate heterodimerization between Gid1^{SRS} and Gid8^{SRS} and between Gid2 and Gid9 (Qiao et al., 2020).

β-Propellers are protein interaction domains formed by toroidally arranged β sheet "blades" (Chen et al., 2011a). The 7-bladed propellers from the two Gid7 protomers ensue from the LisH-CTLH-CRA motifs at different relative angles and interact with each other. The resultant asymmetric double-propeller domain binds part of Gid1^{SA}. The SA module is further stabilized by distinctive interactions between the CTLH-CRA^{N} domains from Gid1^{SA}, a loop from Gid8^{SA}, and the CTLH-CRA^{N} domain from a Gid7 protomer we call Gid7$^{to\text{-}Cat}$ because it points toward the Cat module (Figure S3D). The remainder of the Gid1^{SA} and Gid8^{SA} subcomplex superimposes on corresponding regions of Gid1^{SRS} and Gid8^{SRS}. At the two edges of the SA module, the CTLH-CRA^{N} domains from the SRS-facing Gid7 protomer (Gid7$^{to\text{-}SRS}$) and Gid8^{SA} connect to the SRS and Cat modules, respectively.

Supramolecular chelate assembly is supported by inter- and intramodule LisH-CTLH-CRA domain interactions

The relative arrangement of E3 ligase elements—the Gid4 substrate receptor and the Gid2-Gid9 RING-RING-L complex—in Chelator-GID^{SR4} depends on the exterior oval band. The oval is established by two types of intersubunit interactions—within the modules and mediating intermodule connections—in a daisy chain-like arrangement of LisH-CTLH-CRA domains (Figures 3B and 3C).

In Chelator-GID^{SR4}, the modules are connected to each other by outward-facing heterotypic dimerization of CTLH-CRA^{N} domains at the edges of each module (Figure 3B). The CTLH-CRA^{N} domains connect modules in a side-by-side manner. In the GID^{SR4} assembly, the SRS and Cat modules are adjoined by interactions between the CTLH-CRA^{N} domains of Gid8^{SRS} and Gid9. The Cat and SA modules are bridged by interactions between the CTLH-CRA^{N} domains of Gid2 and Gid8^{SA}. Notably, Gid2's CTLH-CRA^{N} domain also packs against Gid9's RING-L domain, which may explain how formation of the Chelator-GID^{SR4} assembly affects intrinsic Ub transferase activity (Figures 3A, S1A, and S3B). The oval structure also depends on adjoining the SRS and SA modules through interactions between the CTLH-CRA^{N} domains of Gid1^{SRS} and Gid7$^{to\text{-}SRS}$. Despite the similarity of intermodule interactions at a secondary structural level, specificity is dictated by contacts between domains, ensuring formation of the Chelator-GID^{SR4} assembly.

Chelator-GID^{SR4} assembly mediates avid recruitment of the tetrameric substrate Fbp1

Comparing the major classes of Chelator-GID^{SR4} alone or bound to Fbp1 showed relative repositioning of the SRS module toward the center of the oval to bind the substrate, resembling a Venus flytrap capturing its prey (Figure 4A). An individual Fbp1 Pro/N-degron was visualized bound to Gid4 in a locally refined map of SRS (Figures 4B and S4B). Fbp1's N-terminal proline and two subsequent residues are recruited much like short peptides binding human Gid4 (Chen et al., 2017; Dong et al., 2018; Hämmerle et al., 1998). Comparing the substrate-bound Chelator-GID^{SR4} structure with the substrate-free GID^{SR4} (Qiao et al., 2020) shows remodeling of several Gid4 loops to embrace the N-terminal residues PTL of the Fbp1 substrate (Figure 4B).

Notably, the Pro/N-degrons and several subsequent residues are not visible in the Fbp1 crystal structure, suggesting that they are intrinsically disordered (Figure 4C). These elements could emanate from opposite sides of the disk-like Fbp1 catalytic domain. In the complex with Chelator-GID^{SR4}, degrons from both sides appear to simultaneously ensnare Gid4 substrate receptors. Such avid binding would rationalize the 10-fold lower K_m in Fbp1 ubiquitylation assays (Figure 1C). To further test

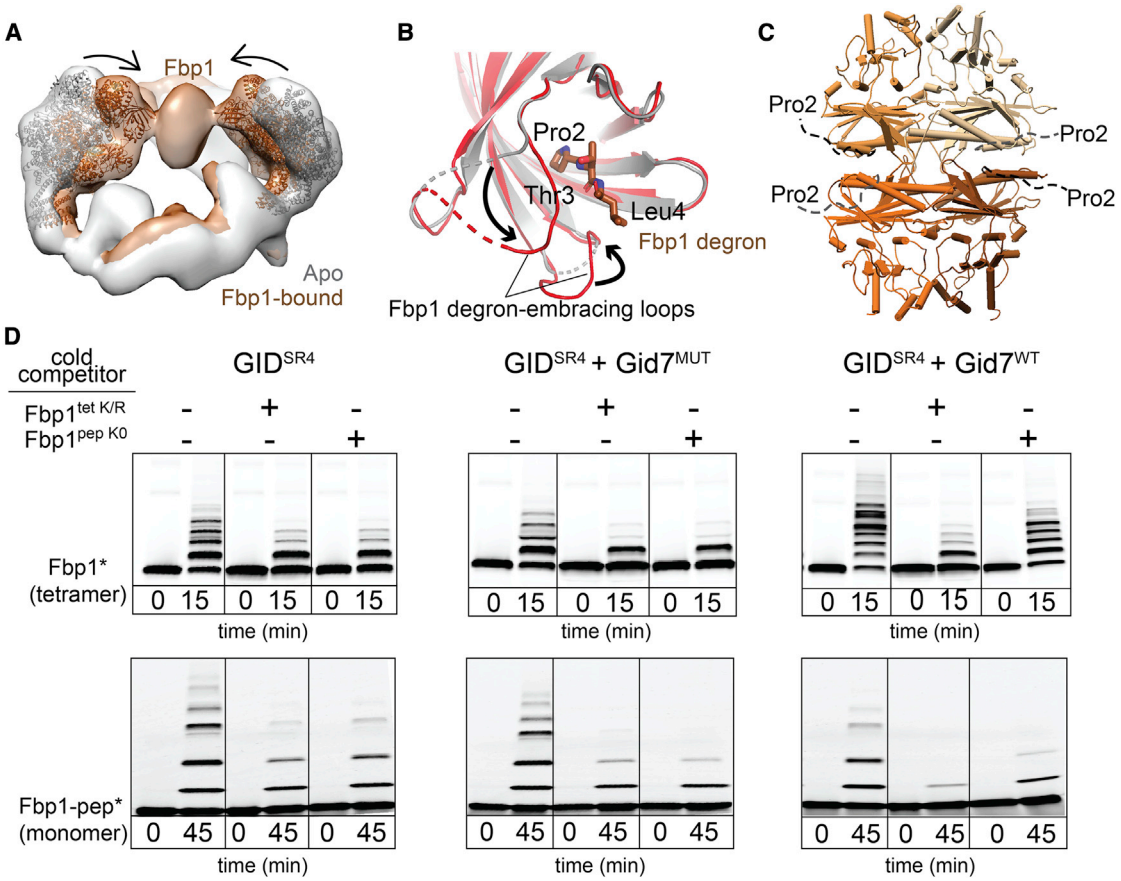

Figure 4. Chelator-GID^{SR4} assembly specifies multivalent binding for the tetrameric Fbp1 substrate

(A) Superimposed maps of substrate-free (gray) and Fbp1-bound Chelator-GID^{SR4} (brown) show relative inward movement of SRS modules (ribbon) upon substrate recruitment.

(B) Conformational differences between Gid4 in GID^{SR4} (PDB: 6SWY, gray) and Fbp1-bound Chelator-GID^{SR4} (red). The first three residues of Fbp1 (the Pro/N-degron) bound to Gid4 are shown as sticks.

(C) Crystal structure of the Fbp1 tetramer, with the N-terminal region (residues 2–19), including the degron not visible in the electron density, depicted as dotted lines. Fbp1 protomers are shown in various brown shades.

(D) Competitive *in vitro* ubiquitylation assays probing multivalent E3-substrate interactions. Chelator-GID^{SR4} has two substrate binding sites and two catalytic centers, whereas two other E3 assemblies (GID^{SR4} or GID^{SR4} + Gid7^{MUT} lacking the LisH-CTLH-CRA motif, Δ1–285) have only one substate binding site and one catalytic center. Substrates are oligomeric (tetrameric Fbp1) or monomeric (a peptide harboring a single acceptor Lys, Fbp1-pep) and fluorescently labeled at the C terminus (denoted by an asterisk). Competitors are oligomeric (tetrameric Fbp1$^{tet\ K/R}$, with preferred target lysines mutated to arginines) or monomeric (lysine-less peptide, Fbp1$^{pep\ K0}$).

See also Figure S4 and Tables S1 and S2.

the possibility of avid substrate capture, we performed competitive qualitative ubiquitylation assays. Unlabeled monomeric and tetrameric Fbp1 competitors had a comparable inhibitory effect on ubiquitylation of fluorescent Fbp1 by GID^{SR4} or GID^{SR4} mixed with a Gid7 mutant that does not support supramolecular assembly (Figure 4D). However, compared with an unlabeled monomeric inhibitor, the unlabeled Fbp1 tetramer was strikingly more effective at impeding Chelator-GID^{SR4} ubiquitylation of fluorescent Fbp1. The same inhibitory trends were observed for ubiquitylation of a fluorescent monomeric peptide substrate, confirming that the Fbp1 tetramer complements the Chelator assembly. The data are consistent with avid Fbp1 recruitment to Chelator-GID^{SR4} depending on supramolecular assembly of the E3 ligase and its substrate.

Chelator-GID^{SR4} assembly establishes dual site-specific Ub targeting

We next mapped regions of Fbp1 engaging the ubiquitylation active sites. Locating di-Gly sites by mass spectrometry identified Chelator-GID^{SR4}-mediated ubiquitylation of two pairs of neighboring lysines, K32/K35 and K280/K281, preferentially from 18 potential target lysines on the surface of Fbp1 (Figure S5). The importance of these lysines was confirmed mutationally (Figures 5A and 5B). Use of K0 Ub had shown modification of up to two sites in an Fbp1 protomer during the time course of the experiment (Figure 1B). Eliminating either lysine pair reduced this to monoubiquitylation, with a slightly greater effect on the K32/K35 mutant (Figure 5A). The results suggest that either region can be ubiquitylated independent of the other but that, for

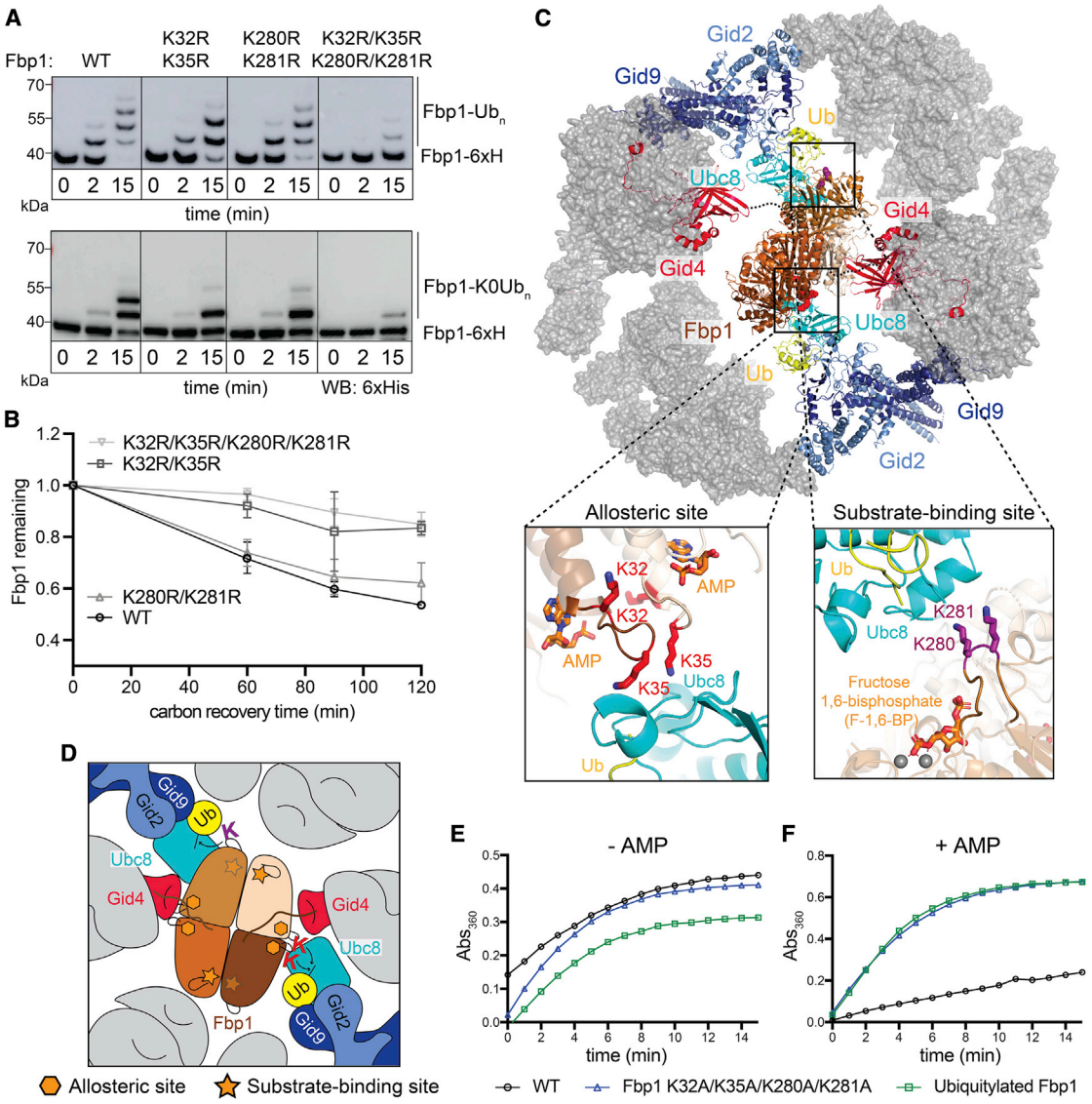

Figure 5. Chelator-GID^{SR4} configures simultaneous targeting of specific lysine clusters in metabolic regulatory regions of the Fbp1 tetramer

(A) *In vitro* ubiquitylation of Fbp1-6xHis, detected by anti-His immunoblotting, with WT (top) or K0 (bottom) Ub, testing the effects of mutating the major Fbp1 Ub-targeted lysines identified by mass spectrometry.

(B) Glucose-induced degradation *in vivo* of exogenously expressed WT or lysine mutant versions of Fbp1. Substrate levels were quantified as the ratio of substrate detected relative to the level after switching from carbon starvation to carbon recovery conditions. Points represent mean, and error bars represent SD (n = 3).

(C) Structural model of Chelator-GID^{SR4}-mediated ubiquitylation of Fbp1. Ubc8~Ub was modeled by aligning a RING-E2~Ub structure (PDB: 5H7S) on Gid2 RING. Dotted lines indicate disordered Fbp1 N termini. Close ups show major Fbp1 ubiquitylation sites near substrate (Fructose-1,6-bisphosphate, F-1,6-BP) and allosteric AMP binding sides modeled from structures with human Fbp1 (PDB: 5ZWK and 5ET6).

(D) Structure-based cartoon of Fbp1 ubiquitylation as shown in (C). Stars and hexagons represent substrate-binding and allosteric sites in Fbp1, respectively.

(E) *In vitro* Fbpase activity of purified WT, polyubiquitylated, and mutant Fbp1 (K32A/K35A/K280A/K281A).

(F) Fbpase activity assay as in (E), testing the responses of purified WT, polyubiquitylated, and mutant Fbp1 (K32A/K35A/K280A/K281A) to the allosteric inhibitor AMP.

See also Figure S5.

a given protomer, ubiquitylation is restricted to one lysine within a pair. Testing the effects of the mutations on Fbp1 degradation confirmed the importance of these lysines *in vivo*, with substantial stabilization even upon mutating only the K32/K35 lysine pair (Figure 5B).

To understand how the Chelator-GID^{SR4} supramolecular assembly determines regulation, we generated a structural model of ubiquitylation (Figures 5C and 5D). Fbp1 was first anchored via two degrons, one from each side binding a Gid4. Ubc8~Ub was modeled on the Gid2-Gid9 RING-RING-L domains based

on homology to another RING-E2∼Ub assembly (Nayak and Sivaraman, 2018). Fbp1 was subjected to constrained rotation to localize the K32 and K35 region of one protomer adjacent to one active site. This led to two striking observations. First, the K32 and K35 regions of two pairs of protomers are adjacent to each other. Second, and unexpectedly, when a K32 and K35 region is aligned with one active site, the K280 and K281 region of a different Fbp1 protomer is simultaneously situated in the other Chelator-GID^{SR4} active site. Thus, the Chelator-GID^{SR4} supramolecular assembly complements the tetrameric structure of Fbp1 by enabling simultaneous capture of two Pro/N degrons and simultaneous ubiquitylation of multiple protomers within the Fbp1 tetramer.

Given that Fbp1 is allosterically regulated in response to metabolite binding (Ke et al., 1990a, 1990b), we inspected the structure for potential functional importance of the ubiquitylation sites (Figures 5C and 5D). Intriguingly, the K32 and K35 residues reside in a loop abutting the allosteric site that regulates Fbp1 activity by binding the non-competitive inhibitor AMP (Ke et al., 1990b). K280 and K281 are located adjacent to another interprotomer interface, relatively near the substrate binding site (Ke et al., 1990a). We thus examined the effects of Chelator-GID^{SR4} ubiquitylation on Fbp1 activity. A K32A/K35A/K280A/K281A mutant and a ubiquitylated version of Fbp1 show Fbpase activity in our assay. However, allosteric modulation by AMP was substantially impaired in both cases (Figures 5E and 5F). Thus, Chelator-GID^{SR4} targets sites related to Fbp1's metabolic function.

Structural and mechanistic parallels in human CTLH E3

To determine whether structural principles governing activity of the yeast GID E3 are conserved in higher eukaryotes, we studied the human CTLH complex, whose subunits mirror those of Chelator-GID^{SR4} (Figure 6A).

We first reconstituted a recombinant complex that we call "CTLH^{SR4}," which parallels yeast GID^{SR4}. A low-resolution cryo-EM envelope showed that the corresponding human subunits form SRS (hGid4-ARMC8-RANBP9-TWA1) and Cat (RMND5A-MAEA) modules (Figure S6A). As for yeast GID^{SR4} (Qiao et al., 2020), the CTLH^{SR4} Cat module is relatively poorly resolved, but the coordinates for the yeast Gid2-Gid9 subcomplex derived from Chelator-GID^{SR4} readily fit in the density. A 3.2-Å-resolution map obtained by focused refinement enabled building of atomic coordinates for the human SRS module, which superimposes on its yeast counterpart (Figures 6B, S6B and S7; Table S1).

We tested whether the structural conservation extended to the enzymatic mechanism. Because the Pro/N-end degron targets of the CTLH E3 remain unknown, we generated a model peptide substrate: an N-terminal PGLW sequence reported previously to optimally bind hGid4 (Dong et al., 2018, 2020), connected via a flexible linker to a C-terminal target lysine. With this peptide substrate, we tested the effects of structure-based point mutations on ubiquitylation. The hGid4 residues mediating its incorporation into CTLH^{SR4} and RMND5A and MAEA residues that activate UBE2H∼Ub are crucial for peptide substrate ubiquitylation (Figures S6C–S6H). Moreover, as with GID^{SR4} (Qiao et al., 2020), only K48 of all Ub lysines was sufficient to support polyUb chain formation by CTLH^{SR4}, albeit to a substantially lesser degree than WT Ub (Figure S6I). Thus, it seems that the human CTLH core module parallels that in yeast GID assemblies.

We examined by cryo-EM whether the human Gid7 orthologs WDR26 and MKLN1 have capacity for supramolecular assembly. We obtained reconstructions for two subcomplexes containing WDR26. Coexpressing WDR26 with scaffolding and catalytic subunits (ARMC8-RANBP9-TWA1-RMND5A-MAEA) yielded a complex broadly resembling Chelator-GID^{SR4} in that it forms a hollow oval of similar dimensions (Figures 6A and 6C). Docking structures of human and yeast subcomplexes into the density showed that a WDR26 dimer is the SA module. However, WDR26 binds directly to RANBP9-TWA1 in the scaffold, without duplicates of these subunits corresponding to yeast Gid1^{SA}-Gid8^{SA}. The distinct WDR26-dependent supramolecular assembly places four—not two—ARMC8 subunits poised to each bind a hGid4 to capture substrate degrons in the CTLH oval.

The distinctive arrangement of SA and SRS modules was preserved in a 6-Å resolution map of WDR26, RANBP9, TWA1, ARMC8, hGid4, and the poorly understood CTLH subunit YPEL5 (Figure 6C; Table S1). Interestingly, YPEL5 binds at the junction of the two protomers in the WDR26 double-propeller domain.

A low-resolution map showed yet another SA for another human Gid7 ortholog, MKLN1, bound to the CTLH SRS module (Figure 6D; Table S1). Like WDR26, MKLN1 binds directly to RANBP9-TWA1 in the scaffold without intervening duplicates of these subunits. However, in accordance with previous studies (Delto et al., 2015; Kim et al., 2014), MKLN1 forms a tetramer. Four MKLN1 protomers bind between two CTLH SRS modules, demonstrating potential for even higher-order CTLH complex assemblies.

We confirmed roles of WDR26 and MKLN1 in human CTLH complex assembly by sedimentation analyses of lysates from K562 cells or lines in which the human Gid7 orthologs were deleted. Immunoblotting of fractions from sucrose density gradients of parental K562 cell lysates showed comigration of CTLH subunits, corresponding to a complex with a molecular weight greater than that predicted for a uniformly stoichiometric assembly (600–800 kDa according to standards) (Figure 6E). However, probing migration of the core subunit RANBP9 as a marker for the CTLH complex showed that the assembly changes markedly, toward fractions of 150–350 kDa, in CRISPR-Cas9 genome-edited lines lacking WDR26, MKLN1, or both or the Cat module subunit MAEA (Figures 6F and S6J). Interestingly, migration of WDR26 and MKLN1 in higher-molecular-weight fractions is not interdependent (Figure 6G), possibly indicating that each Gid7 ortholog can reside in distinct CTLH assemblies. Much of the total CTLH population shifted to lower-molecular-weight fractions upon deletion of WDR26, with a lesser effect of deleting MKLN1. This may suggest that a greater proportion of the CTLH complex in these cells depends on WDR26 for supramolecular assembly, perhaps because of a higher relative concentration of WDR26 or factors differentially regulating WDR26 or MKLN1 assembly into CTLH complexes.

Overall, the results suggest that CTLH E3 assemblies contain SRS, Cat, and SA modules with features resembling those of Chelator-GID^{SR4}. Moreover, differences in structural configuration of complexes containing MKLN1 or WDR26 offer prospects

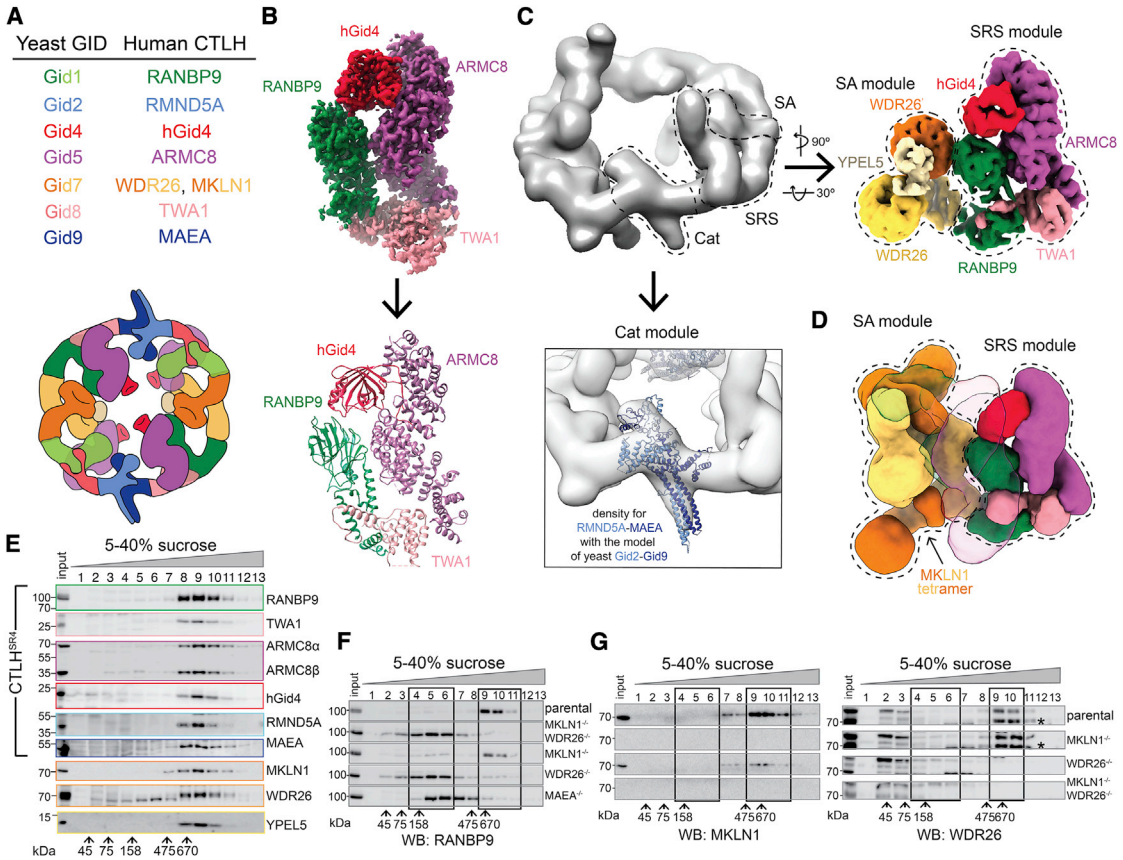

Figure 6. Higher-order assemblies of human CTLH E3

(A) Color-coded guide to yeast GID subunits and their human orthologs in the CTLH complex (top). Two colors indicate multiple protomers of a subunit. Cartoon colored as in the top, representing CTLH oval assembly where the SA module is the WDR26-YPEL5 dimer (bottom).

(B) 3.2-Å-resolution segmented map of CTLH SRS module (RANBP9-TWA1-ARMC8-hGid4) obtained by focused refinement of $CTLH^{SR4}$ (top) and its corresponding model (bottom).

(C) Cryo-EM maps of CTLH assemblies containing the Cat (RMND5A-MAEA), SRS (RANBP9-TWA1-ARMC8 alone or bound to hGid4), and/or supramolecular assembly (WDR26 with or without YPEL5) modules, as indicated. Subunits are colored according to the guide in (A). Top left: low-resolution map of WDR26-mediated SA of CTLH (RANBP9-TWA1-ARMC8-MAEA-RMND5A-WDR26). Right: 6.5-Å-resolution map of the human CTLH SRS module (RANBP9-TWA1-ARMC8-hGid4) subcomplex with an SA module comprising WDR26-YPEL5. Bottom panel: the yeast Gid2-Gid9 structure in the corresponding CTLH Cat module.

(D) 10.4-Å-resolution map of the human CTLH SRS module with MKLN1 as the SA module. The second copy of the SRS module in the subcomplex is transparent.

(E) Immunoblots of fractions from sucrose gradients of K562 cell lysates, probed with the indicated antibodies.

(F) Immunoblots probing for the core CTLH subunit (RANBP9) in fractions from sucrose gradients of lysates from parental K562 and *WDR26*$^{-/-}$/*MKLN1*$^{-/-}$, *MKLN1*$^{-/-}$, *WDR26*$^{-/-}$, and *MAEA*$^{-/-}$ knockout cells. Black boxes delineate high- and low-molecular weight (MW) peak fractions.

(G) As in (F) but probed as indicated with anti-MKLN1 or -WDR26 antibodies. *, WDR26 band.

See also Figures S6 and S7 and Table S1.

that CTLH may adopt a variety of supramolecular E3 assemblies that could impart distinct functionalities.

DISCUSSION

Here we discovered multipronged substrate targeting by an E3 ligase chelate supramolecular assembly tailored to the oligomeric quaternary structure of its metabolic enzyme substrate. In the absence of chelate assembly, GID^{SR4} is a competent E3 ligase that can bind a substrate degron, activate the intrinsic reactivity of its E2 partner (the Ubc8∼Ub intermediate), and promote Ub transfer from Ubc8 to a recruited substrate (Qiao et al., 2020). GID^{SR4} is also competent *in vivo* insofar as Gid7 is not required for glucose- and GID-dependent degradation of several substrates (Figure 1). Instead of binding directly to its specified substrate Fbp1, Gid7 alters the GID assembly (Figures 2 and 3).

Although other E3s have been reported to self-assemble (Balaji and Hoppe, 2020), this is typically achieved by catalytic or substrate receptor subunits; for example, the dimeric RING domains of single-subunit E3s or dimeric F-box and BTB substrate receptors in multisubunit cullin-RING ligases (Dou et al., 2012; McMahon et al., 2006; Ogura et al., 2010; Plechanovová et al., 2012; Welcker et al., 2013; Zhuang et al., 2009). Substrate-bound multivalent E3s can undergo liquid-liquid phase-separation (Bouchard et al., 2018). However, the transformation into

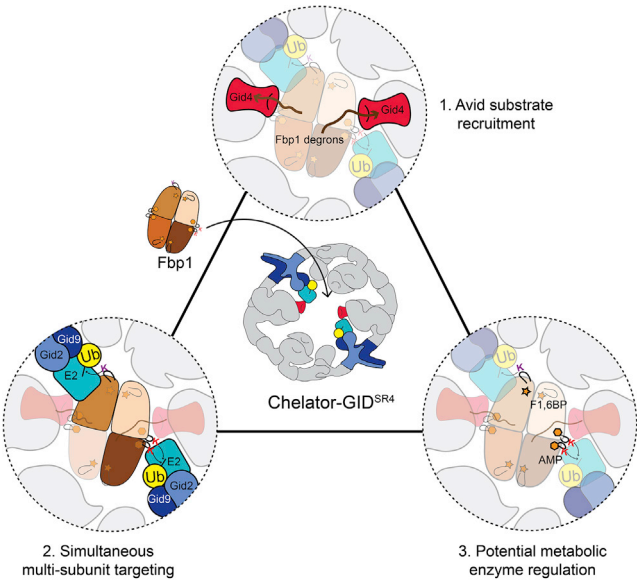

Figure 7. Molecular logic of multipronged Ub targeting of Fbp1 by Chelator-GID^{SR4}

Supramolecular chelate assembly specifies oligomeric metabolic enzyme targeting. (1) Opposing Gid4 subunits avidly bind multiple degrons of tetrameric Fbp1. (2) Opposing RING-E2~Ub active sites simultaneously target specific lysine clusters. (3) Targeted lysines map to metabolically important regions of oligomeric substrate.

Chelator-GID^{SR4} is a distinctive, extreme, and specific adjustment of E3 ligase architecture (Figures 2 and 3).

Resembling an organometallic chelate interacting with its central ligand, Chelator-GID^{SR4}'s multiple distinct points of contact with Fbp1 not only include the degron-binding sites from two opposing Gid4 substrate receptors but also the ubiquitylation active sites from Ubc8~Ub intermediates activated by two opposing Gid2-Gid9 catalytic domains (Figures 4, 5, and 7). Relative to the monodentate GID^{SR4}, the Chelator-GID^{SR4} assembly enables more molecules within the Fbp1 tetramer to be ubiquitylated simultaneously, increasing Ub density on a given Fbp1 tetramer (Figures 1A and 1B). Interestingly, there is not a 1:1 correspondence between the number of degron binding sites in Chelator-GID^{SR4} and the number of degrons in Fbp1. The Fbp1 tetramer has four exposed potential degrons, two on each side, both seemingly poised to capture one central-facing Gid4 in Chelator-GID^{SR4} (Figure 4C). An excess number of degrons is reminiscent of substrates recruited to the cullin-RING ligase receptor Cdc4, whose single binding site can continually and dynamically sample multiple degrons (Mittag et al., 2008). For Chelator-GID^{SR4}-bound Fbp1, we speculate that the arrangement of degrons allows their rapid interchange. This could potentially mediate switching between the protomers positioned adjacent to the active sites.

The human CTLH E3 complex displays striking parallels to Chelator-GID^{SR4}, albeit with interesting twists. In particular, the different Gid7 orthologs form distinct supramolecular assemblies (Figure 6). We speculate that the unique assemblies define distinct functions, as implied by varying phenotypic alterations upon their individual mutation (Bauer et al., 2018; Nassan et al., 2017; Skraban et al., 2017; Zhen et al., 2020) .

Taken together with previous data (Lampert et al., 2018; Qiao et al., 2020), it is now clear that there is not a single yeast GID or human CTLH complex. Rather, GID and CTLH are examples of responsive systems of multiprotein assemblies with an active E3 core that can be elaborated by supramolecular assembly. Although the function of one such assembly is shown here, the variations revealed by human Gid7 orthologs suggest that they, and presumably other subunits, also co-configure substrate binding and ubiquitylation active sites in accordance with the molecular organization and quaternary structure of particular substrates. The Chelator model presented here demonstrates how GID (and presumably CTLH) utilizes an elegant molecular logic: the response to a signal such as glucose availability converges on numerous aspects of its substrate's structure and function to achieve precise physiological regulation (Figure 7).

Limitations

Chelator-GID^{SR4} is remarkably specific in ubiquitylating particular Fbp1 lysines in metabolic regulatory regions. However, the physiological roles of Fbp1 ubiquitylation impairing allosteric regulation and metabolic function are unknown. Future studies will be required to determine how metabolic flux is coupled with GID-dependent ubiquitylation during termination of gluconeogenesis.

Although Chelator-GID^{SR4} is active toward Mdh2 and Pck1, it is unclear why these oligomeric substrates are less dependent than Fbp1 on Gid7-mediated supramolecular assembly. One speculative possibility could be that any potential advantage of avid binding is offset by accessibility of numerous ubiquitylation sites to GID^{SR4}. Future studies will be required to understand how Pck1 and other GID E3 substrates, including the Gid4 substrate receptor itself, are recognized and ubiquitylated (Hämmerle et al., 1998; Karayel et al., 2020; Menssen et al., 2018).

Finally, although discovery of the Chelator configuration provides a basis for understanding higher-order GID assembly, what other assemblies or sub-assemblies may form and their functions remain unknown. Clearly, other arrangements are observed for human CTLH complexes with WDR26. MKLN1 forms an even higher-order assembly with the human SRS module. Some yeast GID assemblies migrate in the void volume, as seen by size-exclusion chromatography (Figure S2A). Moreover, the mechanistic roles of additional subunits, including YPEL5 (Figure 6), or regulatory partners, such as Cdc48/p97, remain unknown (Barbin et al., 2010; Lampert et al., 2018). We await future studies revealing functions of other variations of GID and CTLH assemblies.

STAR★METHODS

Detailed methods are provided in the online version of this paper and include the following:

- KEY RESOURCES TABLE
- RESOURCE AVAILABILITY

SUPPLEMENTAL INFORMATION

Supplemental information can be found online at https://doi.org/10.1016/j.molcel.2021.03.025.

ACKNOWLEDGMENTS

We thank A. Varshavsky for promoter reference plasmids; S. Übel and S. Pettera for peptide synthesis; D. Bollschweiler, T. Schäfer, J. Basquin, K. Valer-Saldana, and S. Pleyer for assistance with cryo-EM and crystallography; Swiss Light Source, Villigen, Switzerland for Fbp1 crystal data collection; M. Strauss for assistance with initial negative-stain data collection on the yeast Chelator-GID complex; M. Yamaguchi for Gid7 constructs; G. Kleiger for guidance regarding kinetics; I. Paron for technical assistance with mass spectrometry; and K. Baek, B. Bräuning, and the Schulman lab for advice and support. The B.A.S. lab is funded by the Leibniz Prize from Deutsche Forschungsgemeinschaft (SCHU 3196/1-1). B.A.S. and M.M. are supported by the Max Planck Society.

AUTHOR CONTRIBUTIONS

Initial conceptualization, D.S., J.C., and B.A.S.; methodology, D.S., J.C., J.R.P., C.R.L., O.K., A.F.A., and B.A.S.; investigation, D.S., J.C., S.Q., C.R.L., L.A.H., K.V.G., F.M.H., O.K., J.R.P., and A.F.A.; resources, D.S., J.C., K.V.G., C.R.L., S.v.G., and A.F.A.; writing – original draft, D.S., J.C., and B.A.S.; writing – review & editing, D.S., J.C., C.R.L., A.F.A., and B.A.S.; supervision, M.M., A.F.A., and B.A.S.; funding acquisition, M.M. and B.A.S.

DECLARATION OF INTERESTS

B.A.S. is an honorary professor at Technical University of Munich, Germany and adjunct faculty at St. Jude Children's Research Hospital, Memphis, TN, USA and is on the scientific advisory board of Interline Therapeutics.

Received: October 15, 2020
Revised: February 17, 2021
Accepted: March 17, 2021
Published: April 26, 2021

REFERENCES

Adams, P.D., Afonine, P.V., Bunkóczi, G., Chen, V.B., Davis, I.W., Echols, N., Headd, J.J., Hung, L.W., Kapral, G.J., Grosse-Kunstleve, R.W., et al. (2010). PHENIX: a comprehensive Python-based system for macromolecular structure solution. Acta Crystallogr. D Biol. Crystallogr. *66*, 213–221.

Afonine, P.V., Klaholz, B.P., Moriarty, N.W., Poon, B.K., Sobolev, O.V., Terwilliger, T.C., Adams, P.D., and Urzhumtsev, A. (2018). New tools for the analysis and validation of cryo-EM maps and atomic models. Acta Crystallogr. D Struct. Biol. *74*, 814–840.

Baek, K., Krist, D.T., Prabu, J.R., Hill, S., Klügel, M., Neumaier, L.M., von Gronau, S., Kleiger, G., and Schulman, B.A. (2020). NEDD8 nucleates a multivalent cullin-RING-UBE2D ubiquitin ligation assembly. Nature *578*, 461–466.

Balaji, V., and Hoppe, T. (2020). Regulation of E3 ubiquitin ligases by homotypic and heterotypic assembly. F1000Res. *9*, F1000 Faculty Rev-88.

Barbin, L., Eisele, F., Santt, O., and Wolf, D.H. (2010). The Cdc48-Ufd1-Npl4 complex is central in ubiquitin-proteasome triggered catabolite degradation of fructose-1,6-bisphosphatase. Biochem. Biophys. Res. Commun. *394*, 335–341.

Barford, D. (2020). Structural interconversions of the anaphase-promoting complex/cyclosome (APC/C) regulate cell cycle transitions. Curr. Opin. Struct. Biol. *61*, 86–97.

Bauer, A., Jagannathan, V., Högler, S., Richter, B., McEwan, N.A., Thomas, A., Cadieu, E., André, C., Hytönen, M.K., Lohi, H., et al. (2018). MKLN1 splicing defect in dogs with lethal acrodermatitis. PLoS Genet. *14*, e1007264.

Biyani, N., Righetto, R.D., McLeod, R., Caujolle-Bert, D., Castano-Diez, D., Goldie, K.N., and Stahlberg, H. (2017). Focus: The interface between data collection and data processing in cryo-EM. J. Struct. Biol. *198*, 124–133.

Boldt, K., van Reeuwijk, J., Lu, Q., Koutroumpas, K., Nguyen, T.M., Texier, Y., van Beersum, S.E., Horn, N., Willer, J.R., Mans, D.A., et al.; UK10K Rare Diseases Group (2016). An organelle-specific protein landscape identifies novel diseases and molecular mechanisms. Nat. Commun. *7*, 11491.

Bouchard, J.J., Otero, J.H., Scott, D.C., Szulc, E., Martin, E.W., Sabri, N., Granata, D., Marzahn, M.R., Lindorff-Larsen, K., Salvatella, X., et al. (2018). Cancer Mutations of the Tumor Suppressor SPOP Disrupt the Formation of Active, Phase-Separated Compartments. Mol. Cell *72*, 19–36.e8.

Braun, B., Pfirrmann, T., Menssen, R., Hofmann, K., Scheel, H., and Wolf, D.H. (2011). Gid9, a second RING finger protein contributes to the ubiquitin ligase activity of the Gid complex required for catabolite degradation. FEBS Lett. *585*, 3856–3861.

Brown, N.G., VanderLinden, R., Watson, E.R., Weissmann, F., Ordureau, A., Wu, K.P., Zhang, W., Yu, S., Mercredi, P.Y., Harrison, J.S., et al. (2016). Dual RING E3 Architectures Regulate Multiubiquitination and Ubiquitin Chain Elongation by APC/C. Cell *165*, 1440–1453.

Budhidarmo, R., Nakatani, Y., and Day, C.L. (2012). RINGs hold the key to ubiquitin transfer. Trends Biochem. Sci. *37*, 58–65.

Burnley, T., Palmer, C.M., and Winn, M. (2017). Recent developments in the CCP-EM software suite. Acta Crystallogr. D Struct. Biol. *73*, 469–477.

Cao, W.X., Kabelitz, S., Gupta, M., Yeung, E., Lin, S., Rammelt, C., Ihling, C., Pekovic, F., Low, T.C.H., Siddiqui, N.U., et al. (2020). Precise Temporal Regulation of Post-transcriptional Repressors Is Required for an Orderly Drosophila Maternal-to-Zygotic Transition. Cell Rep. *31*, 107783.

Chen, V.B., Arendall, W.B., 3rd, Headd, J.J., Keedy, D.A., Immormino, R.M., Kapral, G.J., Murray, L.W., Richardson, J.S., and Richardson, D.C. (2010). MolProbity: all-atom structure validation for macromolecular crystallography. Acta Crystallogr. D Biol. Crystallogr. *66*, 12–21.

Chen, C.K., Chan, N.L., and Wang, A.H. (2011a). The many blades of the β-propeller proteins: conserved but versatile. Trends Biochem. Sci. *36*, 553–561.

Chen, I., Dorr, B.M., and Liu, D.R. (2011b). A general strategy for the evolution of bond-forming enzymes using yeast display. Proc. Natl. Acad. Sci. USA *108*, 11399–11404.

Chen, S., Wu, J., Lu, Y., Ma, Y.B., Lee, B.H., Yu, Z., Ouyang, Q., Finley, D.J., Kirschner, M.W., and Mao, Y. (2016). Structural basis for dynamic regulation of the human 26S proteasome. Proc. Natl. Acad. Sci. USA *113*, 12991–12996.

Chen, S.J., Wu, X., Wadas, B., Oh, J.H., and Varshavsky, A. (2017). An N-end rule pathway that recognizes proline and destroys gluconeogenic enzymes. Science *355*, eaal3655.

Chiang, H.L., and Schekman, R. (1991). Regulated import and degradation of a cytosolic protein in the yeast vacuole. Nature *350*, 313–318.

Cong, L., Ran, F.A., Cox, D., Lin, S., Barretto, R., Habib, N., Hsu, P.D., Wu, X., Jiang, W., Marraffini, L.A., and Zhang, F. (2013). Multiplex genome engineering using CRISPR/Cas systems. Science *339*, 819–823.

Cowtan, K. (2006). The Buccaneer software for automated model building. 1. Tracing protein chains. Acta Crystallogr. D Biol. Crystallogr. *62*, 1002–1011.

Delto, C.F., Heisler, F.F., Kuper, J., Sander, B., Kneussel, M., and Schindelin, H. (2015). The LisH motif of muskelin is crucial for oligomerization and governs intracellular localization. Structure *23*, 364–373.

DiMaio, F., Echols, N., Headd, J.J., Terwilliger, T.C., Adams, P.D., and Baker, D. (2013). Improved low-resolution crystallographic refinement with Phenix and Rosetta. Nat. Methods *10*, 1102–1104.

Dong, C., Zhang, H., Li, L., Tempel, W., Loppnau, P., and Min, J. (2018). Molecular basis of GID4-mediated recognition of degrons for the Pro/N-end rule pathway. Nat. Chem. Biol. *14*, 466–473.

Dong, C., Chen, S.J., Melnykov, A., Weirich, S., Sun, K., Jeltsch, A., Varshavsky, A., and Min, J. (2020). Recognition of nonproline N-terminal residues by the Pro/N-degron pathway. Proc. Natl. Acad. Sci. USA *117*, 14158–14167.

Dou, H., Buetow, L., Sibbet, G.J., Cameron, K., and Huang, D.T. (2012). BIRC7-E2 ubiquitin conjugate structure reveals the mechanism of ubiquitin transfer by a RING dimer. Nat. Struct. Mol. Biol. *19*, 876–883.

Emsley, P., and Cowtan, K. (2004). Coot: model-building tools for molecular graphics. Acta Crystallogr. D Biol. Crystallogr. *60*, 2126–2132.

Emsley, P., Lohkamp, B., Scott, W.G., and Cowtan, K. (2010). Features and development of Coot. Acta Crystallogr. D Biol. Crystallogr. *66*, 486–501.

Fernandez-Leiro, R., and Scheres, S.H.W. (2017). A pipeline approach to single-particle processing in RELION. Acta Crystallogr. D Struct. Biol. *73*, 496–502.

Francis, O., Han, F., and Adams, J.C. (2013). Molecular phylogeny of a RING E3 ubiquitin ligase, conserved in eukaryotic cells and dominated by homologous components, the muskelin/RanBPM/CTLH complex. PLoS ONE *8*, e75217.

Gancedo, C. (1971). Inactivation of fructose-1,6-diphosphatase by glucose in yeast. J. Bacteriol. *107*, 401–405.

Gibson, D.G., Young, L., Chuang, R.Y., Venter, J.C., Hutchison, C.A., 3rd, and Smith, H.O. (2009). Enzymatic assembly of DNA molecules up to several hundred kilobases. Nat. Methods *6*, 343–345.

Goddard, T.D., Huang, C.C., Meng, E.C., Pettersen, E.F., Couch, G.S., Morris, J.H., and Ferrin, T.E. (2018). UCSF ChimeraX: Meeting modern challenges in visualization and analysis. Protein Sci. *27*, 14–25.

Hämmerle, M., Bauer, J., Rose, M., Szallies, A., Thumm, M., Düsterhus, S., Mecke, D., Entian, K.D., and Wolf, D.H. (1998). Proteins of newly isolated mutants and the amino-terminal proline are essential for ubiquitin-proteasome-catalyzed catabolite degradation of fructose-1,6-bisphosphatase of Saccharomyces cerevisiae. J. Biol. Chem. *273*, 25000–25005.

Haselbach, D., Schrader, J., Lambrecht, F., Henneberg, F., Chari, A., and Stark, H. (2017). Long-range allosteric regulation of the human 26S proteasome by 20S proteasome-targeting cancer drugs. Nat. Commun. *8*, 15578.

Janke, C., Magiera, M.M., Rathfelder, N., Taxis, C., Reber, S., Maekawa, H., Moreno-Borchart, A., Doenges, G., Schwob, E., Schiebel, E., and Knop, M. (2004). A versatile toolbox for PCR-based tagging of yeast genes: new fluorescent proteins, more markers and promoter substitution cassettes. Yeast *Aug;21(11)*.

Kaiser, S.E., Riley, B.E., Shaler, T.A., Trevino, R.S., Becker, C.H., Schulman, H., and Kopito, R.R. (2011). Protein standard absolute quantification (PSAQ) method for the measurement of cellular ubiquitin pools. Nat. Methods *8*, 691–696.

Karayel, O., Michaelis, A.C., Mann, M., Schulman, B.A., and Langlois, C.R. (2020). DIA-based systems biology approach unveils E3 ubiquitin ligase-dependent responses to a metabolic shift. Proc. Natl. Acad. Sci. USA *117*, 32806–32815.

Ke, H.M., Thorpe, C.M., Seaton, Ba., Lipscomb, W.N., and Marcus, F. (1990a). Structure refinement of fructose-1,6-bisphosphatase and its fructose 2,6-bisphosphate complex at 2.8 A resolution. J. Mol. Biol. *212*, 513–539.

Ke, H.M., Zhang, Y.P., and Lipscomb, W.N. (1990b). Crystal structure of fructose-1,6-bisphosphatase complexed with fructose 6-phosphate, AMP, and magnesium. Proc. Natl. Acad. Sci. USA *87*, 5243–5247.

Kelley, L.A., Mezulis, S., Yates, C.M., Wass, M.N., and Sternberg, M.J. (2015). The Phyre2 web portal for protein modeling, prediction and analysis. Nat. Protoc. *10*, 845–858.

Kim, K.H., Hong, S.K., Hwang, K.Y., and Kim, E.E. (2014). Structure of mouse muskelin discoidin domain and biochemical characterization of its self-association. Acta Crystallogr. D Biol. Crystallogr. *70*, 2863–2874.

Knop, M., Siegers, K., Pereira, G., Zachariae, W., Winsor, B., Nasmyth, K., and Schiebel, E. (1999). Epitope tagging of yeast genes using a PCR-based strategy: more tags and improved practical routines. Yeast *Jul;15(10B)*.

Kobayashi, N., Yang, J., Ueda, A., Suzuki, T., Tomaru, K., Takeno, M., Okuda, K., and Ishigatsubo, Y. (2007). RanBPM, Muskelin, p48EMLP, p44CTLH, and the armadillo-repeat proteins ARMC8alpha and ARMC8beta are components of the CTLH complex. Gene *396*, 236–247.

Koshland, D.E., Jr. (1963a). Correlation of Structure and Function in Enzyme Action. Science *142*, 1533–1541.

Koshland, D.E., Jr. (1963b). Properties of the active site of enzymes. Ann. N Y Acad. Sci. *103*, 630–642.

Kulak, N.A., Pichler, G., Paron, I., Nagaraj, N., and Mann, M. (2014). Minimal, encapsulated proteomic-sample processing applied to copy-number estimation in eukaryotic cells. Nat. Methods *11*, 319–324.

Lampert, F., Stafa, D., Goga, A., Soste, M.V., Gilberto, S., Olieric, N., Picotti, P., Stoffel, M., and Peter, M. (2018). The multi-subunit GID/CTLH E3 ubiquitin ligase promotes cell proliferation and targets the transcription factor Hbp1 for degradation. eLife *7*, e35528.

Lander, G.C., Estrin, E., Matyskiela, M.E., Bashore, C., Nogales, E., and Martin, A. (2012). Complete subunit architecture of the proteasome regulatory particle. Nature *482*, 186–191.

Leggett, D.S., Hanna, J., Borodovsky, A., Crosas, B., Schmidt, M., Baker, R.T., Walz, T., Ploegh, H., and Finley, D. (2002). Multiple associated proteins regulate proteasome structure and function. Mol. Cell *10*, 495–507.

Liu, H., and Pfirrmann, T. (2019). The Gid-complex: an emerging player in the ubiquitin ligase league. Biol. Chem. *400*, 1429–1441.

Liu, H., Ding, J., Köhnlein, K., Urban, N., Ori, A., Villavicencio-Lorini, P., Walentek, P., Klotz, L.O., Hollemann, T., and Pfirrmann, T. (2020). The GID ubiquitin ligase complex is a regulator of AMPK activity and organismal lifespan. Autophagy *16*, 1618–1634.

Maitland, M.E.R., Onea, G., Chiasson, C.A., Wang, X., Ma, J., Moor, S.E., Barber, K.R., Lajoie, G.A., Shaw, G.S., and Schild-Poulter, C. (2019). The mammalian CTLH complex is an E3 ubiquitin ligase that targets its subunit muskelin for degradation. Sci. Rep. *9*, 9864.

Mastronarde, D. (2003). SerialEM: A Program for Automated Tilt Series Acquisition on Tecnai Microscopes Using Prediction of Specimen Position. Microsc. Microanal. *9*, 1182–1183.

McMahon, M., Thomas, N., Itoh, K., Yamamoto, M., and Hayes, J.D. (2006). Dimerization of substrate adaptors can facilitate cullin-mediated ubiquitylation of proteins by a "tethering" mechanism: a two-site interaction model for the Nrf2-Keap1 complex. J. Biol. Chem. *281*, 24756–24768.

Melnykov, A., Chen, S.J., and Varshavsky, A. (2019). Gid10 as an alternative N-recognin of the Pro/N-degron pathway. Proc. Natl. Acad. Sci. USA *116*, 15914–15923.

Menssen, R., Schweiggert, J., Schreiner, J., Kusevic, D., Reuther, J., Braun, B., and Wolf, D.H. (2012). Exploring the topology of the Gid complex, the E3 ubiquitin ligase involved in catabolite-induced degradation of gluconeogenic enzymes. J. Biol. Chem. *287*, 25602–25614.

Menssen, R., Bui, K., and Wolf, D.H. (2018). Regulation of the Gid ubiquitin ligase recognition subunit Gid4. FEBS Lett. *592*, 3286–3294.

Mittag, T., Orlicky, S., Choy, W.Y., Tang, X., Lin, H., Sicheri, F., Kay, L.E., Tyers, M., and Forman-Kay, J.D. (2008). Dynamic equilibrium engagement of a polyvalent ligand with a single-site receptor. Proc. Natl. Acad. Sci. USA *105*, 17772–17777.

Monod, J., Changeux, J.P., and Jacob, F. (1963). Allosteric proteins and cellular control systems. J. Mol. Biol. *6*, 306–329.

Nakatsukasa, K., Okumura, F., and Kamura, T. (2015). Proteolytic regulation of metabolic enzymes by E3 ubiquitin ligase complexes: lessons from yeast. Crit. Rev. Biochem. Mol. Biol. *50*, 489–502.

Nassan, M., Li, Q., Croarkin, P.E., Chen, W., Colby, C.L., Veldic, M., McElroy, S.L., Jenkins, G.D., Ryu, E., Cunningham, J.M., et al. (2017). A genome wide association study suggests the association of muskelin with early onset bipolar disorder: Implications for a GABAergic epileptogenic neurogenesis model. J. Affect. Disord. *208*, 120–129.

Nayak, D., and Sivaraman, J. (2018). Structure of LNX1:Ubc13∼Ubiquitin Complex Reveals the Role of Additional Motifs for the E3 Ligase Activity of LNX1. J. Mol. Biol. *430*, 1173–1188.

Ogura, T., Tong, K.I., Mio, K., Maruyama, Y., Kurokawa, H., Sato, C., and Yamamoto, M. (2010). Keap1 is a forked-stem dimer structure with two large spheres enclosing the intervening, double glycine repeat, and C-terminal domains. Proc. Natl. Acad. Sci. USA *107*, 2842–2847.

Oh, J.H., Chen, S.J., and Varshavsky, A. (2017). A reference-based protein degradation assay without global translation inhibitors. J. Biol. Chem. *292*, 21457–21465.

Pettersen, E.F., Goddard, T.D., Huang, C.C., Couch, G.S., Greenblatt, D.M., Meng, E.C., and Ferrin, T.E. (2004). UCSF Chimera–a visualization system for exploratory research and analysis. J. Comput. Chem. *25*, 1605–1612.

Plechanovová, A., Jaffray, E.G., Tatham, M.H., Naismith, J.H., and Hay, R.T. (2012). Structure of a RING E3 ligase and ubiquitin-loaded E2 primed for catalysis. Nature *489*, 115–120.

Pruneda, J.N., Littlefield, P.J., Soss, S.E., Nordquist, K.A., Chazin, W.J., Brzovic, P.S., and Klevit, R.E. (2012). Structure of an E3:E2∼Ub complex reveals an allosteric mechanism shared among RING/U-box ligases. Mol. Cell *47*, 933–942.

Qiao, S., Langlois, C.R., Chrustowicz, J., Sherpa, D., Karayel, O., Hansen, F.M., Beier, V., von Gronau, S., Bollschweiler, D., Schäfer, T., et al. (2020). Interconversion between Anticipatory and Active GID E3 Ubiquitin Ligase Conformations via Metabolically Driven Substrate Receptor Assembly. Mol. Cell *77*, 150–163.e9.

Regelmann, J., Schüle, T., Josupeit, F.S., Horak, J., Rose, M., Entian, K.D., Thumm, M., and Wolf, D.H. (2003). Catabolite degradation of fructose-1,6-bisphosphatase in the yeast Saccharomyces cerevisiae: a genome-wide screen identifies eight novel GID genes and indicates the existence of two degradation pathways. Mol. Biol. Cell *14*, 1652–1663.

Rusnac, D.V., and Zheng, N. (2020). Structural Biology of CRL Ubiquitin Ligases. Adv. Exp. Med. Biol. *1217*, 9–31.

Salemi, L.M., Maitland, M.E.R., McTavish, C.J., and Schild-Poulter, C. (2017). Cell signalling pathway regulation by RanBPM: molecular insights and disease implications. Open Biol. *7*, 170081.

Sanchez-Garcia, R., Gomez-Blanco, J., Cuervo, A., Carazo, J., Sorzano, C., and Vargas, J. (2020). DeepEMhancer: a deep learning solution for cryo-EM volume post-processing. bioRxiv. https://doi.org/10.1101/2020.06.12.148296.

Santt, O., Pfirrmann, T., Braun, B., Juretschke, J., Kimmig, P., Scheel, H., Hofmann, K., Thumm, M., and Wolf, D.H. (2008). The yeast GID complex, a novel ubiquitin ligase (E3) involved in the regulation of carbohydrate metabolism. Mol. Biol. Cell *19*, 3323–3333.

Scheres, S.H. (2012). RELION: implementation of a Bayesian approach to cryo-EM structure determination. J. Struct. Biol. *180*, 519–530.

Schindelin, J., Arganda-Carreras, I., Frise, E., Kaynig, V., Longair, M., Pietzsch, T., Preibisch, S., Rueden, C., Saalfeld, S., Schmid, B., et al. (2012). Fiji: an open-source platform for biological-image analysis. Nat. Methods *9*, 676–682.

Schork, S.M., Bee, G., Thumm, M., and Wolf, D.H. (1994a). Catabolite inactivation of fructose-1,6-bisphosphatase in yeast is mediated by the proteasome. FEBS Lett. *349*, 270–274.

Schork, S.M., Bee, G., Thumm, M., and Wolf, D.H. (1994b). Site of catabolite inactivation. Nature *369*, 283–284.

Schork, S.M., Thumm, M., and Wolf, D.H. (1995). Catabolite inactivation of fructose-1,6-bisphosphatase of Saccharomyces cerevisiae. Degradation occurs via the ubiquitin pathway. J. Biol. Chem. *270*, 26446–26450.

Schweitzer, A., Aufderheide, A., Rudack, T., Beck, F., Pfeifer, G., Plitzko, J.M., Sakata, E., Schulten, K., Förster, F., and Baumeister, W. (2016). Structure of the human 26S proteasome at a resolution of 3.9 Å. Proc. Natl. Acad. Sci. USA *113*, 7816–7821.

Shakeel, S., Rajendra, E., Alcón, P., O'Reilly, F., Chorev, D.S., Maslen, S., Degliesposti, G., Russo, C.J., He, S., Hill, C.H., et al. (2019). Structure of the Fanconi anaemia monoubiquitin ligase complex. Nature *575*, 234–237.

Skraban, C.M., Wells, C.F., Markose, P., Cho, M.T., Nesbitt, A.I., Au, P.Y.B., Begtrup, A., Bernat, J.A., Bird, L.M., Cao, K., et al. (2017). WDR26 Haploinsufficiency Causes a Recognizable Syndrome of Intellectual Disability, Seizures, Abnormal Gait, and Distinctive Facial Features. Am. J. Hum. Genet. *101*, 139–148.

Storici, F., and Resnick, M.A. (2006). The delitto perfetto approach to in vivo site-directed mutagenesis and chromosome rearrangements with synthetic oligonucleotides in yeast. Methods Enzymology *409*.

Tu, B.P., and McKnight, S.L. (2006). Metabolic cycles as an underlying basis of biological oscillations. Nat. Rev. Mol. Cell Biol. *7*, 696–701.

Tyanova, S., Temu, T., Sinitcyn, P., Carlson, A., Hein, M.Y., Geiger, T., Mann, M., and Cox, J. (2016). The Perseus computational platform for comprehensive analysis of (prote)omics data. Nat. Methods *13*, 731–740.

Waterhouse, A., Bertoni, M., Bienert, S., Studer, G., Tauriello, G., Gumienny, R., Heer, F.T., de Beer, T.A.P., Rempfer, C., Bordoli, L., et al. (2018). SWISS-MODEL: homology modelling of protein structures and complexes. Nucleic Acids Res. *46* (W1), W296–W303.

Watson, E.R., Brown, N.G., Peters, J.M., Stark, H., and Schulman, B.A. (2019). Posing the APC/C E3 Ubiquitin Ligase to Orchestrate Cell Division. Trends Cell Biol. *29*, 117–134.

Wehmer, M., Rudack, T., Beck, F., Aufderheide, A., Pfeifer, G., Plitzko, J.M., Förster, F., Schulten, K., Baumeister, W., and Sakata, E. (2017). Structural insights into the functional cycle of the ATPase module of the 26S proteasome. Proc. Natl. Acad. Sci. USA *114*, 1305–1310.

Weissmann, F., Petzold, G., VanderLinden, R., Huis In 't Veld, P.J., Brown, N.G., Lampert, F., Westermann, S., Stark, H., Schulman, B.A., and Peters, J.M. (2016). biGBac enables rapid gene assembly for the expression of

large multisubunit protein complexes. Proc. Natl. Acad. Sci. USA *113*, E2564–E2569.

Welcker, M., Larimore, E.A., Swanger, J., Bengoechea-Alonso, M.T., Grim, J.E., Ericsson, J., Zheng, N., and Clurman, B.E. (2013). Fbw7 dimerization determines the specificity and robustness of substrate degradation. Genes Dev. *27*, 2531–2536.

Zaman, S., Lippman, S.I., Zhao, X., and Broach, J.R. (2008). How Saccharomyces responds to nutrients. Annu. Rev. Genet. *42*, 27–81.

Zavortink, M., Rutt, L.N., Dzitoyeva, S., Henriksen, J.C., Barrington, C., Bilodeau, D.Y., Wang, M., Chen, X.X.L., and Rissland, O.S. (2020). The E2 Marie Kondo and the CTLH E3 ligase clear deposited RNA binding proteins during the maternal-to-zygotic transition. eLife *9*, e53889.

Zhang, K. (2016). Gctf: Real-time CTF determination and correction. J. Struct. Biol. *193*, 1–12.

Zhen, R., Moo, C., Zhao, Z., Chen, M., Feng, H., Zheng, X., Zhang, L., Shi, J., and Chen, C. (2020). Wdr26 regulates nuclear condensation in developing erythroblasts. Blood *135*, 208–219.

Zheng, S.Q., Palovcak, E., Armache, J.P., Verba, K.A., Cheng, Y., and Agard, D.A. (2017). MotionCor2: anisotropic correction of beam-induced motion for improved cryo-electron microscopy. Nat. Methods *14*, 331–332.

Zhu, J., and Thompson, C.B. (2019). Metabolic regulation of cell growth and proliferation. Nat. Rev. Mol. Cell Biol. *20*, 436–450.

Zhuang, M., Calabrese, M.F., Liu, J., Waddell, M.B., Nourse, A., Hammel, M., Miller, D.J., Walden, H., Duda, D.M., Seyedin, S.N., et al. (2009). Structures of SPOP-substrate complexes: insights into molecular architectures of BTB-Cul3 ubiquitin ligases. Mol. Cell *36*, 39–50.

Zivanov, J., Nakane, T., Forsberg, B.O., Kimanius, D., Hagen, W.J., Lindahl, E., and Scheres, S.H. (2018). New tools for automated high-resolution cryo-EM structure determination in RELION-3. eLife *7*, e42166.

3.2. Multifaceted N-degron recognition and ubiquitylation by GID/CTLH E3 ligases

(Chrustowicz and Sherpa, et al. Journal of Molecular Biology. 2021)

Gid7-dependent transformation of the GID complex facilitates targeting of oligomeric substrates. On top of their oligomeric state, another feature diversifying E3 ligase substrates is a sequence of their degrons. Although it is well-known that GID swaps its substrate receptors to recognize different sets of substrates, it is unclear what is a range of degrons recognized by a single substrate receptor. This issue is especially intriguing in the case of N-recognins with deep substrate-binding tunnels, like Gid4 and yGid10, which accommodate several N-terminal residues. In Chrustowicz and Sherpa, et al. 2021 [110], we comprehensively analyzed the specificity of three homologous GID/CTLH substrate receptors by screening a randomized library of N-terminal peptides displayed on phages. The screen identified unique binding motifs similar for hGid4 and yGid4 but distinct for yGid10. The new sequences substantiate recognition of peptides initiated with both Pro and non-Pro hydrophobic residues with affinities superior to natural Pro/N-degrons and other sequences identified to date. The structural data revealed that binding of diverse sequences by GID substrate receptors is possible thanks to the intrinsic plasticity of their substrate-binding tunnels. Finally, the analysis of natural degrons revealed that ubiquitylation of GID substrates is determined by a combination of degron identity, folded substrate domain with a unique distribution of targeted lysines, and a matching assembly of the E3 ligase.

Apart from designing experiments and preparing the manuscript, my contributions to this project involved: preparation of proteins for phage display screening and NMR, cloning Fbp1 constructs for *in vivo* degradation studies, performing *in vitro* binding (Fig. 1C, 4D, S1B and S1D) and activity (Fig. 4EF, 5AC, 6AB, S4A, S5C, S5D) assays, crystallization and determination of crystal structures of hGid4 and yGid10 bound to Phe/N-peptides (PDB ID: 7Q50 and 7Q51, respectively).

Multifaceted N-degron recognition and ubiquitylation by GID/CTLH E3 ligases

Author:
Jakub Chrustowicz,Dawafuti Sherpa,Joan Teyra,Mun Siong Loke,Grzegorz Popowicz,Jerome Basquin,Michael Sattler,J. Rajan Prabu,Sachdev S. Sidhu,Brenda A. Schulman

Publication: Journal of Molecular Biology

Publisher: Elsevier

Date: Available online 9 November 2021

Research Article

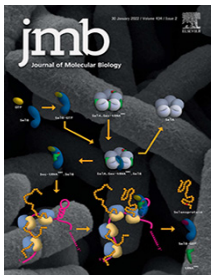

Multifaceted N-Degron Recognition and Ubiquitylation by GID/CTLH E3 Ligases

Jakub Chrustowicz [1†], Dawafuti Sherpa [1†], Joan Teyra [2], Mun Siong Loke [1], Grzegorz M. Popowicz [4,5], Jerome Basquin [6], Michael Sattler [4,5], J. Rajan Prabu [1], Sachdev S. Sidhu [2,3] and Brenda A. Schulman [1*]

*1 - **Department of Molecular Machines and Signaling,** Max Planck Institute of Biochemistry, 82152 Martinsried, Germany*
*2 - **The Donnelly Centre,** University of Toronto, Toronto, ON M5S 3E1, Canada*
*3 - **Department of Molecular Genetics,** University of Toronto, Toronto, ON M5S 1A8, Canada*
*4 - **Helmholtz Zentrum München,** Ingolstädter Landstrasse 1, 85764 Neuherberg, Germany*
*5 - **Bavarian NMR Center,** Department of Chemistry, Technical University of Munich, Germany*
*6 - **Department of Structural Cell Biology,** Max Planck Institute of Biochemistry, 82152 Martinsried, Germany*

***Correspondence to Brenda A. Schulman:** schulman@biochem.mpg.de (B.A. Schulman)*
@dawafutisherpa (D. Sherpa), @chrustowicz_j (J. Chrustowicz), @rajanprabu (J.R. Prabu)
https://doi.org/10.1016/j.jmb.2021.167347
Edited by Igor Stagljar

Abstract

N-degron E3 ubiquitin ligases recognize specific residues at the N-termini of substrates. Although molecular details of N-degron recognition are known for several E3 ligases, the range of N-terminal motifs that can bind a given E3 substrate binding domain remains unclear. Here, we discovered capacity of Gid4 and Gid10 substrate receptor subunits of yeast "GID"/human "CTLH" multiprotein E3 ligases to tightly bind a wide range of N-terminal residues whose recognition is determined in part by the downstream sequence context. Screening of phage displaying peptide libraries with exposed N-termini identified novel consensus motifs with non-Pro N-terminal residues binding Gid4 or Gid10 with high affinity. Structural data reveal that conformations of flexible loops in Gid4 and Gid10 complement sequences and folds of interacting peptides. Together with analysis of endogenous substrate degrons, the data show that degron identity, substrate domains harboring targeted lysines, and varying E3 ligase higher-order assemblies combinatorially determine efficiency of ubiquitylation and degradation.

Introduction

Specificity of ubiquitylation depends on E3 ligases recognizing motifs, termed "degrons", in substrates to be modified. The first such motif to be identified was the N-terminal sequence - now called N-degron[1] - in substrates of the yeast E3 ligase Ubr1.[2,3] Subsequently, several E3 ligases in different families were discovered to recognize protein N-termini as degrons. Higher eukaryotes have one HECT-type and several RING-family E3s with "Ubr" domains homologous to those in yeast Ubr1 that either have been shown to or are presumed to recognize distinct N-terminal sequences.[4,5] Other N-degron-recognizing ubiquitin ligases were identified either through characterizing substrate sequences mediating E3-binding,[6,7] or through systematic genetic screens matching human protein N-terminal sequences with E3 ligases.[8] Some of the best-studied pathways recognize sequences with an N-terminal Arg,[9] Pro[6,10] or Gly[8,11] (termed

Arg/N-degron, Pro/N-degron or Gly/N-degron, respectively), or acetylated N-terminus.[12–15]

An N-degron-recognizing E3 of emerging importance is a suite of related multiprotein complexes termed "GID" in budding yeast (named due to mutations causing *g*lucose-*i*nduced degradation *d*eficiency of fructose-1,6-bisphosphatase, Fbp1)[7,16–20] or "CTLH" in higher eukaryotes (named due to preponderance of subunits containing CTLH motifs).[21] The yeast GID E3 mediates degradation of gluconeogenic enzymes Fbp1, Mdh2 and Icl1 during recovery from carbon starvation.[7] The GID E3 recognizes the N-terminal Pro in these substrates generated by cleavage of the initiator methionine.[6,7] In higher eukaryotes, corresponding CTLH complexes are involved in diverse biological processes including erythropoiesis, organ development, embryogenesis, and cell division.[22–32] However, the mechanistic roles of CTLH-mediated ubiquitylation in these pathways remain largely mysterious.

Recent genetic, biochemical and structural studies have revealed that the GID E3 is not a singular complex. Rather a core GID^{Ant} complex (comprising Gid1, Gid5, Gid8, Gid2, Gid9 subunits) essentially anticipates shifts in environmental conditions that stimulate expression of interchangeable and mutually exclusive substrate-binding receptors – Gid4 (termed "yGid4" for yeast Gid4 hereafter),[17,33,34] Gid10 (yGid10 hereafter)[34–36] and Gid11 (yGid11 hereafter).[37] Whereas yGid4 is expressed after glucose has been restored to carbon-starved yeast, yGid10 and yGid11 are upregulated upon other environmental perturbations including heat shock, osmotic stress as well as carbon, nitrogen and amino acid starvation. The resultant E3 complexes, GID^{SR4}, GID^{SR10}, and GID^{SR11} (where SR# refers to Gid substrate receptor), recognize distinct N-terminal sequences of their substrates.[6,7,34,35,37] In addition, another subunit, Gid7, can drive supramolecular assembly of two GID^{SR4} units into a complex named Chelator-GID^{SR4} to reflect its resemblance to an organometallic chelate capturing a smaller ligand through multiple contacts.[38] The cryo EM structure of a Chelator-GID^{SR4} complex with Fbp1 showed two opposing Gid4 molecules avidly binding N-degrons from different Fbp1 protomers. As such, Fbp1 is encapsulated within the center of the oval-shaped Chelator-GID^{SR4}. This assembly positions functionally-relevant target lysines from multiple Fbp1 protomers adjacent to two Chelator-GID^{SR4} catalytic centers.

The molecular details of GID/CTLH recognition of Pro/N-degrons were initially revealed from crystal structures of human Gid4 (referred to as hGid4 hereafter) bound to peptides with N-terminal prolines.[10] Although Pro/N-degron substrates of the CTLH E3 remain unknown, hGid4 is suitably well-behaved for biophysical and structural characterization, whereas yGid4 has limited solubility on its own.[10] Previously, the sequence PGLWKS was identified as binding hGid4 with highest affinity amongst all sequences tested, with a K_D in the low micromolar range.[10] The crystallized peptide-binding region of hGid4, which superimposes with the substrate-binding domains of yGid4 and yGid10 in GID^{SR4} and GID^{SR10}, adopts an 8-stranded β-barrel with a central tunnel that binds the N-terminus of a peptide, or of the intrinsically-disordered N-terminal degron sequence of a substrate.[10,34,36,38,39] Loops between β-strands at the edge of the barrel bind residues downstream of the peptide's N-terminus. Interestingly, although GID^{SR4} was originally thought to exclusively bind peptides with an N-terminal Pro, hGid4 can also bind peptides with non-Pro hydrophobic N-termini such as Ile or Leu, albeit with at best ≈8-fold lower affinity.[39] Furthermore, yGid11 is thought to use a distinct structure to recognize substrate Thr/N-degrons.[37] Collectively, these findings suggested that the landscape of GID/CTLH E3 substrates can extend beyond Pro/N-degron motifs.

Here, phage display screening identified peptides with various non-Pro N-termini that not only bind hGid4, yGid4 and yGid10, but do so with comparable or higher affinity than the previously identified Pro-initiating sequences including Pro/N-degrons of ubiquitylation substrates. Structural data reveal that loops in GID/CTLH substrate-binding domains adopt conformations complementary to partner peptide sequences downstream of the N-terminus. Thus, sequence context is a determinant of N-terminal recognition by GID/CTLH substrate-binding domains. In the context of natural substrates recognized by yGid4, not only the degron but also the associated domain harboring targeted lysine contribute to ubiquitylation by the core GID^{SR4} and its superassembly.

Results

hGid4 can bind peptides with a range of N-terminal sequences

We took advantage of the amenability of hGid4 to biophysical characterization to further characterize features of the PGLWKS sequence mediating interactions. To assess the importance of peptide length beyond the N-terminus, we examined chemical shift perturbations (CSPs) in 2D ^{1}H, ^{15}N-HSQC NMR spectra of [^{15}N]-labeled hGid4 mixed with the amino acid Pro, a Pro-Gly dipeptide, or the PGLWKS peptide (Figure 1(A)). Although prior studies emphasized the importance of an N-terminal Pro,[10,39] Pro alone only minimally influenced the spectrum. The Pro-Gly dipeptide elicited stronger CSPs, presumably due to the peptide bond directly interacting with hGid4, and suppressing repulsion by burying the negatively charged carboxylate of a single Pro in a hydrophobic environment (Figure S1(A)). The PGLWKS peptide showed the greatest CSPs and binding kinetics in the slow exchange regime at the NMR chemical shift

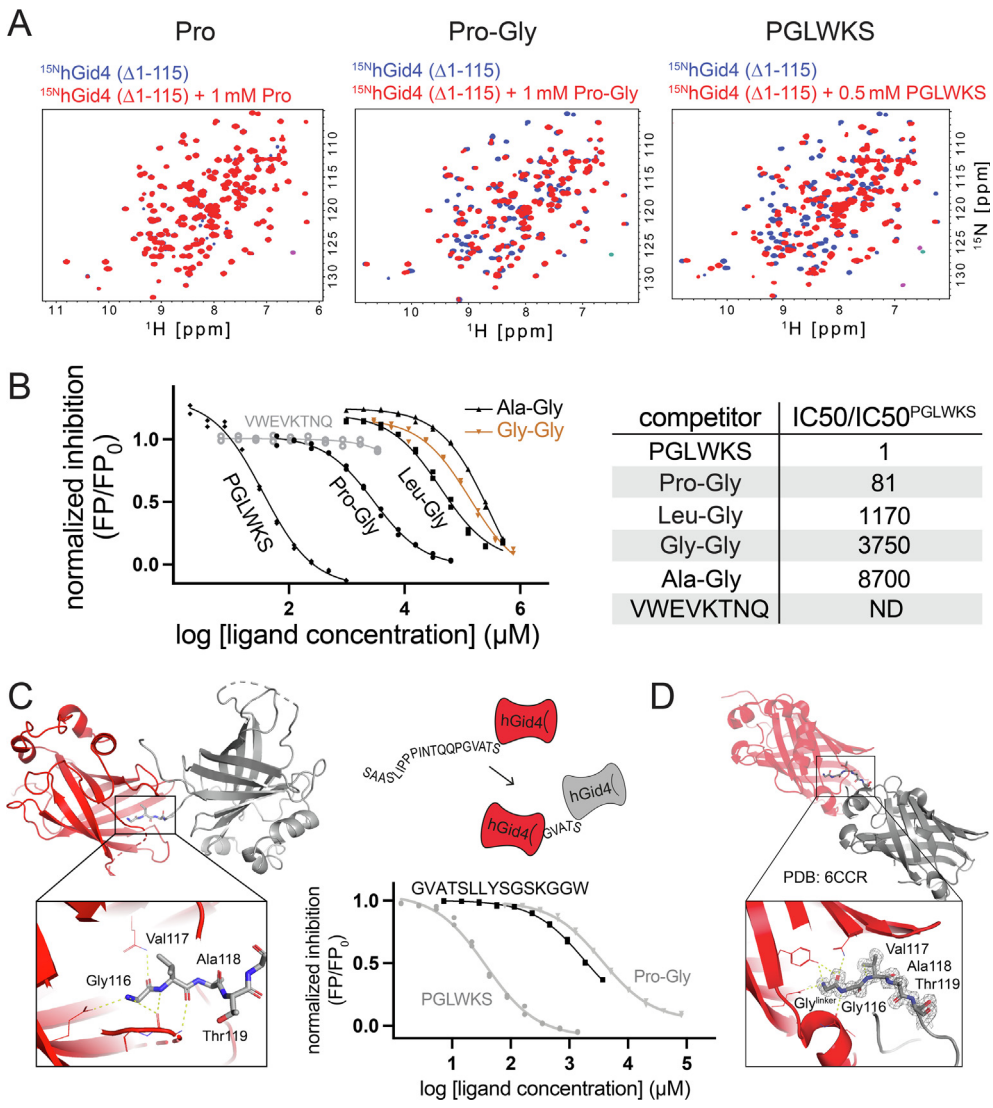

Figure 1. hGid4 recognizes various peptide N-termini and several downstream residues. A. Overlaid ^{1}H, ^{15}N-HSQC NMR spectra of 0.1 mM [^{15}N]-labeled 6xHis-hGid4 (Δ1-115) alone (blue) and upon addition of 1 mM Pro, 1 mM Pro-Gly or 0.5 mM PGLWKS peptide (red). B. Competitive fluorescence polarization (FP) experiments comparing different unlabeled ligands for inhibiting hGid4 (Δ1-115) binding to C-terminally fluorescein-labeled PGLWKS peptide. Ratios of FP signals at varying concentrations of unlabeled ligands to that in the absence of a competitor (FP/FP_0) were plotted as a function of log[ligand concentration] (left). Half-maximal inhibitory concentrations (IC50) for each ligand were determined by fitting to log[inhibitor] vs. response model and presented relative to IC50 of the unlabeled PGLWKS peptide (right). The peptide VWEVKTNQ corresponding to the N-terminus of Hbp1 (2–9) that is not an hGid4 substrate[88] was included as a negative control. C. Crystal structure of one hGid4 (red) accommodating serendipitously generated Gly116-initiating N-terminus of an adjacent hGid4 molecule (grey) in the crystal lattice. The binding strength of the newly generated N-terminal sequence (116–127) to hGid4 was compared to that of PGLWKS and Pro-Gly with competitive FP (right bottom). D. Previously published hGid4 crystal structure (PDB ID: **6CCR**) revealing one hGid4 binding the N-terminus bearing an additional Gly upstream Gly116 derived from cloning of an adjacent hGid4 molecule (grey) in the lattice of a distinct crystal form.

time scale, indicating tight binding, and, therefore, importance of downstream residues.

Given the ability of a Pro-Gly dipeptide to bind hGid4, we examined importance of the N-terminal residue by testing commercially-available variants (Leu-Gly, Ala-Gly, and Gly-Gly along with Pro-Gly) for competing with a fluorescently-labeled PGLWKS peptide whose binding to hGid4 can be measured by fluorescence polarization (FP) (Figure S1(B)). Although each of the dipeptides yielded sigmoidal curves, those with N-terminal Pro or Leu were superior (Figure 1(B)). Pro-Gly

showed a 15-fold lower IC_{50} than Leu-Gly, consistent with prior studies emphasizing the importance of an N-terminal Pro.[39]

To examine roles of individual positions in the 6-residue PGLWKS sequence, we employed peptide spot arrays testing all natural amino acids in position 1, positions 2 and 3 together, position 4 or position 5 (Figure S1(C)). Binding was detected after incubating the membranes with the substrate binding domain of hGid4, and immunoblotting with anti-hGid4 antibodies. Overall, the data confirm the previous findings that out of the peptides tested PGLWKS is an optimal binder, and that N-terminal non-Pro hydrophobic residues are tolerated in the context of the downstream GLWKS sequence albeit with lower binding.[10,39]

The peptide array data also highlighted the importance of context. Amongst the 400 possible combinations of residues 2 and 3, Gly, and to a lesser extent Ser, Val and Ala are preferred at position 2 and Ile or Leu at position 3, mirroring the previously defined sequence preferences.[10] The dynamic range of our assay suggested that downstream residues also contribute to specificity, by unveiling pronounced amino acid preference for bulky hydrophobics and some non-hydrophobic residues also at position 4. In agreement with the structural data,[10] the 5th position following the PGLW sequence tolerates many amino acids.

Despite this seemingly strong preference for an N-terminal Pro, we serendipitously visualized hGid4 recognizing a supposedly non-cognate sequence when we set out to visualize its structure in the absence of a peptide ligand by X-ray crystallography. Unexpectedly, the electron density from data at 3 Å resolution showed the first visible N-terminal residue of one molecule of hGid4 inserted into the substrate binding tunnel of an adjacent hGid4 molecule in the crystal lattice (Figure 1(C); Table S1). Perplexingly, this was not the first residue of the input hGid4 construct but Gly116 located 16 positions downstream. It appears that hGid4 underwent processing during crystallization, although it remains unknown if this neo-N-terminus was generated through enzymatic cleavage by a contaminating bacterial protease or chemical processing. Nonetheless, the potential for hGid4 to recognize a non-cognate N-terminal Gly was supported by re-examination of the published "apo" hGid4 crystal. In the previous structure of hGid4 (PDB ID: **6CCR)**, distinct crystal packing is also mediated by a peptide-like sequence (initiating with a Gly from the Tobacco Etch Virus (TEV) protease cleavage site, followed by hGid4 Gly116) inserting into the substrate binding tunnel of the neighboring molecule in the lattice (Figure 1(D)). The positions and interactions of the two N-terminal Gly are similar but not identical, as hGid4's Tyr258 does not hydrogen bond to the N-terminal amine of Gly116 in our structure.

To test binding of our fortuitously identified hGid4-binding sequence in solution, we examined competition with the fluorescently-labeled PGLWKS peptide (Figure 1(C)). Limited solubility of the GVATSLLYSGSKGGW peptide (hGid4 residues 116–127, with C-terminal Trp appended with a Gly-Gly linker to accurately measure peptide concentration) precluded accurate measurement of IC_{50} using our competitive FP assay. Nonetheless, the data qualitatively indicated that the GVATSLLYSGSKGGW peptide binds to hGid4 with significantly lower affinity than PGLWKS, but more tightly than the Pro-Gly dipeptide. Therefore, we speculate that these structurally-observed interactions were favored by the high concentration of protein during crystallization.

Taken together with published work, the data confirmed hGid4′s preference for binding to the previously-defined sequence PGLWKS, but they also highlighted capacity for hGid4 to recognize alternative N-termini. Moreover, given that specific combinations of residues downstream of the Pro-Gly substantially impact the interaction, we considered the possibility that hGid4 recognition of N-terminal sequences could be influenced by context.

Identification of superior hGid4-binding motifs not initiated by Pro

To discover alternative hGid4-binding sequences that do not initiate with Pro, we constructed a highly diverse N-terminal peptide phage-displayed library of 3.5×10^9 random octapeptides. The library was constructed after the signal peptide using 8 consecutive NNK degenerate codons encoding for all 20 natural amino acids and fused to the N-terminus of the phage coat protein. It is expected that Arg or Pro located next to the cleavage site (position + 1) will be inexistent or strongly underrepresented because they are known to either inhibit the secretion of phages[40,41] or the signal peptidase cleavage,[42,43] respectively.

The library was cycled through five rounds of selections following an established protocol[44] to enrich for phages displaying peptides that preferentially bound hGid4 (Figure 2(a)). Phages from individual clones that bound to GST-hGid4 (Δ1-99) but not a control GST based on phage ELISA were subjected to DNA sequence analysis.

The screen yielded 41 unique sequences, none of which were overtly similar to the previously defined hGid4-binding consensus motif PGLWKS (Figure 2(B); Table S2). A new consensus emerged with the following preferences: (1) hydrophobic residues at position 1, with Phe predominating; (2) Asp at position 2; (3) hydrophobic residues at positions 3 and 6, and to a lesser extent at position 5; and (4) small and polar residues at positions 4 and 7. Unlike the PGLWKS sequence wherein the striking selectivity

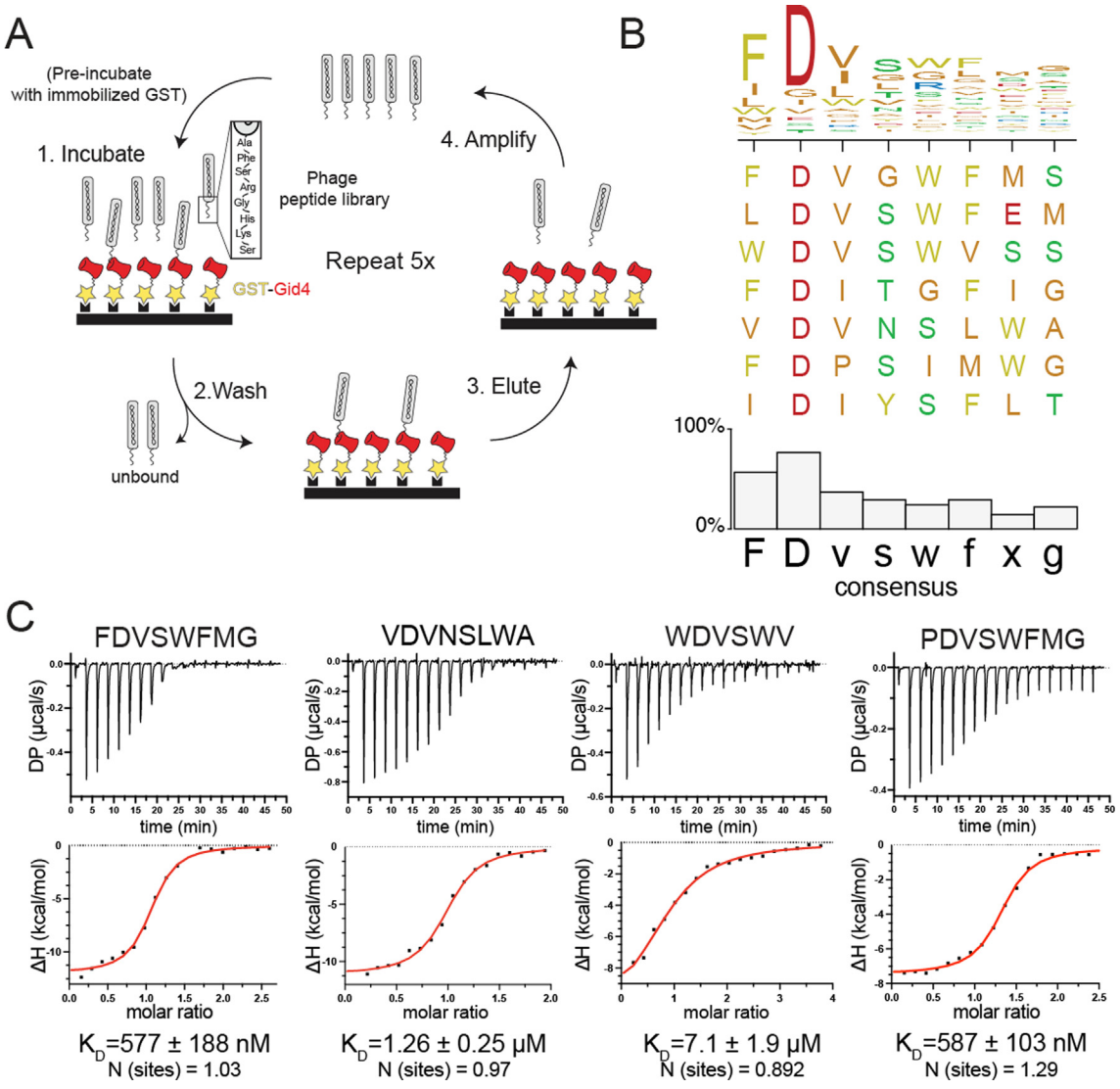

Figure 2. Identification of high-affinity hGid4-binding motifs initiating with non-Pro hydrophobic residues. A. Schematic of phage-display peptide library screen identifying peptides binding GST-tagged hGid4 (Δ1-99). B. Consensus motif obtained from multiple sequence alignment of 41 unique hGid4-binding peptide sequences listed in Table S2 (out of which a representative set of 7 sequences is shown). The height of the bars reflects the frequency of a given residue at different positions of the consensus. C. Isothermal titration calorimetry (ITC) to quantify binding of newly determined sequences to hGid4 (Δ1-115). The amount of heat released (ΔH) upon peptide injection was calculated from integrated raw ITC data (top) and plotted as a function of peptide:protein molar ratio (bottom). Dissociation constant (K_D) and the stoichiometry of the binding event (N) were determined by fitting to the One-Set-of-Sites binding model.

is predominantly for the first four residues, this new consensus extends through the seventh residue.

Although peptides with non-Pro hydrophobic N-termini were previously shown to bind hGid4, the tested sequences bound with one to two orders-of-magnitude lower affinity (K_D for IGLWKS 16 μM, VGLWKS 36 μM) than to PGLWKS (K_D = 1.9 μM) (Figure S2(A)).[39] To determine how the newly identified sequences compare, we quantified interactions by isothermal titration calorimetry (ITC). Notably, the peptides of sequences FDVSWFMG and VDVNSLWA showed superior binding (K_D = 0.6 and 1.3 μM, respectively) to the best binder with an N-terminal Pro (Figure 2(C) and S1(D)). Recognition of N-terminal Pro is also substantiated by the new consensus as substitution of Phe in FDVSWFMG with a Pro resulted in significantly tighter binding (K_D = 0.6 μM) than that of the PGLWKS motif (Figures 2(C) and S1(D)). Moreover, the affinity for a sequence starting with a Trp (K_D = 7.1 μM for WDVSWV) was superior to the previously identified best binder initiating with a non-Pro

hydrophobic residue (Figures 2(C) and S1(D)). Thus, hGid4 is able to accommodate even the bulkiest hydrophobic sidechain at the N-terminus of an interacting peptide. Taken together, the data show hGid4 binds a wide range of peptide sequences, with affinity strongly influenced by residues downstream of the N-terminus.

hGid4 structural pliability enables recognition of various N-terminal sequences

To understand how hGid4 recognizes diverse sequences, we determined its crystal structure bound to the FDVSWFMG peptide (Figure 3(A), Table S1; all peptide residues except C-terminal Gly visible in density). Overlaying this structure with published coordinates for other hGid4 complexes revealed diverse N-termini protruding into a common central substrate-binding tunnel (Figure S2(B), Phe (our study), or Pro, Leu, Val, or newly recognized Gly.[10,39] The N-terminal residues are anchored through contacts of their amine groups with hGid4 Glu237 and Tyr258 at the tip of the substrate binding tunnel, and common hydrogen bonds of the peptide backbone carbonyl to hGid4 Gln132.

The structures suggest that the varying peptide sequences are accommodated by complementary conformations of four hairpin loops (L1-L4) at the edge of the hGid4 substrate-binding tunnel (Figure 3(B)). The L2, L3, and L4 loops are fully or partially invisible, and are presumably mobile, in the structure of apo-hGid4 assembled in a subcomplex with its interacting subunits from the CTLH E3.[38] However, they are ordered and adopt different conformations when bound to the different peptides.

As compared to the structure with PGLWKS, the interactions with FDVSWFMG are more extensive and relatively more dominated by hydrophobic contacts rather than hydrogen bonding, which rationalizes improved binding of the new motif (Figure 3(C)). The L2 and L3 loops are relatively further from the central axis of the hGid4 β-barrel to interact with more residues in the peptide sequence. The different position of the L2 loop is also required to accommodate the hydrophobic Phe in the context of the new sequence (Figure 3(D)). Meanwhile, repositioning of the L4 loop places hGid4 Gln282 to form a hydrogen bond with Asp2 in the peptide (Figure 3(C)). Moreover, upon binding to hGid4, FDVSWFMG itself adopts a structured conformation owing to multiple intrapeptide backbone hydrogen bonds as well as interaction of Asp2 sidechain with the sidechain and backbone amide of Ser4 (Figure 3(E)). Therefore, a strong bias towards Asp at position 2 of all identified sequences may stem from its importance for maintaining the complementary folds of both the peptide and the substrate binding pocket. Overall, the structures reveal pliability of the hGid4 substrate-binding tunnel enabling interactions with a range of N-terminal sequences, which themselves may also contribute interactions by conformational complementarity.

Yeast GID substrate receptors recognize natural degrons with suboptimal affinity

To extend our findings to the yeast GID system, we screened the phage peptide library for binders to the yGid4 and yGid10 substrate receptors. The selected consensus sequence binding yGid4 paralleled that for hGid4 (Figure 4(A); Table S2), in agreement with their being true orthologs. Remarkably, despite high similarity to the Gid4s, and its only known endogenous substrate likewise initiating with a Pro,[36] the selections with yGid10 identified 12 unique sequences, some with bulky hydrophobic residues and others with Gly prevalent at position 1, each followed by a distinct downstream pattern (Figure 4(B); Table S3). By solving an X-ray structure of yGid10 bound to FWLPANLW peptide and superimposing it on its prior structure with N-terminus of its *bona fide* substrate Art2,[36] we confirmed that the novel sequence is accommodated by the previously characterized binding pocket of yGid10 (Figures 4(C) and S3(A); Table S1). Moreover, conformations of the yGid10 loops varied in complexes with different peptides,[36,45] suggesting like hGid4, yGid10 structural pliability allows recognition of various N-terminal sequences (Figure S3(B)).

Then, we sought to quantitatively compare binding of the new sequences to respective substrate receptors. Affinities of yGid10 for Phe and Gly-initiating sequences, measured by ITC, were comparable to and 2-fold greater than for a peptide corresponding to the N-degron of a natural substrate Art2[36] (Figures 4(D) and S3(C)). Notably, the endogenous degron, and selected sequences, bind yGid10 10- to 20-fold more tightly than the Pro-initiating sequence previously identified by a yeast two-hybrid screen.[35] Although yGid4 is not amenable to biophysical characterization, we could rank-order peptides by inhibition of ubiquitylation of a natural GID^{SR4} substrate Mdh2 (Figure 4(E)). Comparing IC_{50} values for the different peptides led to two major conclusions: (1) the phage display-selected sequences are better competitors than N-terminal sequences of endogenous gluconeogenic substrates, and (2) natural substrate N-terminal sequences themselves exhibit varying suppressive effects, with degron of Mdh2 being the most potent, followed by those of Fbp1 and Icl1.

To test if the novel sequences can mediate binding of substrates for ubiquitylation, we performed two experiments. First, we connected a yGid4- and a yGid10-binding sequence to a lysine via a flexible linker designed based on prior structural modelling.[38] The peptides also had a C-terminal fluorescein for detection. Incubating the peptides with either GID^{SR4} or GID^{SR10} and ubiquitylation assay mixes revealed that each serves as a substrate only for its cognate E3, with low activity

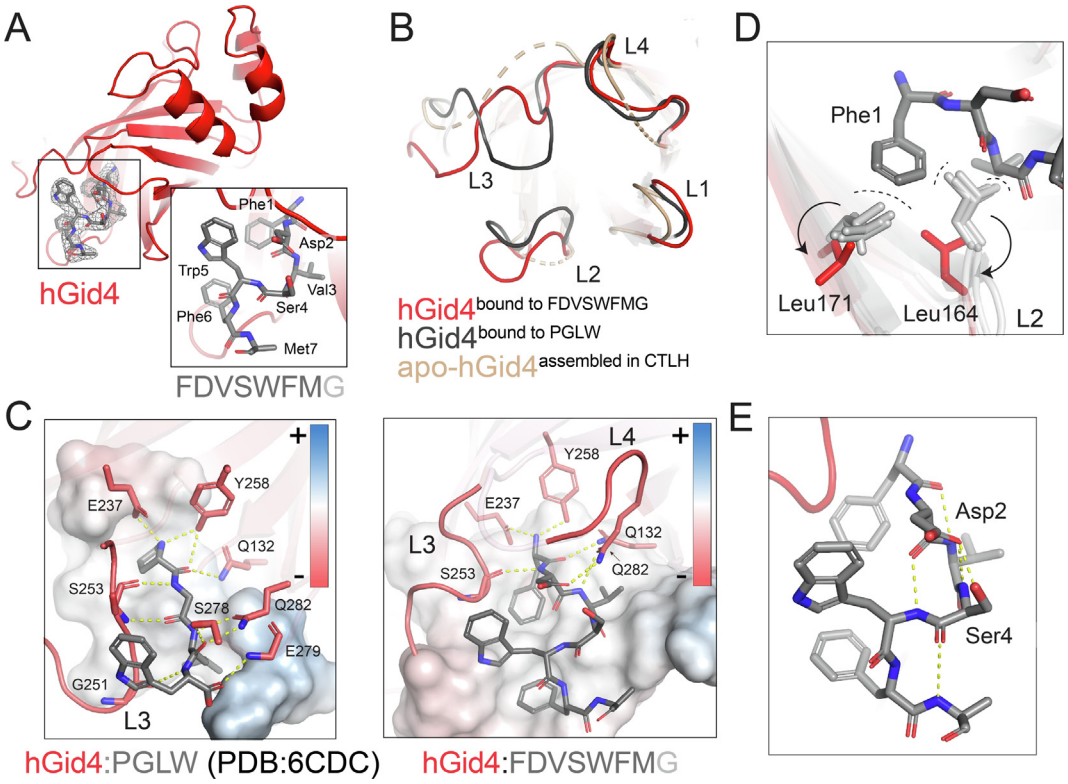

Figure 3. Molecular details of high-affinity peptide binding by hGid4. A. Crystal structure of hGid4 (Δ1-120, Δ294-300) bound to the FDVSWFMG peptide. Clear electron density ($2F_O$-F_C, contoured at 1.5 σ; grey mesh) was visible for all peptide residues besides the C-terminal Gly and the sidechain of Met7, presumably reflecting their mobility. B. Conformations of binding tunnel hairpin loops in apo-hGid4 assembled in CTLH^{SR4} (PDB ID: **7NSC**, light brown) as well as PGLW- (PDB ID: **6CDC**, dark grey) and FDVSWFMG-bound (red) hGid4. C. Comparison of PGLW (left) and FDVSWFMG (right) binding modes to hGid4. Hydrogen bonds between hGid4 residues (red sticks) and peptides (dark grey sticks) are depicted as yellow dashes, whereas the predominantly hydrophobic character of the binding tunnel is visualized as electrostatic potential surface (plotted at ± 7 kT/e; surface colored according to the potential: red – negative (-), blue – positive (+), white – uncharged). D. Overlay of hGid4 bound to PGLW (PDB ID: **6CDC**, light grey), IGLWKS (PDB ID: **6WZX**, light grey), VGLWKS (PDB ID: **6WZZ**, light grey) and FDVSWFMG (red) revealing conformational changes of L2 loop, which prevents steric clash (black dashes) between hGid4 Leu164 and Leu171 and N-terminal Phe of the FDVSWFMG peptide. E. Intrapeptide hydrogen bonding pattern (yellow dashes) within FDVSWFMG upon binding to hGid4.

of GID^{SR10} towards the yGid4-binding sequence (Figure 4(F)). Second, we replaced a native N-terminus of Fbp1 with the novel yGid4-binding consensus and performed *in vitro* ubiquitylation assay with two known forms of the GID E3 – the monomeric GID^{SR4} and the oligomeric Chelator-GID^{SR4} (Figure S4(A)). In both cases, the phage display-determined motif potentiated ubiquitylation of Fbp1 as compared to the WT control, indicating that it can mediate ubiquitylation of a full-length substrate.

Although ubiquitylation is typically a prerequisite, a multitude of processes control ubiquitin-mediated proteolysis in cells. Thus, we examined if the novel non-Pro initiating motifs would be sufficient to target Fbp1 for cellular degradation. We used the promoter reference technique, which was pioneered for examining degradation of GID E3 ligase substrates by normalizing for translation of an exogenously expressed substrate (here, C-terminally 3xFLAG-tagged versions of Fbp1) relative to a simultaneously expressed control (here, DHFR).[6,46] Since varying N-terminal sequences are differentially processed by Met-aminopeptidases,[47] or subjected to co-translational N-terminal acetylation[48] that would block binding to yGid4, we employed the previously-described technique of expressing assorted versions of Fbp1 as linear N-terminal fusions to ubiquitin. The N-terminal ubiquitin is cleaved off by deubiquitylating enzymes, revealing the residue following the ubiquitin sequence as a neo N-terminus.[39,49] As shown previously, Fbp1 harboring the native degron, or that replaced by the sequence IGLW that binds yGid4 with 8-fold lower affinity promoted timely degradation in this assay.[39] However, neither of the novel tight binders, initiating with either Phe or Leu, con-

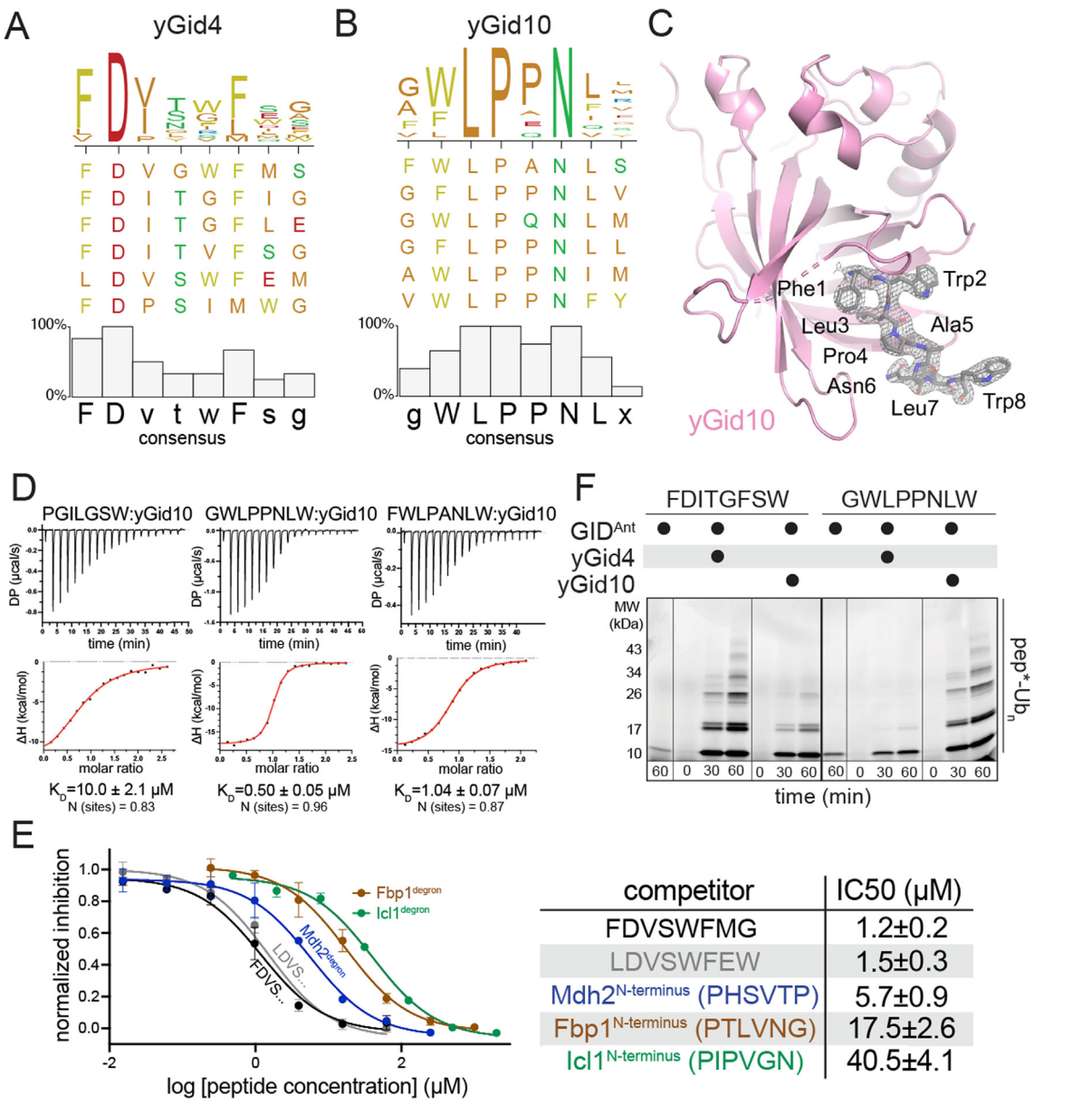

competitor	IC50 (µM)
FDVSWFMG	1.2±0.2
LDVSWFEW	1.5±0.3
Mdh2$^{N\text{-terminus}}$ (PHSVTP)	5.7±0.9
Fbp1$^{N\text{-terminus}}$ (PTLVNG)	17.5±2.6
Icl1$^{N\text{-terminus}}$ (PIPVGN)	40.5±4.1

Figure 4. Identification of novel yGid4 and yGid10-binding sequence motifs superior to natural degrons. A. Consensus motif obtained by multiple sequence alignment of 12 unique yGid4-binding peptide sequences listed in Table S2 (out of which a representative set of 6 sequences is shown). B. Consensus motif obtained by multiple sequence alignment of 12 unique yGid10-binding peptide sequences listed in Table S3 (out of which a representative set of 6 sequences is shown). C. Crystal structure of yGid10 (Δ1-64, Δ285-292) (pink) bound to FWLPANLW (grey sticks). The $2F_O$-F_C electron density map corresponding to the peptide is shown as grey mesh contoured at 2σ. D. ITC binding assays as in Figure 2(C) but quantifying binding of several peptides to yGid10 (Δ1-56). E. Competitive *in vitro* ubiquitylation assays probing binding of two novel Phe- and Leu-initiating sequences to yGid4 (Δ1-115) as compared to N-termini of natural GID substrates (Mdh2, Fbp1 and Icl1). Unlabeled peptides were titrated to compete off binding of fluorescent Mdh2 (labeled with C-terminal fluorescein) to GID^{SR4}, thus attenuating its ubiquitylation. Normalized inhibition (fraction of ubiquitylated Mdh2 at varying concentration of unlabeled peptides divided by that in the absence of an inhibitor) was plotted against peptide concentration. Fitting to log[inhibitor] vs. response model yielded IC50 values and its standard error based on 2 independent measurements. F. Fluorescent scans of SDS-PAGE gels after *in vitro* ubiquitylation of fluorescent model peptides harboring either a yGid4 or yGid10-binding sequence by GID^{Ant} (comprising 2 copies each of Gid1 and Gid8, and one copy each of Gid5, Gid2 and Gid9) mixed with either yGid4 (Δ1-115) or yGid10 (Δ1-56) (forming GID^{SR4} or GID^{SR10}, respectively). The model peptides contained a corresponding phage display-determined consensus at the N-terminus connected to C-terminal fluorescein (indicated by an asterisk) with a flexible linker.

ferred instability (Figure S4(B)). At this point, future studies will be required to determine the molecular basis for defective proteasomal targeting. However, given that these sequences increased ubiquitylation *in vitro*, it is possible that accelerated ubiquitylation could impede degradation for example through mis-recruitment of deubiquitylating enzymes, mis-processing by Cdc48,[50] or more trivially, they may be subject to unknown modifications that inhibit binding to or ubiquitylation by the GID E3.

GID E3 supramolecular assembly differentially impacts catalytic efficiency toward different substrates

We were surprised by the differences in IC_{50} values for the naturally occurring degrons from the best-characterized GID E3 substrates, Fbp1 and Mdh2. We thus sought to compare ubiquitylation of the two substrates, which not only display different degrons but also distinct catalytic domains with unique constellations of lysines. Previous studies showed that ubiquitylation of both substrates depends on coordination of degron binding by yGid4 with placement of specific lysines in the ubiquitylation active site.[34,38] However, while GID^{SR4} is competent for Mdh2 degradation *in vivo*, a distinct E3 assembly – wherein the Gid7 subunit drives two GID^{SR4} complexes into an oval arrangement (Chelator-GID^{SR4}) is specifically required for optimal ubiquitylation and degradation of Fbp1.[38] Two yGid4 subunits in Chelator-GID^{SR4} simultaneously bind degrons from the oligomeric Fbp1, for simultaneous ubiquitylation of specific lysines on multiple Fbp1 protomers.

Much like for Fbp1, addition of Gid7 to GID^{SR4} was shown to affect Mdh2 ubiquitylation *in vitro*, albeit in a more nuanced way.[38] As a qualitative test for avid binding to two degrons from Mdh2 (whose dimeric state was confirmed by SEC-MALS (Figure S5(A)) and homology modeling (Figure S5(B))) we performed competition assays with monovalent (GID^{SR4} alone or with addition of a truncated version of Gid7 that does not support supramolecular assembly) and bivalent (GID^{SR4} with Gid7 to form Chelator-GID^{SR4}) versions of the E3, and lysineless monodentate (Mdh2 degron peptide) and bidentate (Mdh2 dimer) inhibitors (Figure S5(C)). While the two inhibitors attenuated ubiquitylation of Mdh2 to a similar extent in reactions with the monovalent E3s, only the full-length Mdh2 complex substantially inhibited the bivalent Chelator-GID^{SR4}. This suggested that Chelator-GID^{SR4} is capable of avidly binding to Mdh2.

Thus, we quantified roles of the Fbp1 and Mdh2 degrons by measuring kinetic parameters upon titrating the two different GID E3 assemblies. In reactions with monovalent GID^{SR4}, the K_m for Mdh2 was roughly 3-fold lower than for Fbp1, in accordance with differences in degron binding (Figure 5(A) and (B)). Although the higher-order Chelator-GID^{SR4} assembly improved the K_m values for Fbp1 and for Mdh2, the extents differ such that the values are similar for both substrates. Formation of the higher-order Chelator-GID^{SR4} assembly also dramatically increased the reaction turnover number (k_{cat}) for Fbp1, with a marginal increase for Mdh2 (8- vs. 1.4- times higher k_{cat}, respectively), which was already relatively high in the reaction with monomeric GID^{SR4} (Figures 5(C) and S4(C)). Combined with its effects on K_m, formation of the Chelator-GID^{SR4} assembly increased catalytic efficiency (k_{cat}/K_m) more than 100-times for Fbp1 and only 6-fold for Mdh2, which may rationalize Gid7-dependency of Fbp1 degradation.

Beyond avid substrate binding, the multipronged targeting of Fbp1 by Chelator-GID^{SR4} involves proper orientation of the substrate so that specific lysines in metabolic regulatory regions are simultaneously ubiquitylated.[38] To explain the lesser effect of Chelator-GID^{SR4} on catalytic efficiency toward Mdh2, we examined structural models. Briefly, after docking two substrate degrons into opposing yGid4 protomers, we rotated the tethered substrate to place the targeted lysines in the ubiquitylation active sites (Figure S5(E) and (F)). As shown previously, docking either Fbp1 targeted lysine cluster (K32/K35 and K280/K281) places the other in the opposing active site (Figures 5(D) and S5(E)). For Mdh2, upon mutating the individual clusters of preferentially targeted lysines determined previously,[34] we found that K330 is the major ubiquitylation target for Chelator-GID^{SR4} (Figure S5(D)). However, the structural locations of the two K330 residues within the Mdh2 dimer precludes their simultaneously engaging both Chelator-GID^{SR4} active sites (Figures 5(D) and S5(F)). Thus, the distinct constellations of targeted lysines may also contribute to differences in ubiquitylation efficiency.

Degron identity determines K_m for ubiquitylation but differentially impacts glucose-induced degradation of Mdh2 and Fbp1

To assess the roles of differential degron binding in the distinct contexts provided by the Fbp1 and Mdh2 experiments, we examined the effects of swapping their degrons. We first performed qualitative ubiquitylation assays using the simpler GID^{SR4} E3 ligase. Comparing ubiquitylation of fluorescently-labeled Fbp1 and Mdh2 side-by-side showed more Mdh2 is ubiquitylated with more ubiquitins during the time-course of reactions.[38] These properties are reversed when the N-terminal sequence of Mdh2 is substituted for the Fbp1 degron and vice-versa (Figure 6(A)).

Quantifying the K_m values showed that the values for degron-swapped substrates roughly scaled with degron identity (Figures 6(B) and S4(D); for Mdh2 $K_m \approx 1.3$ μM, for degron-swapped $Fbp1^{Mdh2\ degron}$ $K_m \approx 0.8$ μM, for Fbp1 $K_m \approx 3.6$ μM, for degron-swapped $Mdh2^{Fbp1\ degron} \approx 3.5$ μM). Furthermore,

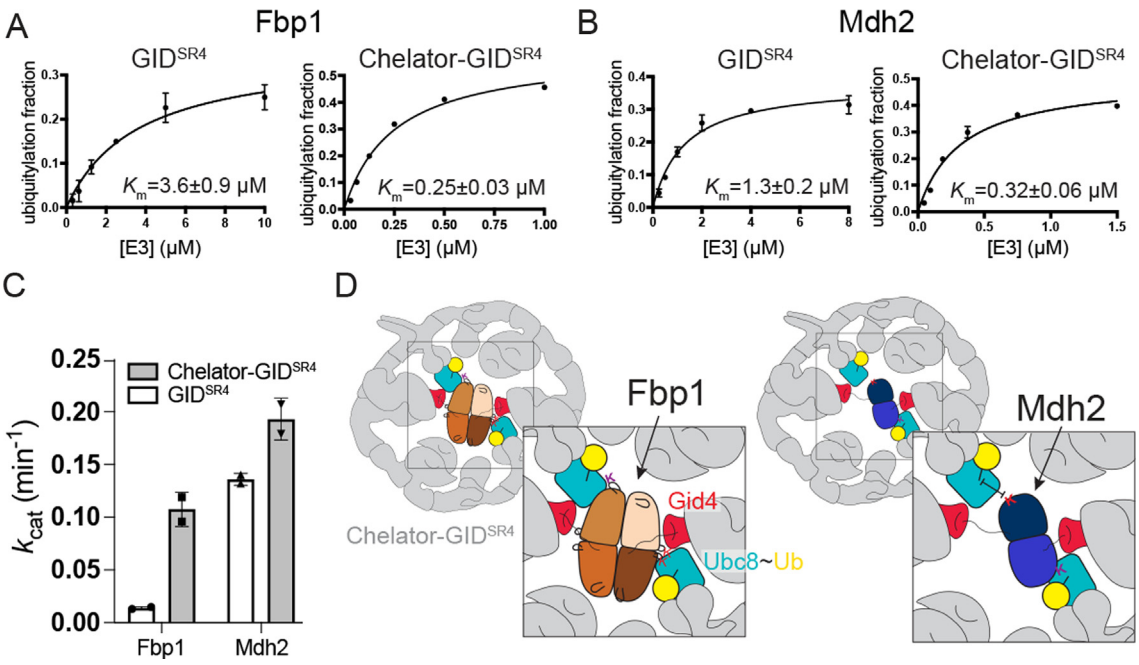

Figure 5. Differential targeting of Mdh2 and Fbp1 by GID E3. A. Plots showing fraction of *in vitro*-ubiquitylated Fbp1 as a function of varying concentration of GID E3 in either its monomeric GID^{SR4} or higher-order Chelator-GID^{SR4} form (co-expressed GID^{SR4} + Gid7). Fitting to Michaelis-Menten equation yielded K_m values. Error bars represent standard deviation ($n = 2$). B. Plots as in (A) but analyzing Mdh2 ubiquitylation. C. Comparison of k_{cat} values for Fbp1 and Mdh2 ubiquitin targeting by GID^{SR4} and Chelator-GID^{SR4} based on a time-course of substrate ubiquitylation (Figure S4(C)). D. Cartoons representing ubiquitylation of Fbp1 and Mdh2 by Chelator-GID^{SR4} based on structural modeling (Figure S5(E) and (F)).

as expected, the K_m values for all substrates improved in reactions with Chelator-GID^{SR4}. However, the relative impact seemed to scale with the way in which they are presented from the folded domain of a substrate rather than the degrons themselves (roughly 14-fold for Fbp1 and 11-fold for Fbp1$^{Mdh2\ degron}$ versus 4-fold for Mdh2 and 6-fold for Mdh2$^{Fbp1\ degron}$).

Effects *in vivo* were examined by monitoring glucose-induced degradation of the wild-type and mutant substrates with the promoter-reference technique.[6,46] As shown previously, Mdh2 was rapidly degraded in the wild-type yeast and the ΔGid7 strain (Figure 6(C)).[38] However, turnover of the mutant version bearing the weaker Fbp1 degron was significantly slower in both genetic backgrounds. Thus, the Mdh2 degron is tailored to the Mdh2 substrate. In striking contrast, although the Mdh2 degron did subtly impact degradation of Fbp1, it was not sufficient to overcome dependency on Gid7 (Figure 6(D)). Thus, substrate ubiquitylation, and turnover, depend not only on degron identity, but also on their associated targeted domains.

Discussion

Overall, our study leads to several conclusions. First, GID/CTLH E3 substrate receptors recognize a diverse range of N-terminal sequences, dictated not only by the N-terminal residue, but also the pattern of downstream amino acids (Figures 1 and S1). Second, such diverse N-terminal sequence recognition is achieved by the combination of (1) a deep substrate-binding tunnel culminating in conserved Glu and Tyr side-chains recognizing the N-terminal amine, (2) pliable loops at the entrance to the substrate binding tunnel that conform to a range of downstream sequences, and (3) the binders themselves forming distinct extended conformations that likewise complement the receptor structures (Figure 3). Remarkably, the hGid4 loops and the bound peptide reciprocally affect each other – peptide binding induces folding of the flexible loops whereas the arrangement of the loops dictates affinity for the bound peptide. This correlation rationalizes strong dependence of Gid4 specificity on the peptide sequence context. Third, the range of interactions result in a range of affinities (Figures 2, 4 and S2(A)). Notably, our randomized phage-display peptide library screen identified far tighter binders to yGid4 than known natural degrons. This approach also generated yGid10-binding sequences with affinities similar to or greater than the only known natural degron, and with significantly higher affinity than a sequence identified by yeast two-hybrid screening. Phage-display peptide library screening may thus prove to be a generally useful method for identifying E3

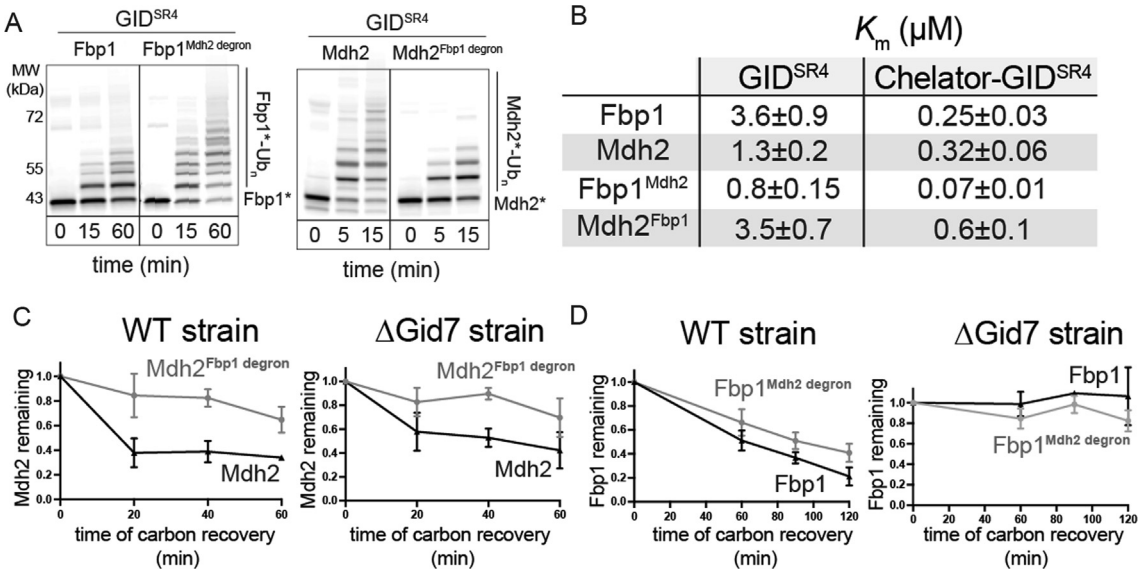

Figure 6. Combinatorial nature of substrate recognition by GID. A. Qualitative *in vitro* ubiquitylation assay probing effect of degron exchange between Fbp1 and Mdh2. Both WT and degron-swapped versions of Fbp1 and Mdh2 were C-terminally labelled with fluorescein (indicated by an asterisk) and ubiquitylated by GID^{SR4}. B. Table summarizing values of K_m for ubiquitylation of WT and degron-swapped substrates by the two versions of GID based on the plots in Figure S4(D). C. *In vivo* glucose-induced degradation of exogenously expressed and C-terminally 3xFlag-tagged Mdh2 as well as its degron-swapped versions quantified with a promoter-reference technique. Levels of the substrates (relative to the level of DHFR) at different timepoints after switch from gluconeogenic to glycolytic conditions were divided by their levels before the switch (timepoint 0). For each substrate, the experiment was performed in WT and ΔGid7 yeast strains. Error bars represent standard deviation ($n = 3$), whereas points represent the mean. D. *In vivo* assay as in (C) but with WT and degron-swapped Fbp1.

ligase binders. Fourth, degron binding is only part of substrate recognition by GID E3s (Figures 5 and 6). Rather, ubiquitylation and degradation depend on both the pairing of a degron with a substrate domain that presents lysines in a particular constellation, and configuration of the GID E3 in either a simplistic monovalent format or in a multivalent chelator assembly specialized for targeting some but not all oligomeric substrates.

Some features of the high-affinity peptide binding by Gid4s and yGid10 parallel other end-degron E3s. Although ubiquitin ligases in the Ubr family employ UBR-box 1 and UBR-box 2 domains with a shallower modes of N-degron recognition,[51–57] C-degron recognition by several cullin-RING ligase substrate receptors involves terminal peptide binding within deep clefts or tunnels[58–61] much like the high-affinity binder interactions with Gid4s and yGid10. Furthermore, end-degron E3 ligases use different strategies to recognize diverse degron sequences. For example, a single Ubr-family E3 can bind different N-terminal sequences through distinct N-degron-binding domains.[62–64] However, much like Gid4s and yGid10 recognize diverse N-terminal sequences, the substrate-binding site of a single cullin-RING ligase was recently shown to bind interchangeably to a C-degron or to a different substrate's internal sequence.[60,61,65]

To-date, few GID E3 substrates have unambiguously been identified. Thus, our findings may have implications for identifying new substrates. Most of the currently characterized substrates depend on co-translational generation of an N-terminal Pro. However, sequences initiating with bulky hydrophobic residues may be refractory to N-terminal processing enzymes such as Met aminopeptidases.[47] Nonetheless, post-translational processing could generate such N-termini. Several paradigms for post-translational generation of N-degrons have been established by studies of Ubr1 substrates. First, endoproteolytic cleavage – by caspases, calpains, separases, cathepsins and mitochondrial proteases[37,66–71] – is responsible for the generation of myriad Arg/N-degron pathway substrates recognized by some Ubr-family E3s.[9] Similarly, N-terminal trimming by aminopeptidases has recently been reported to expose Pro/N-degrons of two yGid4 substrates.[72] Notably, 15 hGid4 interactors reported in the BioGRID database[73] have a solvent-exposed internal [FIL]-D-[VIL] sequence (Figure S6), raising the possibility that the newly identified Gid4-and yGid10-binding motifs likewise could be exposed upon post-translational proteolytic cleavage. Second, some N-degrons are created by aminoacyl-tRNA protein transferases-catalyzed appendage of an

additional amino acid at the protein's N-terminus.[64,74] The bacterial N-degron pathway involves conjugation of hydrophobic residues such as Phe and Leu,[75,76] hence it is tempting to speculate that hydrophobic N-degrons in eukaryotes could likewise involve such N-terminal amino acid addition. Finally, yeast Ubr1 is modulated in an intricate manner: after HtrA-type protease cleavage, a portion of the protein Roq1 binds Ubr1 and alters its substrate specificity.[77] Notably, proteomic studies showed that the human CTLH complex itself associates with the HtrA-type protease HTRA2,[22,24,78–80] known to be involved in mitochondrial quality control.[81,82] This raises the tantalizing possibility that the CTLH E3 might form a multienzyme targeting complex that integrates a regulatory cascade to generate its own substrates or regulatory partners.

The identified sequences might also play various non-degradative functions. Some tight binders to other E3 ligases are pseudosubstrates that modulate subcellular localization,[83,84] or inhibit activity.[85–87] Irrespective of whether such sequences target endogenous proteins to GID/CTLH-family E3 ligases, the identification of nanomolar hGid4 binders and the structural insight into the substrate receptor plasticity may be useful for development of small molecules targeting these E3s.

Finally, our examination of degron-swapped GID E3 substrates Fbp1 and Mdh2 showed that N-terminal sequence is only part of the equation determining ubiquitylation and subsequent degradation. Mdh2 required its own degron and its ubiquitylation and degradation were impaired when substituted with the weaker degron from Fbp1, irrespective of capacity for GID^{SR4} to undergo Gid7-mediated superassembly. However, while either degron could support Fbp1 targeting, this requires Gid7-dependent formation of the chelate-like E3 configuration. Taken together, our data reveal that structural malleability of both the substrate receptor and the E3 supramolecular assembly endows GID E3 complexes – and presumably CTLH E3s as well – capacity to conform to diverse substrates, with varying degrons and associated targeted domains. Such structural malleability raises potential for regulation through modifications or interactions impacting the potential conformations of both the substrate binding domains and higher-order assemblies, and portends future studies will reveal how these features underlie biological functions of GID/CTLH E3s across eukaryotes. Moreover, our results highlight that turnover depends on structural complementarity between E3 and both the substrate degron and ubiquitylated domains, a principle of emerging importance for therapeutic development of targeted protein degradation.

Methods

Reagent table

Reagent/Resource	Reference or Source	Identifier or Catalog Number
Experimental models, cell lines and strains		
High Five Insect cells	Thermo Fisher	Cat#B85502
Saccharomyces cerevisiae: Strain S288C: BY4741; MATa his3Δ1leu2Δ0 met15Δ0 ura3Δ0	Euroscarf	Cat#Y00000
CRLY12; BY4741, Gid4::KANMX	38	N/A
CRLY14; BY4741, Gid7::KANMX	38	N/A
Recombinant DNA		
pCSJ95	6	N/A
pCSJ125	6	N/A
DSJC3; pRS313-pGPD-MPHSVTP-Fbp1(Δ1-7)-3xFLAG-CYC-pGPD-DHFR-HA-CYC	This study	N/A
DSJC4; pRS313-pGPD-MPTLVNG-Mdh2(Δ1-7)-3xFLAG-CYC-pGPD-DHFR-HA-CYC	This study	N/A
DSJC5; pRS313-pGPD-Ub-FDITGFSW-Fbp1(Δ1-9)-3xFLAG-CYC-pGPD-DHFR-HA-CYC	This study	N/A
DSJC6; pRS313-pGPD-Ub-LDVSWFEW-Fbp1(Δ1-9)-3xFLAG-CYC-pGPD-DHFR-HA-CYC	This study	N/A
DSJC7; pRS313-pGPD-Ub-IGLW-Fbp1(Δ1-5)-3xFLAG-CYC-pGPD-DHFR-HA-CYC	39	N/A
pLIB Gid4	34	N/A
pLIB Gid7	38	N/A
pBIG2 Gid1:Gid8-TEV-2xS:Gid5:Gid2:Gid9:Gid7	38	N/A
pBIG2 Gid1:Gid8-TEV-2xS:Gid5:Gid4:Gid2:Gid9:	38	N/A

(*continued*)

Reagent/Resource	Reference or Source	Identifier or Catalog Number
Gid7		
pBIG2 Gid1:Gid8-TEV-2xS:Gid5:Gid4:Gid2:Gid9	34	N/A
pBIG2 Gid1:Gid8-TEV-2xS:Gid5:Gid2:Gid9	34	N/A
pGEX GST-TEV-hGid4 (Δ1-115)	This study	N/A
pGEX GST-TEV-Gid7	38	N/A
pGEX GST-TEV-Gid7 (Δ1-285)	38	N/A
pGEX GST-TEV-hGid4 (Δ1-99)	38	N/A
pGEX GST-TEV-hGid4 (Δ1-120, Δ294-300)	This study	N/A
pGEX GST-TEV-yGid4 (Δ1-115)	34	N/A
pGEX GST-TEV-yGid10 (Δ1-57)	34	N/A
pGEX GST-TEV-yGid10 (Δ1-64, Δ285-292)	This study	N/A
pRSF Fbp1-GGGGS-sortag-6xHis	38	N/A
pRSF Mdh2-GGGGS-LPETGG-6xHis	34	N/A
pRSF MPHSVTP-Fbp1 (Δ1-7)-GGGGS-LPETGG-6xHis	This study	N/A
pRSF MPTLVNG-Mdh2 (Δ1-7)-GGGGS-sortag-6xHis	This study	N/A
pRSF GST-TEV-SUMO- FDITGFSW-Fbp1(Δ1-9)-GGGGS-sortag-6xHis	This study	N/A
pRSF Ubc8-6xHis	34	N/A
pRSF 6xHis-hGid4 (Δ1-115)	This study	N/A
pET3b Ub (ubiquitin)	34	N/A
pET29 sortase A	89	N/A
pRSF Mdh2-6xHis	34	N/A
pRSF Mdh2-6xHis K254R/K256R/K259R	This study	N/A
pRSF Mdh2-6xHis K330R	This study	N/A
pRSF Mdh2-6xHis K360R/K361R	This study	N/A
pRSF Mdh2-6xHis K254R/K256R/K259R; K330R; K360R/K361R	34	N/A
Antibodies		
Mouse anti-His	Cell Signaling Technology	Cat#9991
Sheep polyclonal anti-hGid4	38	N/A
Monoclonal ANTI-FLAG M2	Sigma Aldrich	Cat#F1804
Rabbit anti-HA	Sigma Aldrich	Cat#H6908
Goat anti-rabbit IgG Dylight488 conjugated	Invitrogen	Cat#35552
Goat anti-mouse IgG Dylight633 conjugated	Invitrogen	Cat#35512
Goat anti-mouse IgG HRP conjugated	Sigma Aldrich	Cat#A4416; PRID
Chemicals, Enzymes and peptides		
complete EDTA free	Roche	Cat#05056489001
Aprotinin from bovine lung	Sigma	A1153-10MG
Leupeptin	Sigma	L2884-250MG
Benzamidine	Sigma	B6506-25G
GGGGGFYVK-FAM	MPIB	N/A
PGLWKS	MPIB	N/A
IGLWKS	MPIB	N/A
Leu-Gly	Sigma	CAS# 686–50-0
Pro-Gly	Sigma	CAS# 2578–57-6
Ala-Gly	MPIB	CAS# 687–69-4
Gly-Gly	MPIB	CAS# 556–50-3
GVATSLLW	MPIB	N/A
FDVSWFMG	MPIB	N/A
PDVSWFMG	MPIB	N/A
LDVSWFMG	MPIB	N/A
VDVNSLWA	MPIB	N/A
WDVSWV	MPIB	N/A
FDITGFS	MPIB	N/A

(*continued on next page*)

(*continued*)

Reagent/Resource	Reference or Source	Identifier or Catalog Number
GWLPPNLW	MPIB	N/A
PGILGSW	MPIB	N/A
FWLPANLW	MPIB	N/A
PHSVTPWSI	MPIB	N/A
PTLVNGWPR	MPIB	N/A
PIPVGNWTK	MPIB	N/A
VWEVKTNQ	MPIB	N/A
PHSVTPSIEQDSLK	MPIB	N/A
PGLWKS-FAM	MPIB	N/A
GGGGRHDS(P)GLDS(P)MKDEE-FAM	MPIB	N/A
FDITGFSWRDSTEGFTGRGWSGRGWSKGGK-FAM	MPIB	N/A
GWLPPNLWRDSTEGFTGRGWSGRGWSKGGK-FAM	MPIB	N/A
Software		
Phyre[2]	90	http://www.sbg.bio.ic.ac.uk/~phyre2/html/page.cgi?id=index
UCSF Chimera	91	https://www.cgl.ucsf.edu/chimera/
UCSF ChimeraX	92	https://www.rbvi.ucsf.edu/chimerax/
PyMOL v2.1	Schrödinger	https://pymol.org/2/
Coot	93,94	https://www2.mrc-lmb.cam.ac.uk/personal/pemsley/coot/
Phenix	95–97	https://www.phenix-online.org/
Image Studio	LI-COR Biosciences	https://www.licor.com/bio/image-studio/
Fiji/ImageJ	98	https://imagej.net/
GraphPad Prism version 8.0	GraphPad Software	www.graphpad.com
ImageQuant TL Toolbox version 8.2	GE Healthcare	
MicroCal PEAQ-ITC Analysis Software	Malvern Panalytical	

Plasmid preparation and mutagenesis

All the genes encoding yeast GID subunits including the substrate receptors yGid4 and yGid10, as well as Fbp1 and Mdh2 substrates were amplified from *S. cerevisiae* BY4741 genomic DNA. The gene encoding hGid4 was codon-optimized for bacterial expression system and synthesized by GeneArt (Thermo Fisher Scientific).

All the recombinant constructs used for protein expression were generated by Gibson assembly method[99] and verified by DNA sequencing. The GID subunits were combined using the biGBac method[100] into a single baculoviral expression vector. All the plasmids used in this study are listed in the Reagent table.

Bacterial protein expression and purification

All bacterial expressions were carried out in *E. coli* BL21 (DE3) RIL cells in a Terrific Broth medium[101] overnight at 18 °C. All versions of yGid4, yGid10 and hGid4 (except for that used for NMR) were expressed as GST-TEV fusions. The harvested cell pellets were resuspended in the lysis buffer (50 mM HEPES pH 7.5, 200 mM NaCl, 5 mM DTT and 1 mM PMSF), disintegrated by sonication and subjected to glutathione affinity chromatography, followed by overnight cleavage of the eluted proteins at 4 °C with tobacco etch virus[87] protease to release the GST tag. Final purification was performed with size exclusion chromatography (SEC) in the final buffer containing 50 mM HEPES pH 7.5, 200 mM NaCl and 1 mM or 5 mM DTT (for assays and crystal trials, respectively), or 0.5 mM TCEP (for ITC binding assay). Additionally, pass-back over glutathione affinity resin was performed in order to get rid of the remaining uncleaved GST-fusion protein and free GST.

All versions of Ubc8, Fbp1 (except for FDITGFSW-Fbp1) and Mdh2 were expressed with a C-terminal 6xHis tag. The harvested cell pellets were resuspended in the lysis buffer (50 mM HEPES pH 7.5, 200 mM NaCl, 5 mM β-mercaptoethanol, 10 mM imidazole and 1 mM PMSF) and sonicated. Proteins were purified by nickel affinity chromatography, followed by anion exchange and SEC in the final buffer containing 50 mM HEPES pH 7.5, 200 mM NaCl and 1 mM DTT.

To purify FDITGFSW-Fbp1 for fluorescein labeling, it was expressed as N-terminal GST-SUMO fusion. After glutathione affinity chromatography, the GST-SUMO tag was cleaved

off with a SUMO-specific protease SENP2 generating a desired N-terminus. After cleavage, FDITGFSW-Fbp1 was further purified by SEC in the final buffer containing 50 mM HEPES pH 7.5, 200 mM NaCl and 1 mM DTT. The uncleaved GST-SUMO fusion and free GST-SUMO was removed by pass-back over the GST resin.

Untagged WT ubiquitin used for *in vitro* assays was purified via glacial acetic acid method,[102] followed by gravity S column ion exchange chromatography and SEC.

Insect cell protein expression and purification

All yeast GID complexes used in this study were expressed in insect cells. For protein expression, Hi5 insect cells were transfected with recombinant baculovirus variants and grown for 60–72 h in EX-CELL 420 Serum-Free Medium at 27 °C**.** The insect cells were harvested by centrifugation at 450xg for 15 min and pellets were resuspended in a lysis buffer (50 mM HEPES pH 7.5, 200 mM NaCl, 5 mM DTT, 10 μg/ml leupeptin, 20 μg/ml aprotinin, 2 mM benzamidine, EDTA-free complete protease inhibitor tablet (Roche, 1 tablet per 50 ml of buffer) and 1 mM PMSF). All the complexes were purified from insect cell lysates by StrepTactin affinity chromatography by pulling on a twin-Strep tag fused to the Gid8 C-terminus. Further purification was performed by anion exchange chromatography and SEC in the final buffer containing 25 mM HEPES pH 7.5, 200 mM NaCl and 1 mM DTT.

Preparation of fluorescent substrates for in vitro activity assays

C-terminal labelling of Fbp1, Mdh2 and their degron-swapped versions with fluorescein was performed through a sortase A-mediated reaction. The reaction mix contained 50 μM substrate (C-terminally tagged with a sortag (LPETGG) followed by a 6xHis tag), 250 μM fluorescent peptide (GGGGGFYVK-FAM), 50 μM sortase A[89] and a reaction buffer (50 mM Tris pH 8, 150 mM NaCl and 10 mM $CaCl_2$). The reaction was carried out at room temperature for 30 min. After the reaction, a pass-back over Ni-NTA resin was done to get rid of unreacted substrates. Further purification was done with SEC in the final buffer containing 50 mM HEPES pH 7.5, 200 mM NaCl and 1 mM DTT.

^{15}N labelling of hGid4

For NMR experiments, ^{15}N-labeling of 6xHis-hGid4 (Δ1-115) was carried out. Firstly, 50 ml of the preculture was spun at 3000 rpm for 20 mins. The supernatant was then removed and resuspended with 1x M9 cell growth medium (2 g glucose, 5 mg/ml thiamine chloride, 1 M $MgSO_4$, 1 M $CaCl_2$ and 1g $^{15}NH_4Cl$ per liter of 1x M9 medium) containing all essential ions and antibiotics. The cultures were then grown at 37 °C and 200 rpm until it reached the OD_{600} of 0.5–0.8. Subsequently, the temperature was reduced to 23 °C and kept for an hour before inducing with 0.6 M IPTG. The cultures were then kept growing overnight at 23 °C, 200 rpm, harvested and used for protein purification as described in the section "Protein expression and purification" but in the final SEC buffer containing 25 mM phosphate buffer pH 7.8, 150 mM NaCl and 1 mM DTT.

NMR (Nuclear Magnetic Resonance) spectroscopy

NMR experiments were recorded at 298 K on Bruker Avance III 600 MHz spectrometer (at ^{1}H Larmor frequency of 600 MHz) equipped with a 5 mm TCI cryoprobe. Samples at 0.1 mM ^{15}N-labeled hGid4 were prepared in NMR buffer (50 mM HEPES, 100 mM NaCl, pH 7.0) supplemented with 10% D_2O. ^{1}H,^{15}N HSQC (heteronuclear single quantum coherence) correlation spectra were acquired with 2048 × 256 complex points and a recycle delay of 1.2 s, with 24 scans. DMSO references were acquired at the beginning and end of the assay. No differences were observed between them. Spectra in the presence of ligands where measured at 1 mM Pro or Pro-Gly and 0.5 mM PGLWKS peptide.

Phage-displayed N-terminal peptide library construction and selections

A diverse octapeptide N-terminal phage-displayed library was generated for the identification of peptides binding to hGid4 (Δ1-99), yGid4 (Δ1-115) and yGid10 (Δ1-56). An IPTG-inducible P_{tac} promoter was utilized to drive the expression of open-reading frames encoding the fusion proteins in the following form: the stII secretion signal sequence, followed by a random octapeptide peptide, a GGGSGGG linker and the M13 bacteriophage gene-8 major coat protein (P8). The libraries were constructed by using oligonucleotide-directed mutagenesis with the phagemid pRSTOP4 as the template, as described.[103] The mutagenic oligonucleotides used for library construction were synthesized using with NNK degenerate codons (where N = A/C/G/T & K = G/T) that encode all 20 genetically encoded amino acids. The diversity of the library was 3.5×10^9 unique peptides.

The N-terminal peptide library was cycled through five rounds of binding selections against immobilized GST-tagged hGid4, yGid4, and yGid10, as described.[44] Pre-incubation of the phage pools against immobilized GST was performed before each round of selections to deplete non-specific binding peptides. For rounds four and five, 48 individual clones were isolated and tested for binding to the corresponding targets by phage ELISA,[104] and clones with a strong and specific pos-

itive ELISA signal were Sanger sequenced. A total of 41, 12, and 12 unique peptide sequences were identified binding to hGid4, yGid4, and yGid10, respectively, and their sequences were aligned to identify common specificity motifs.

Oligonucleotide used for the Kunkel reaction to construct the library:

GCTACAAATGCCTATGCANNKNNKNNKNNKN NKNNKNNKNNKGGTGGAGGATCCGGAGGA.

Fluorescence polarization (FP) assays

To determine conditions for a competitive FP assay, we first performed the experiment in a non-competitive format. A 2-fold dilution series of hGid4 (Δ1-115) was prepared in the FP buffer containing 25 mM Hepes pH 7.5, 150 mM NaCl, 0.5 mM DTT and 20 nM fluorescent PGLWKS-FAM and a non-binding GGGGRHDS(P)GLDS(P) MKDEE-FAM as a control peptide. The mixed samples were equilibrated at room temperature for 5 min before transferring to Greiner 384-well flat bottom black plates. Then, the polarization values were measured at the excitation and emission wavelengths of 482 nm and 530 nm, respectively using CLARIOstar microplate reader (BMG LABTECH). For each run, the gain was recorded with FP buffer-only control. The data were fit to one site-binding model in GraphPad Prism to determine K_D value.

To compare binding of several unlabeled ligands to hGid4, we performed the FP measurements in a competitive format. Based on the FP plot from hGid4 titration experiment, we identified hGid4 concentration, which resulted in ~60% saturation of the FP signal. Next, 2-fold dilution series of unlabeled competitors was prepared in the FP buffer mixed with 6.8 μM hGid4. After 5 min incubation, the measurement was performed as described above. The data were plotted relative to the FP signal in the absence of an inhibitor as a function of log(ligand concentration) and analyzed with log(inhibitor) vs. response model to determine IC50 values. To determine relative inhibitory strength of the ligands, the determined IC50 values were divided by that of PGLWKS.

Screening of PGLWKS sequence for hGid4 binding using peptide spot array

The array of peptides derived from the PGLWKS sequence with all 20 amino acid substituted at positions 1, 2 and 3 together, 4 and 5 were synthesized on a membrane in the MPIB biochemistry core facility . The membrane blot was first blocked with 3% milk in TBST buffer (20 mM Tris, 150 mM NaCl and 0.1% Tween 20) for 1 h at room temperature. hGid4 (Δ1-99) was diluted to 10 μg/ml in the buffer containing 150 mM NaCl, 25 mM HEPES pH 7.5, 0.5 mM EDTA pH 8.0, 10% glycerol, 0.1% Tween 20, 2% milk and 1 mM DTT and incubated with the blocked membrane overnight at 4 °C with gentle shaking. The membrane was then washed with TBST buffer 3 times, incubated with primary anti-hGid4 sheep polyclonal antibody (1:500) for 3 h with gentle shaking, followed by multiple washing steps with TBST and 1 h incubation with secondary HRP-conjugated anti-sheep (1:5000) antibody. The membranes were again washed multiple times with TBST and hGid4 binding was visualized by chemiluminescence in Amersham Imager 800 (Cytiva).

Isothermal titration calorimetry (ITC) binding assays

To quantify binding of peptides to hGid4 (Δ1-115) and yGid10 (Δ1-56), we employed ITC. All peptides were dissolved in the SEC buffer used for purification of substrate receptors containing 25 mM HEPES pH 7.5, 150 mM NaCl and 0.5 mM TCEP and their concentration was measured by absorbance at 280 nm (if not present in the original sequence, a single tryptophan residue was appended at peptides' C-termini to facilitate determination of peptide concentration). Binding experiments were carried out in the MicroCal PEAQ-ITC instrument (Malvern Pananalytica) at 25 °C by titrating peptides to either hGid4 or yGid10. Peptides were added to individual substrate receptors using 19 × 2 μl injections, with 4 s injection time and 150 s equilibration time between the injections. The reference power was set to 10 μcal/s. The concentration of the peptides and substrate receptors were customized according the estimated K_D values. Raw ITC data were analyzed using One-Set-of-Sites binding model (Malvern Pananalytica) to determine K_D and stoichiometry of the binding events (N). All plots presented in figures were prepared in GraphPad Prism.

Size exclusion chromatography with multiangle light scattering (SEC-MALS)

To determine the oligomeric state of Mdh2, we performed SEC-MALS (conducted in the MPIB Biochemistry Core Facility). For each run, 100 μl Mdh2 at 1 mg/mL were injected onto Superdex 200 column equilibrated with a buffer containing 25 mM HEPES pH 7.5, 150 mM NaCl and 5 mM DTT.

In vitro activity assays

All ubiquitylation reactions were performed in a multi-turnover format in the buffer containing 25 mM HEPES pH 7.5, 150 mM NaCl, 5 mM ATP and 10 mM $MgCl_2$. To quench the reactions at indicated timepoints, an aliquot of the reaction mix was mixed with SDS-PAGE loading buffer. Ubiquitylation of fluorescein-labelled substrates was visualized with a fluorescent scan of an SDS-

PAGE gel with a Typhoon imager (GE Healthcare) and quantified with ImageQuant (GE Healthcare; version 8.2).

To verify whether FDITGFSW and GWLPPNLW can be recognized by, respectively, yGid4 and yGid10 during ubiquitylation reaction (Figure 4(D)), we performed an *in vitro* activity assay with model peptides, consisting of the respective N-terminal sequences connected to a single acceptor lysine with a 23-residue linker and C-terminal fluorescein (the length of the linker was optimized based on the GID^{SR4} structure[38]). To start the reaction, 0.2 μM E1 Uba1, 1 μM E2 Ubc8-6xHis, 0.5 μM E3 GID^{Ant}, 20 μM ubiquitin, 1 μM yGid4 (Δ1-115) or yGid10 (Δ1-56) and 1 μM peptide substrate were mixed and incubated at room temperature.

In order to probe avid binding of Mdh2 to Chelator-GID^{SR4}, we employed a competition ubiquitylation assay (Figure S4(C)). The reactions were initiated by mixing 0.2 μM Uba1, 1 μM Ubc8-6xHis, 0.5 μM E3 GID^{SR4}, 0 or 2 μM Gid7 (WT or its N terminal deletion mutant, Δ1-284), 0.5 μM Mdh2-FAM, 20 μM unlabeled competitor (dimeric Mdh2-6xHis or a peptide comprising Mdh2 N-terminal sequence PHSVTPSIEQDSLK) and 20 μM ubiquitin. GID^{SR4} was incubated with Gid7 for 5 min on ice before the start of the reaction.

To test which of the preferred ubiquitylation sites within Mdh2 determined previously for GID^{SR4}[34] are major ubiquitylation targets of Chelator-GID^{SR4}, we performed an activity assay with WT and mutant Mdh2, in which putative target lysine clusters (K254/K256/K259; K330; K360/K361) were mutated to arginines individually and all together (Figure S5(A)). To start the reaction, 0.2 μM Uba1, 1 μM Ubc8-6xHis, 0.1 μM Chelator-GID^{SR4}, 1 μM WT or mutant Mdh2-6xHis and 20 μM ubiquitin were mixed. After quenching, Mdh2-6xHis and its ubiquitylated versions were visualized by immunoblotting with anti-6xHis primary antibody and HRP-conjugated anti-mouse secondary antibody.

To quantitatively compare recognition of phage display-identified sequences and degrons of natural GID substrates by yGid4, we employed competitive ubiquitylation assays (Figure 4(F)). Unlabeled peptide inhibitors comprising the analyzed sequences were titrated to compete off binding of Mdh2-FAM to GID^{SR4}, thus attenuating its ubiquitylation. Reactions were started by addition of 20 μM ubiquitin to the mixture of 0.2 μM E1 Uba1, 1 μM E2 Ubc8-6xHis, 0.5 μM E3 GID^{Ant}, 1 μM yGid4 (Δ1-115), 0.25 μM Mdh2-FAM and various concentrations of peptide competitors. After 3 min, the reactions were quenched so that their velocities were still in the linear range. The fractions of ubiquitylated Mdh2 in the presence of an inhibitor were divided by that for Mdh2 alone and plotted against peptide concentration. Fitting of the data to [inhibitor] vs. response model in GraphPad Prism yielded IC50 values.

To qualitatively compare degrons of Fbp1 and Mdh2 in the context of full-length substrates (Figure 6(A)), we performed activity assay with WT and degron-swapped versions ($Fbp1^{Mdh2\ degron}$ and $Mdh2^{Fbp1\ degron}$) of the substrates by mixing 0.2 μM E1 Uba1, 1 μM E2 Ubc8-6xHis, 1 μM E3 GID^{Ant}, 2 μM yGid4 (Δ1-115), 0.5 μM WT or mutant version of Fbp1-FAM or Mdh2-FAM and 20 μM ubiquitin. Similarly, we tested if the N-terminal FDITGFSW motif can promote *in vitro* ubiquitylation of Fbp1. The reactions contained 0.2 μM E1 Uba1, 1 μM E2 Ubc8-6xHis, 0.1 μM GID^{SR4} or Chelator-GID^{SR4}, 1 μM of WT or mutant Fbp1 and 20 μM ubiquitin.

Kinetic parameters for ubiquitylation of WT and degron-swapped versions of Fbp1 and Mdh2 were determined as described previously.[38] Briefly, to determine Michaelis-Menten constant (K_m), we titrated E3 (GID^{SR4} or Chelator-GID^{SR4}) at constant substrate concentration kept below K_m (0.5 and 0.1 μM for reactions with GID^{SR4} and Chelator-GID^{SR4}, respectively; Figures 5(A), (B) and S4(E)). The reaction time was optimized so that the velocity of all reactions was in the linear range. The fraction of ubiquitylated substrate was calculated and plotted as a function of E3 concentration in GraphPad Prism and fit to Michaelis-Menten equation to determine K_m. To calculate k_{cat}, time course assays were performed with the ratios of [E3]:K_m and [substrate]:K_m kept the same for all substrates and E3 versions (2.7 and 0.4, respectively; Figure 5(C)). The rates of the reactions were calculated by linear regression in GraphPad Prism from plots of fraction of ubiquitylated substrates vs. reaction time (Figure S4(D)) and converted into initial velocity using the following equation: $V_0 = rate \cdot [substrate]$.

Then, V_{max} was estimated using a modified form of the Michaelis-Menten equation:

$V_{max} = \frac{V_0 \cdot (K_m + [substrate])}{[substrate]}$. To obtain k_{cat} values, V_{max} was divided by the E3 concentration: $k_{cat} = \frac{V_{max}}{[E3]}$.

Yeast strain construction and growth conditions

The yeast strains used in this study are specified in the Reagents table. All the yeast strains were constructed as derivatives of BY4741 using standard genetic techniques and were verified using PCR, DNA sequencing and immunoblotting to confirm protein expression.

In vivo yeast substrate degradation assays

In order to test the effect of degron identity on glucose-induced degradation of GID substrates, we monitored turnover of WT and degron-exchanged versions of Mdh2 and Fbp1, using the promoter reference technique.[46] Initially, WT and ΔGid7 yeast strains were transformed with a plasmid harboring the open reading frame of either Fbp1-3xFLAG, Mdh2-3xFLAG or their mutant versions ($Fbp1^{Mdh2\ degron}$-3xFLAG and $Mdh2^{Fbp1\ degron}$-3xFLAG) and the control protein DHFR-3xHA, both

expressed from identical promoters. Cells were then grown in SD-glucose medium to OD^{600} of 1.0 followed by carbon starvation in SE medium (0.17% yeast nitrogen base, 0.5% ammonium sulfate, 2% ethanol, amino acid mix) for 19 h. Next, yeasts at the equivalent of 1 OD_{600} were transferred to SD-glucose medium containing 0.5 mM tetracycline resulting in translation inhibition induced by its binding to specific RNA-aptamers within ORFs of the examined and control proteins. At the indicated time points, 1 mL of cells were harvested and pellets were flash frozen in liquid nitrogen. Cell lysis was performed by thawing and resuspending the pellets in 800 μL 0.2 M NaOH, followed by 20 min incubation on ice and subsequent centrifugation at 11,200xg for 1 min at 4 °C. The supernatant was removed and pellets were resuspended in 50 μL HU buffer (8 M Urea, 5% SDS, 1 mM EDTA, 100 mM DTT, 200 mM Tris pH 6.8, protease inhibitor, bromophenol blue), heated at 70 °C for 10 min and then centrifuged again for 5 min at 11,200xg and at 4 °C. The substrates and the control protein DHFR were visualized by immunoblotting with, respectively, anti-FLAG or anti-HA primary and DyLight fluorophore conjugated secondary antibodies, and imaged using a Typhoon scanner (GE Healthcare). Quantification was done using the ImageStudioLite software (LI-COR). For the final graphs, the substrate signal was first normalized relative to the DHFR signal and then to the time point zero (before glucose replenishment). Three biological replicates were performed for all the assays.

A similar experiment was done to test is the novel high-affinity yGid4-binding sequences can confer glucose-induced instability onto Fbp1. To enable N-terminal exposure of sequences with N-terminal bulky hydrophobic residues, all Fbp1 versions (FDITGFSW-Fbp1(Δ1-9)-3xFLAG, LDVSWFEW-Fbp1(Δ1-9)-3xFLAG, a positive control IGLW-Fbp1 (Δ1-5)-3xFLAG[39] and Fbp1-3xFLAG) were expressed as N-terminal fusions to ubiquitin as described previously.[39,49] The cleavage of the ubiquitin fusion was confirmed by immunoblotting with anti-FLAG antibodies. The experiment was performed as described above.

X-ray crystallography

All crystallization trials were carried out in the MPIB Crystallization facility. All crystals were obtained by vapor diffusion experiment in sitting drops at room temperature. The diffraction datasets were recorded at X10SA beam line, Swiss Light Source (SLS) in Villingen, Switzerland.

Crystals of hGid4 (Δ1-99) (without a peptide) were obtained at a concentration of 10 mg/ml using 18% PEG 3350, 0.2 M ammonium nitrate and 0.1 M Bis-Tris buffer at pH 7. Crystals were cryoprotected in 20% ethylene glycol and flash-frozen in liquid nitrogen for data collection.

For hGid4 (Δ1-120, Δ294-300) crystals containing FDVSWFM peptide, 9.2 mg/mL of hGid4 was mixed with 600 μM FDVSWFMG peptide and incubated for 1 h on ice before setting up trays. Crystals were obtained using 1.1 M Sodium malonate, 0.3% Jeffamine ED-2001 pH 7 and 0.1 M HEPES pH 7 and cryoprotected using mix of 20% glycerol and 20% ethylene glycol.

Similarly, for yGid10 (Δ1-64, Δ285-292) crystals with the peptide FWLPANLW, the protein was concentrated to 10 mg/mL and mixed with the peptide to obtain final protein and peptide concentrations of 262 μM and 760 μM, respectively (~3-fold molar excess of the peptide). Crystals were obtained using 0.1 M MES pH 6.9 and cryoprotected using 20% ethylene glycol.

All the diffraction data were indexed, integrated, and scaled using XDS package. Phasing was performed through molecular replacement using the previous structure of hGid4 (PDB ID: **6CDC**, in the case of hGid4 with and without a peptide) or cryo EM structure of yGid4 (extracted from PDB ID: **7NS3**, in the case of peptide-bound yGid10) using PHASER module integrated into PHENIX software suite.[95–97] Model building was done using Coot,[93,94] and further refinements were carried out with phenix.refine. Details of X-ray diffraction data collection and refinement statistics are listed in Table S1.

Data availability

The accession codes for the PDB models are available in RCSB as follows: human Gid4 bound to a Gly/N-peptide, PDB ID: **7Q4Y**; human Gid4 bound to a Phe/N-peptide, PDB ID: **7Q50**; yeast Gid10 bound to a Phe/N-peptide, PDB ID: **7Q51**.

All the unprocessed image data have been deposited to Mendeley Data: http://dx.https://doi.org/10.17632/nz5mch8k2w.1.

CRediT authorship contribution statement

Jakub Chrustowicz: Conceptualization, Methodology, Investigation, Resources. **Dawafuti Sherpa:** Conceptualization, Methodology, Investigation, Resources. **Joan Teyra:** Methodology, Investigation, Resources. **Mun Siong Loke:** Investigation, Resources. **Grzegorz M. Popowicz:** Methodology, Investigation. **Jerome Basquin:** Methodology, Investigation. **Michael Sattler:** Methodology, Supervision, Funding acquisition. **J. Rajan Prabu:** Methodology. **Sachdev S. Sidhu:** Conceptualization, Methodology, Investigation, Supervision, Funding acquisition. **Brenda A. Schulman:** Conceptualization, Methodology, Supervision, Funding acquisition.

Acknowledgments

We thank G. Chen and A. Pavlenco for construction of N-terminal peptide phage-displayed

library; A. Varshavsky for promoter reference plasmids; S. Uebel and S. Pettera for peptide synthesis; K. Valer-Saldana and S. Pleyer for assistance with protein crystallization; J. Rech for the preparation of peptide spot arrays; Paul Scherrer Institut, Villigen, Switzerland for provision of synchrotron radiation beamtime at beamlines PXII and X10SA of the SLS; G. Kleiger for guidance regarding kinetics; I. Paron for technical assistance with mass spectrometry; O. Karayel and T. Vu for bioinformatic analysis of hGid4 interactors; S.v. Gronau for maintenance of insect cells and the Schulman lab for advice and support.

The project was funded by the Deutsche Forschungsgemeinschaft (DFG) SFB1035 (B.A.S. and M.S.), and Leibniz Prize SCHU 3196/1 (B.A.S.). Work in the Schulman lab is supported by the Max Planck Society.

Declaration of Competing Interest

B.A.S. is an honorary professor at Technical University of Munich, Germany and adjunct faculty at St. Jude Children's Research Hospital, Memphis, TN, USA, is on the scientific advisory boards of Interline Therapeutics and BioTheryX, and is co-inventor of intellectual property related to DCN1 small molecule inhibitors licensed to Cinsano.

Appendix A. Supplementary data

Supplementary data to this article can be found online at https://doi.org/10.1016/j.jmb.2021.167347.

Received 31 August 2021;
Accepted 2 November 2021;
Available online 9 November 2021

Keywords:
N-degron pathway;
Phage display;
Ubiquitin;
Protein–protein interaction;
Structural biology

† These authors contributed equally.

References

1. Varshavsky, A., (2019). N-degron and C-degron pathways of protein degradation. *Proc. Natl. Acad. Sci. USA* **116**, 358–366.
2. Bachmair, A., Varshavsky, A., (1989). The degradation signal in a short-lived protein. *Cell* **56**, 1019–1032.
3. Bachmair, A., Finley, D., Varshavsky, A., (1986). In vivo half-life of a protein is a function of its amino-terminal residue. *Science* **234**, 179–186.
4. Tasaki, T., Mulder, L.C., Iwamatsu, A., Lee, M.J., Davydov, I.V., Varshavsky, A., et al., (2005). A family of mammalian E3 ubiquitin ligases that contain the UBR box motif and recognize N-degrons. *Mol. Cell Biol.* **25**, 7120–7136.
5. Tasaki, T., Kwon, Y.T., (2007). The mammalian N-end rule pathway: new insights into its components and physiological roles. *Trends Biochem Sci.* **32**, 520–528.
6. Chen, S.J., Wu, X., Wadas, B., Oh, J.H., Varshavsky, A., (2017). An N-end rule pathway that recognizes proline and destroys gluconeogenic enzymes. *Science* **355**
7. Hammerle, M., Bauer, J., Rose, M., Szallies, A., Thumm, M., Dusterhus, S., et al., (1998). Proteins of newly isolated mutants and the amino-terminal proline are essential for ubiquitin-proteasome-catalyzed catabolite degradation of fructose-1,6-bisphosphatase of Saccharomyces cerevisiae. *J. Biol. Chem.* **273**, 25000–25005.
8. Timms, R.T., Zhang, Z., Rhee, D.Y., Harper, J.W., Koren, I., Elledge, S.J., (2019). A glycine-specific N-degron pathway mediates the quality control of protein N-myristoylation. *Science* **365**
9. Varshavsky, A., (2011). The N-end rule pathway and regulation by proteolysis. *Protein Sci.* **20**, 1298–1345.
10. Dong, C., Zhang, H., Li, L., Tempel, W., Loppnau, P., Min, J., (2018). Molecular basis of GID4-mediated recognition of degrons for the Pro/N-end rule pathway. *Nature Chem. Biol.* **14**, 466–473.
11. Yan, X., Li, Y., Wang, G., Zhou, Z., Song, G., Feng, Q., et al., (2021). Molecular basis for recognition of Gly/N-degrons by CRL2(ZYG11B) and CRL2(ZER1). *Mol. Cell.*
12. Driessen, H.P., de Jong, W.W., Tesser, G.I., Bloemendal, H., (1985). The mechanism of N-terminal acetylation of proteins. *CRC Crit. Rev. Biochem.* **18**, 281–325.
13. Hwang, C.S., Shemorry, A., Varshavsky, A., (2010). N-terminal acetylation of cellular proteins creates specific degradation signals. *Science* **327**, 973–977.
14. Polevoda, B., Arnesen, T., Sherman, F., (2009). A synopsis of eukaryotic Nalpha-terminal acetyltransferases: nomenclature, subunits and substrates. *BMC Proc.* **3** (Suppl 6), S2.
15. Shemorry, A., Hwang, C.S., Varshavsky, A., (2013). Control of protein quality and stoichiometries by N-terminal acetylation and the N-end rule pathway. *Mol. Cell* **50**, 540–551.
16. Wolf, D.H., (2004). From lysosome to proteasome: the power of yeast in the dissection of proteinase function in cellular regulation and waste disposal. *Cell Mol. Life Sci.* **61**, 1601–1614.
17. Santt, O., Pfirrmann, T., Braun, B., Juretschke, J., Kimmig, P., Scheel, H., et al., (2008). The yeast GID complex, a novel ubiquitin ligase (E3) involved in the regulation of carbohydrate metabolism. *Mol. Biol. Cell.* **19**, 3323–3333.
18. Braun, B., Pfirrmann, T., Menssen, R., Hofmann, K., Scheel, H., Wolf, D.H., (2011). Gid9, a second RING finger protein contributes to the ubiquitin ligase activity of the Gid complex required for catabolite degradation. *FEBS Letters* **585**, 3856–3861.
19. Menssen, R., Schweiggert, J., Schreiner, J., Kusevic, D., Reuther, J., Braun, B., et al., (2012). Exploring the topology of the Gid complex, the E3 ubiquitin ligase involved in catabolite-induced degradation of gluconeogenic enzymes. *J. Biol. Chem.* **287**, 25602–25614.
20. Regelmann, J., Schule, T., Josupeit, F.S., Horak, J., Rose, M., Entian, K.D., et al., (2003). Catabolite degradation of fructose-1,6-bisphosphatase in the yeast Saccharomyces cerevisiae: a genome-wide screen identifies eight novel GID genes and indicates the existence of two degradation pathways. *Mol. Biol. Cell.* **14**, 1652–1663.

21. Kobayashi, N., Yang, J., Ueda, A., Suzuki, T., Tomaru, K., Takeno, M., et al., (2007). RanBPM, Muskelin, p48EMLP, p44CTLH, and the armadillo-repeat proteins ARMC8alpha and ARMC8beta are components of the CTLH complex. *Gene* **396**, 236–247.
22. Boldt, K., van Reeuwijk, J., Lu, Q., Koutroumpas, K., Nguyen, T.M., Texier, Y., et al., (2016). An organelle-specific protein landscape identifies novel diseases and molecular mechanisms. *Nature Commun.* **7**, 11491.
23. Cao, W.X., Kabelitz, S., Gupta, M., Yeung, E., Lin, S., Rammelt, C., et al., (2020). Precise Temporal Regulation of Post-transcriptional Repressors Is Required for an Orderly Drosophila Maternal-to-Zygotic Transition. *Cell Rep.* **31**, 107783
24. Lampert, F., Stafa, D., Goga, A., Soste, M.V., Gilberto, S., Olieric, N., et al., (2018). The multi-subunit GID/CTLH E3 ubiquitin ligase promotes cell proliferation and targets the transcription factor Hbp1 for degradation. *Elife* **7**
25. Liu, H., Ding, J., Kohnlein, K., Urban, N., Ori, A., Villavicencio-Lorini, P., et al., (2020). The GID ubiquitin ligase complex is a regulator of AMPK activity and organismal lifespan. *Autophagy* **16**, 1618–1634.
26. Liu, H., Pfirrmann, T., (2019). The Gid-complex: an emerging player in the ubiquitin ligase league. *Biol. Chem.* **400**, 1429–1441.
27. Zavortink, M., Rutt, L.N., Dzitoyeva, S., Henriksen, J.C., Barrington, C., Bilodeau, D.Y., et al., (2020). The E2 Marie Kondo and the CTLH E3 ligase clear deposited RNA binding proteins during the maternal-to-zygotic transition. *Elife* **9**
28. Soni, S., Bala, S., Gwynn, B., Sahr, K.E., Peters, L.L., Hanspal, M., (2006). Absence of erythroblast macrophage protein (Emp) leads to failure of erythroblast nuclear extrusion. *J. Biol. Chem.* **281**, 20181–20189.
29. Zhen, R., Moo, C., Zhao, Z., Chen, M., Feng, H., Zheng, X., et al., (2020). Wdr26 regulates nuclear condensation in developing erythroblasts. *Blood* **135**, 208–219.
30. Pfirrmann, T., Villavicencio-Lorini, P., Subudhi, A.K., Menssen, R., Wolf, D.H., Hollemann, T., (2015). RMND5 from Xenopus laevis is an E3 ubiquitin-ligase and functions in early embryonic forebrain development. *PLoS One* **10**, e0120342
31. Maitland, M.E.R., Kuljanin, M., Wang, X., Lajoie, G.A., Schild-Poulter, C., (2021). Proteomic analysis of ubiquitination substrates reveals a CTLH E3 ligase complex-dependent regulation of glycolysis. *FASEB J.* **35**, e21825
32. Yuan, S., Zhu, H., Gou, H., Fu, W., Liu, L., Chen, T., et al., (2012). A ubiquitin ligase of symbiosis receptor kinase involved in nodule organogenesis. *Plant Physiol.* **160**, 106–117.
33. Menssen, R., Bui, K., Wolf, D.H., (2018). Regulation of the Gid ubiquitin ligase recognition subunit Gid4. *FEBS Letters* **592**, 3286–3294.
34. Qiao, S., Langlois, C.R., Chrustowicz, J., Sherpa, D., Karayel, O., Hansen, F.M., et al., (2020). Interconversion between Anticipatory and Active GID E3 Ubiquitin Ligase Conformations via Metabolically Driven Substrate Receptor Assembly. *Mol. Cell* **77** 150–63 e9.
35. Melnykov, A., Chen, S.J., Varshavsky, A., (2019). Gid10 as an alternative N-recognin of the Pro/N-degron pathway. *Proc. Natl. Acad. Sci. USA* **116**, 15914–15923.
36. Langlois CR, Beier V, Karayel O, Chrustowicz J, Sherpa D, Mann M, et al. A GID E3 ligase assembly ubiquitinates an Rsp5 E3 adaptor and regulates plasma membrane transporters. bioRxiv [Preprint]..
37. Kong, K.E., Fischer, B., Meurer, M., Kats, I., Li, Z., Ruhle, F., et al., (2021). Timer-based proteomic profiling of the ubiquitin-proteasome system reveals a substrate receptor of the GID ubiquitin ligase. *Mol. Cell* **81** 2460–76 e11.
38. Sherpa, D., Chrustowicz, J., Qiao, S., Langlois, C.R., Hehl, L.A., Gottemukkala, K.V., et al., (2021). GID E3 ligase supramolecular chelate assembly configures multipronged ubiquitin targeting of an oligomeric metabolic enzyme. *Mol. Cell* **81** 2445–59 e13.
39. Dong, C., Chen, S.J., Melnykov, A., Weirich, S., Sun, K., Jeltsch, A., et al., (2020). Recognition of nonproline N-terminal residues by the Pro/N-degron pathway. *Proc. Natl. Acad. Sci. USA* **117**, 14158–14167.
40. Peters, E.A., Schatz, P.J., Johnson, S.S., Dower, W.J., (1994). Membrane insertion defects caused by positive charges in the early mature region of protein pIII of filamentous phage fd can be corrected by prlA suppressors. *J. Bacteriol.* **176**, 4296–4305.
41. Rodi, D.J., Soares, A.S., Makowski, L., (2002). Quantitative assessment of peptide sequence diversity in M13 combinatorial peptide phage display libraries. *J. Mol. Biol.* **322**, 1039–1052.
42. Nilsson, I., von Heijne, G., (1992). A signal peptide with a proline next to the cleavage site inhibits leader peptidase when present in a sec-independent protein. *FEBS Letters* **299**, 243–246.
43. Pluckthun, A., Knowles, J.R., (1987). The consequences of stepwise deletions from the signal-processing site of beta-lactamase. *J. Biol. Chem.* **262**, 3951–3957.
44. Tonikian, R., Zhang, Y., Boone, C., Sidhu, S.S., (2007). Identifying specificity profiles for peptide recognition modules from phage-displayed peptide libraries. *Nature Protoc.* **2**, 1368–1386.
45. Shin, J.S., Park, S.H., Kim, L., Heo, J., Song, H.K., (2021). Crystal structure of yeast Gid10 in complex with Pro/N-degron. *Biochem. Biophys. Res. Commun.* **582**, 86–92.
46. Oh, J.H., Chen, S.J., Varshavsky, A., (2017). A reference-based protein degradation assay without global translation inhibitors. *J. Biol. Chem.* **292**, 21457–21465.
47. Sherman, F., Stewart, J.W., Tsunasawa, S., (1985). Methionine or not methionine at the beginning of a protein. *Bioessays* **3**, 27–31.
48. Aksnes, H., Drazic, A., Marie, M., Arnesen, T., (2016). First Things First: Vital Protein Marks by N-Terminal Acetyltransferases. *Trends Biochem. Sci.* **41**, 746–760.
49. Varshavsky, A., (2005). Ubiquitin fusion technique and related methods. *Methods Enzymol.* **399**, 777–799.
50. Barbin, L., Eisele, F., Santt, O., Wolf, D.H., (2010). The Cdc48-Ufd1-Npl4 complex is central in ubiquitin-proteasome triggered catabolite degradation of fructose-1,6-bisphosphatase. *Biochem. Biophys. Res. Commun.* **394**, 335–341.
51. Choi, W.S., Jeong, B.C., Joo, Y.J., Lee, M.R., Kim, J., Eck, M.J., et al., (2010). Structural basis for the recognition of N-end rule substrates by the UBR box of ubiquitin ligases. *Nature Struct. Mol. Biol.* **17**, 1175–1181.
52. Kim, L., Heo, J., Kwon, D.H., Shin, J.S., Jang, S.H., Park, Z.Y., et al., (2021). Structural basis for the N-degron specificity of ClpS1 from Arabidopsis thaliana. *Protein Sci.* **30**, 700–708.
53. Matta-Camacho, E., Kozlov, G., Li, F.F., Gehring, K., (2010). Structural basis of substrate recognition and

specificity in the N-end rule pathway. *Nature Struct. Mol. Biol.* **17**, 1182–1187.
54. Pan, M., Zheng. Q., Wang. T., Liang, L., Mao, J., Zuo, C., et al. (2021). Structural Insights Into the Initiation and Elongation of Ubiquitination by Ubr1. BioRxiv [Preprint]..
55. Roman-Hernandez, G., Grant, R.A., Sauer, R.T., Baker, T. A., (2009). Molecular basis of substrate selection by the N-end rule adaptor protein ClpS. *Proc. Natl. Acad. Sci. USA* **106**, 8888–8893.
56. Schuenemann, V.J., Kralik, S.M., Albrecht, R., Spall, S.K., Truscott, K.N., Dougan, D.A., et al., (2009). Structural basis of N-end rule substrate recognition in Escherichia coli by the ClpAP adaptor protein ClpS. *EMBO Rep.* **10**, 508–514.
57. Wang, K.H., Roman-Hernandez, G., Grant, R.A., Sauer, R.T., Baker, T.A., (2008). The molecular basis of N-end rule recognition. *Mol. Cell* **32**, 406–414.
58. Li, Y., Jin, K., Bunker, E., Zhang, X., Luo, X., Liu, X., et al., (2018). Structural basis of the phosphorylation-independent recognition of cyclin D1 by the SCF (FBXO31) ubiquitin ligase. *Proc. Natl. Acad. Sci. USA* **115**, 319–324.
59. Rusnac, D.V., Lin, H.C., Canzani, D., Tien, K.X., Hinds, T. R., Tsue, A.F., et al., (2018). Recognition of the Diglycine C-End Degron by CRL2(KLHDC2) Ubiquitin Ligase. *Mol. Cell.* **72** 813–22 e4.
60. Chen, X., Liao, S., Makaros, Y., Guo, Q., Zhu, Z., Krizelman, R., et al., (2021). Molecular basis for arginine C-terminal degron recognition by Cul2(FEM1) E3 ligase. *Nature Chem. Biol.* **17**, 254–262.
61. Zhao, S., Ru, W., Chen, X., Liao, S., Zhu, Z., Zhang, J., et al., (2021). Structural insights into SMCR8 C-degron recognition by FEM1B. *Biochem. Biophys. Res. Commun.* **557**, 236–239.
62. Sriram, S.M., Kwon, Y.T., (2010). The molecular principles of N-end rule recognition. *Nature Struct. Mol. Biol.* **17**, 1164–1165.
63. Tasaki, T., Zakrzewska, A., Dudgeon, D.D., Jiang, Y., Lazo, J.S., Kwon, Y.T., (2009). The substrate recognition domains of the N-end rule pathway. *J. Biol. Chem.* **284**, 1884–1895.
64. Tasaki, T., Sriram, S.M., Park, K.S., Kwon, Y.T., (2012). The N-end rule pathway. *Annu. Rev. Biochem.* **81**, 261–289.
65. Manford, A.G., Rodriguez-Perez, F., Shih, K.Y., Shi, Z., Berdan, C.A., Choe, M., et al., (2020). A cellular mechanism to detect and alleviate reductive stress. *Cell* **183** 46–61 e21.
66. Piatkov, K.I., Colnaghi, L., Bekes, M., Varshavsky, A., Huang, T.T., (2012). The auto-generated fragment of the Usp1 deubiquitylase is a physiological substrate of the N-end rule pathway. *Mol. Cell* **48**, 926–933.
67. Rao, H., Uhlmann, F., Nasmyth, K., Varshavsky, A., (2001). Degradation of a cohesin subunit by the N-end rule pathway is essential for chromosome stability. *Nature* **410**, 955–959.
68. Ditzel, M., Wilson, R., Tenev, T., Zachariou, A., Paul, A., Deas, E., et al., (2003). Degradation of DIAP1 by the N-end rule pathway is essential for regulating apoptosis. *Nature Cell Biol.* **5**, 467–473.
69. Piatkov, K.I., Oh, J.H., Liu, Y., Varshavsky, A., (2014). Calpain-generated natural protein fragments as short-lived substrates of the N-end rule pathway. *Proc. Natl. Acad. Sci. USA* **111**, E817–E826.
70. Jin, S.M., Lazarou, M., Wang, C., Kane, L.A., Narendra, D. P., Youle, R.J., (2010). Mitochondrial membrane potential regulates PINK1 import and proteolytic destabilization by PARL. *J. Cell Biol.* **191**, 933–942.
71. Yamano, K., Youle, R.J., (2013). PINK1 is degraded through the N-end rule pathway. *Autophagy* **9**, 1758–1769.
72. Chen, S.J., Kim, L., Song, H.K., Varshavsky, A., (2021). Aminopeptidases trim Xaa-Pro proteins, initiating their degradation by the Pro/N-degron pathway. *Proc. Natl. Acad. Sci. USA* **118**
73. Oughtred, R., Rust, J., Chang, C., Breitkreutz, B.J., Stark, C., Willems, A., et al., (2021). The BioGRID database: A comprehensive biomedical resource of curated protein, genetic, and chemical interactions. *Protein Sci.* **30**, 187–200.
74. Gonda, D.K., Bachmair, A., Wunning, I., Tobias, J.W., Lane, W.S., Varshavsky, A., (1989). Universality and structure of the N-end rule. *J. Biol. Chem.* **264**, 16700–16712.
75. Tobias, J.W., Shrader, T.E., Rocap, G., Varshavsky, A., (1991). The N-end rule in bacteria. *Science* **254**, 1374–1377.
76. Dougan, D.A., Truscott, K.N., Zeth, K., (2010). The bacterial N-end rule pathway: expect the unexpected. *Mol. Microbiol.* **76**, 545–558.
77. Szoradi, T., Schaeff, K., Garcia-Rivera, E.M., Itzhak, D.N., Schmidt, R.M., Bircham, P.W., et al., (2018). SHRED Is a Regulatory Cascade that Reprograms Ubr1 Substrate Specificity for Enhanced Protein Quality Control during Stress. *Mol. Cell.* **70** 1025–37 e5.
78. Botham, A., Coyaud, E., Nirmalanandhan, V.S., Gronda, M., Hurren, R., Maclean, N., et al., (2019). Global Interactome Mapping of Mitochondrial Intermembrane Space Proteases Identifies a Novel Function for HTRA2. *Proteomics* **19**, e1900139
79. Huttlin, E.L., Ting, L., Bruckner, R.J., Gebreab, F., Gygi, M.P., Szpyt, J., et al., (2015). The BioPlex Network: A Systematic Exploration of the Human Interactome. *Cell* **162**, 425–440.
80. Huttlin, E.L., Bruckner, R.J., Paulo, J.A., Cannon, J.R., Ting, L., Baltier, K., et al., (2017). Architecture of the human interactome defines protein communities and disease networks. *Nature* **545**, 505–509.
81. Clausen, T., Kaiser, M., Huber, R., Ehrmann, M., (2011). HTRA proteases: regulated proteolysis in protein quality control. *Nature Rev. Mol. Cell Biol.* **12**, 152–162.
82. Vande Walle, L., Lamkanfi, M., Vandenabeele, P., (2008). The mitochondrial serine protease HtrA2/Omi: an overview. *Cell Death Differ.* **15**, 453–460.
83. Davis, M., Hatzubai, A., Andersen, J.S., Ben-Shushan, E., Fisher, G.Z., Yaron, A., et al., (2002). Pseudosubstrate regulation of the SCF(beta-TrCP) ubiquitin ligase by hnRNP-U. *Genes Dev.* **16**, 439–451.
84. Welcker, M., Larimore, E.A., Frappier, L., Clurman, B.E., (2011). Nucleolar targeting of the fbw7 ubiquitin ligase by a pseudosubstrate and glycogen synthase kinase 3. *Mol. Cell Biol.* **31**, 1214–1224.
85. Cappell, S.D., Mark, K.G., Garbett, D., Pack, L.R., Rape, M., Meyer, T., (2018). EMI1 switches from being a substrate to an inhibitor of APC/C(CDH1) to start the cell cycle. *Nature* **558**, 313–317.
86. Manford, A.G., Mena, E.L., Shih, K.Y., Gee, C.L., McMinimy, R., Martinez-Gonzalez, B., et al., (2021).

Structural basis and regulation of the reductive stress response. *Cell* **184** 5375–90 e16.
87. Miller, J.J., Summers, M.K., Hansen, D.V., Nachury, M.V., Lehman, N.L., Loktev, A., et al., (2006). Emi1 stably binds and inhibits the anaphase-promoting complex/cyclosome as a pseudosubstrate inhibitor. *Genes Dev.* **20**, 2410–2420.
88. Mohamed, W.I., Park, S.L., Rabl, J., Leitner, A., Boehringer, D., Peter, M., (2021). The human GID complex engages two independent modules for substrate recruitment. *EMBO Rep.*.
89. Chen, I., Dorr, B.M., Liu, D.R., (2011). A general strategy for the evolution of bond-forming enzymes using yeast display. *Proc. Natl. Acad. Sci. USA* **108**, 11399–11404.
90. Kelley, L.A., Mezulis, S., Yates, C.M., Wass, M.N., Sternberg, M.J., (2015). The Phyre2 web portal for protein modeling, prediction and analysis. *Nat Protoc.* **10**, 845–858.
91. Pettersen, E.F., Goddard, T.D., Huang, C.C., Couch, G.S., Greenblatt, D.M., Meng, E.C., et al., (2004). UCSF Chimera–a visualization system for exploratory research and analysis. *J. Comput. Chem.* **25**, 1605–1612.
92. Goddard, T.D., Huang, C.C., Meng, E.C., Pettersen, E.F., Couch, G.S., Morris, J.H., et al., (2018). UCSF ChimeraX: Meeting modern challenges in visualization and analysis. *Protein Sci.* **27**, 14–25.
93. Emsley, P., Cowtan, K., (2004). Coot: model-building tools for molecular graphics. *Acta Crystallogr. D Biol. Crystallogr.* **60**, 2126–2132.
94. Emsley, P., Lohkamp, B., Scott, W.G., Cowtan, K., (2010). Features and development of Coot. *Acta Crystallogr. D Biol. Crystallogr.* **66**, 486–501.
95. Adams, P.D., Afonine, P.V., Bunkoczi, G., Chen, V.B., Davis, I.W., Echols, N., et al., (2010). PHENIX: a comprehensive Python-based system for macromolecular structure solution. *Acta Crystallogr. D Biol. Crystallogr.* **66**, 213–221.
96. Afonine, P.V., Klaholz, B.P., Moriarty, N.W., Poon, B.K., Sobolev, O.V., Terwilliger, T.C., et al., (2018). New tools for the analysis and validation of cryo-EM maps and atomic models. *Acta Crystallogr. D Struct. Biol.* **74**, 814–840.
97. DiMaio, F., Echols, N., Headd, J.J., Terwilliger, T.C., Adams, P.D., Baker, D., (2013). Improved low-resolution crystallographic refinement with Phenix and Rosetta. *Nature Methods* **10**, 1102–1104.
98. Schindelin, J., Arganda-Carreras, I., Frise, E., Kaynig, V., Longair, M., Pietzsch, T., et al., (2012). Fiji: an open-source platform for biological-image analysis. *Nature Methods* **9**, 676–682.
99. Gibson, D.G., Young, L., Chuang, R.Y., Venter, J.C., Hutchison 3rd, C.A., Smith, H.O., (2009). Enzymatic assembly of DNA molecules up to several hundred kilobases. *Nature Methods* **6**, 343–345.
100. Weissmann, F., Petzold, G., VanderLinden, R., Huis In't Veld, P.J., Brown, N.G., Lampert, F., et al., (2016). biGBac enables rapid gene assembly for the expression of large multisubunit protein complexes. *Proc. Natl. Acad. Sci. USA* **113**, E2564–9.
101. Lobanov, M.Y., Furletova, E.I., Bogatyreva, N.S., Roytberg, M.A., Galzitskaya, O.V., (2010). Library of disordered patterns in 3D protein structures. *PLoS Comput. Biol.* **6**, e1000958
102. Kaiser, S.E., Riley, B.E., Shaler, T.A., Trevino, R.S., Becker, C.H., Schulman, H., et al., (2011). Protein standard absolute quantification (PSAQ) method for the measurement of cellular ubiquitin pools. *Nature Methods* **8**, 691.
103. Chen, G., Gorelik, L., Simon, K.J., Pavlenco, A., Cheung, A., Brickelmaier, M., et al., (2015). Synthetic antibodies and peptides recognizing progressive multifocal leukoencephalopathy-specific point mutations in polyomavirus JC capsid viral protein 1. *MAbs* **7**, 681–692.
104. Deshayes, K., Schaffer, M.L., Skelton, N.J., Nakamura, G. R., Kadkhodayan, S., Sidhu, S.S., (2002). Rapid identification of small binding motifs with high-throughput phage display: discovery of peptidic antagonists of IGF-1 function. *Chem. Biol.* **9**, 495–505.

4. Discussion

The two publications included in my thesis disclose several aspects of substrate targeting by GID E3s – a family of evolutionarily conserved multi-subunit ubiquitin ligases, which regulate processes ranging from metabolism to cell division. Although the mechanistic role of GID in most of these processes is only beginning to emerge, a multitude of its physiological functions suggest a vast repertoire of targeted proteins. By combining cryoEM, X-ray crystallography, biochemistry, and yeast genetics, we have identified several principles enabling GID to target substrates harboring various N-degrons and adopting oligomeric states.

The identification of novel high-affinity Gid4- and yGid10-binding motifs that are strikingly different from previous motifs and natural degrons highlighted remarkable binding versatility of GID/CTLH substrate receptors. By comparing structures of Gid4 and yGid10 in complex with different peptides determined by us and other groups [68, 69, 109, 111, 112], we revealed that their ability to recognize diverse sequences is attributable to the plasticity of four hairpin loops at the entrance to their substrate-binding tunnels. While largely disordered in the apo form of both Gid4 homologs [62, 109], and possibly yGid10, these loops fold upon peptide binding in a conformation complementing peptide sequences. Reciprocally, the bound peptides themselves adopt different folds to maximize interactions with the substrate binding tunnels. Moreover, our study demonstrated the paramount importance of the sequence context – while the N-termini of peptides play a crucial role in anchoring them to the bottom of substrate binding tunnels, their downstream sequences reshape the flexible Gid4/yGid10 loops, thus dictating preference for an N-terminal residue. The characterized mechanism of N-degron recognition might apply to other end-degron E3s, such as the recently identified suite of C-degron substrate receptors [38], as it enables recognition of various extended terminal sequences with a wide range of affinities.

In addition to mechanistic insights, the novel sequence motifs may assist in identification of physiological GID substrates as well as proteins interacting with GID substrate receptors to modulate activity or localization of the complex, similar to those regulating other multi-subunit E3 ligases [113-117]. However, *in silico* prediction of potential GID substrates/interactors bearing the identified sequences is not straightforward as most of them initiate with bulky hydrophobic residues, which interfere with co-translational removal of Met present at N-termini of all newly-synthesized proteins [66]. Nonetheless, there are alternative routes to generate bulky N-termini post-translationally – proteolytic cleavage exposing internal protein sequences [118] and non-ribosomal conjugation of single amino acid residues at protein N-termini [119]. Both of them are responsible for creating a plethora of terminal degrons and it is tempting to

speculate that similar mechanisms might likewise generate the identified sequence motifs. Notably, aminopeptidases Icp55 and Fra1 have recently been shown to trim the N-termini of two yeast GID substrates to expose their Pro/N-degrons [67], demonstrating the importance of post-translational processing in the generation of GID substrates.

While degron recognition is essential for targeting of all E3 ligase substrates, it is insufficient to drive robust ubiquitylation and degradation of a rate-limiting gluconeogenic enzyme Fbp1. We discovered that Fbp1 targeting depends on the global transformation of GID architecture induced by an additional subunit Gid7. Remarkably, Gid7 brings two catalytically active GID^{SR4} cores together to form a gigantic 1.5 MDa oval complex referred to as Chelator-GID^{SR4}. Although regulation of E3 ligase activity through oligomerization of its catalytic or substrate recognition subunits has previously been observed [120], the supramolecular assembly of GID is unprecedented as it is remarkably specific for the quaternary structure of its substrate. Notably, the daisy chain-like arrangement of modules in Chelator-GID^{SR4} is tailored to complement the oligomeric nature of Fbp1 – the two yGid4 molecules are positioned opposite to each other, poised to capture two Fbp1 degrons, whereas the two catalytic modules simultaneously target its multiple protomers. The capacity for supramolecular assembly has not only been preserved but further diversified throughout the evolution. The human CTLH complex contains two Gid7 orthologs, WDR26 (associating with a small protein YPEL5 of an unknown function) and MKLN1, which mediate formation of distinct higher-order forms of the CTLH complex paralleling yeast Chelator-GID^{SR4}. Since their mutations elicit different disease phenotypes [121-124], the distinct human assemblies might be tailored to target different oligomeric substrates.

As inferred from the structural comparison of its apo and Fbp1-bound form, Chelator-GID^{SR4} is a dynamic assembly owing to flexible junctions between its modules. Much as GID substrate receptors fold their loops to bind diverse peptides, the substrate-binding modules of Chelator-GID^{SR4} tilt toward the center of the oval complex to match the spacing between Fbp1's degrons. A similar rearrangement of catalytic modules is likely crucial to juxtapose activated E2~Ub and the target lysine, especially during the synthesis of polyubiquitin chains wherein the distance between the donor and acceptor ubiquitin dynamically varies. We thus speculate that the pliability of Chelator-GID^{SR4} is essential to polyubiquitylate structurally diverse substrates.

The proposed chelator model enables multipronged ubiquitin targeting of Fbp1. First, Chelator-GID^{SR4} avidly binds Fbp1 thanks to the concerted capture of its two degrons. Since nature often exploits avidity to strikingly enhance the overall binding strength within multivalent complexes [125], it seems likely that the supramolecular assembly of GID evolved to compensate for suboptimal degrons. Second, encapsulation of Fbp1 increases the efficiency

of its targeting. The generated model implies that three Fbp1 protomers can be simultaneously ubiquitylated by the two opposing catalytic centers of Chelator-GID^{SR4}. Finally, Chelator-GID^{SR4} targets lysines located nearby functionally relevant sites of Fbp1. Although its impact on the metabolic function of Fbp1 awaits future studies, it is tempting to speculate that ubiquitylation of Fbp1 immediately incapacitates its several protomers upstream of their proteasomal degradation. Thus, the stringency of lysine selection exhibited by Chelator-GID^{SR4} might parallel other well-known E3 ligases, such as those catalyzing site-specific histone ubiquitylation in response to DNA damage [126].

Our studies of GID/CTLH E3s underscored the importance of complementarity between E3 ligase architecture, degron identity, and the constellation of ubiquitylation sites for efficient substrate targeting. A mismatch between these factors impedes or precludes substrate degradation – Mdh2 carrying a weaker Fbp1 degron is degraded more slowly, whereas Fbp1 is stabilized in the absence of GID supramolecular assembly, even when harboring a stronger degron of Mdh2. This concept is of utmost importance in the field of targeted protein degradation, wherein small molecules, called PROTACs, are engineered to induce proximity between an E3 ligase and a cellular protein of interest to promote its ubiquitin-dependent degradation [127]. However, PROTAC-induced recruitment of a cellular target is sometimes insufficient to confer its instability [128, 129], e.g. due to inaccessibility of substrate lysines to an employed E3 ligase or suboptimal positioning of ubiquitylation sites with respect to an unstructured substrate region important to initiate proteasomal proteolysis [130, 131].

To overcome this challenge, different E3s could be screened for optimal lysine selectivity profiles. However, the toolbox of E3s is limited as only 1% of all existing E3 ligases have been harnessed for PROTAC development [127]. Therefore, the mechanistic characterization of novel E3s can expand the potential of PROTAC technology. Our studies identified several features of the GID/CTLH E3 that hold promise for its therapeutic exploitation: (1) in collaboration with its cognate E2 Ube2H, it catalyzes synthesis of degradative K48-linked polyubiquitin chains, (2) its substrate receptor hGid4 features a deep substrate-binding tunnel that can remodel to accommodate various binders with high affinity, whereas its predominantly hydrophobic character might be favorable for the development of non-polar cell-permeable binders. Markedly, a small-molecule ligand PFI-7 binding hGid4 with a dissociation constant (K_D) of 80 nM has recently been developed. (3) It forms various higher-order assemblies that might target structurally diverse proteins and enhance their binding through avidity.

Taken together, the malleability of the GID/CTLH E3 ligases is central to their ability to target diverse substrates – conformations of substrate receptor fine-tune binding of various degron sequences, whereas the supramolecular assembly elaborates the catalytically active core

to match several features of substrate quaternary structure. These mechanistic principles offer a prospect for interesting regulation. Since the plasticity of Gid4 and Gid10 hairpin loops determine binding specificity, factors affecting their conformation could abrogate or modulate substrate binding. Similarly, the formation of supramolecular GID assemblies might be induced or inhibited by cellular factors, such as post-translational modifications of GID subunits.

By visualizing higher-order forms of both the yeast and human complexes, we have only scratched the surface of the actual complexity of GID. Notably, the human CTLH might exist in numerous flavors as many of its subunits have several isoforms or splicing versions and interact with a multitude of uncharacterized binding partners [70, 132-134]. Moreover, the recent studies suggested that substrate recognition by fly [76] and human CTLH [135] might be independent of the Gid4-Gid5 module, hence highlighting the existence of alternative modes of substrate recognition. Given the astonishing molecular logic of Fbp1 targeting by yeast Chelator-GID and the evolutionary conservation of the supramolecular GID E3 assembly, we expect that further exploration of the GID/CTLH family will uncover many elegant strategies of substrate targeting and provide exciting concepts to the ubiquitin field.

6. References

[1] Ciechanover A. Proteolysis: from the lysosome to ubiquitin and the proteasome. Nat Rev Mol Cell Biol. 2005;6:79-87.

[2] Schoenheimer R, Clarke HT. The dynamic state of body constituents. Cambridge, Mass.,: Harvard university press; 1942.

[3] De Duve C, Gianetto R, Appelmans F, Wattiaux R. Enzymic content of the mitochondria fraction. Nature. 1953;172:1143-4.

[4] Gianetto R, De Duve C. Tissue fractionation studies. 4. Comparative study of the binding of acid phosphatase, beta-glucuronidase and cathepsin by rat-liver particles. Biochem J. 1955;59:433-8.

[5] Ciechanover A, Elias S, Heller H, Hershko A. "Covalent affinity" purification of ubiquitin-activating enzyme. J Biol Chem. 1982;257:2537-42.

[6] Ciechanover A, Heller H, Elias S, Haas AL, Hershko A. ATP-dependent conjugation of reticulocyte proteins with the polypeptide required for protein degradation. Proc Natl Acad Sci U S A. 1980;77:1365-8.

[7] Ciehanover A, Hod Y, Hershko A. A heat-stable polypeptide component of an ATP-dependent proteolytic system from reticulocytes. Biochem Biophys Res Commun. 1978;81:1100-5.

[8] Hershko A, Heller H, Elias S, Ciechanover A. Components of ubiquitin-protein ligase system. Resolution, affinity purification, and role in protein breakdown. J Biol Chem. 1983;258:8206-14.

[9] Mabbitt PD, Loreto A, Dery MA, Fletcher AJ, Stanley M, Pao KC, et al. Structural basis for RING-Cys-Relay E3 ligase activity and its role in axon integrity. Nat Chem Biol. 2020;16:1227-36.

[10] Wilkinson KD, Urban MK, Haas AL. Ubiquitin is the ATP-dependent proteolysis factor I of rabbit reticulocytes. J Biol Chem. 1980;255:7529-32.

[11] Ciechanover A, Finley D, Varshavsky A. Ubiquitin dependence of selective protein degradation demonstrated in the mammalian cell cycle mutant ts85. Cell. 1984;37:57-66.

[12] Finley D, Ciechanover A, Varshavsky A. Thermolability of ubiquitin-activating enzyme from the mammalian cell cycle mutant ts85. Cell. 1984;37:43-55.

[13] Hough R, Pratt G, Rechsteiner M. Ubiquitin-lysozyme conjugates. Identification and characterization of an ATP-dependent protease from rabbit reticulocyte lysates. J Biol Chem. 1986;261:2400-8.

[14] Waxman L, Fagan JM, Goldberg AL. Demonstration of two distinct high molecular weight proteases in rabbit reticulocytes, one of which degrades ubiquitin conjugates. J Biol Chem. 1987;262:2451-7.

[15] Otten EG, Werner E, Crespillo-Casado A, Boyle KB, Dharamdasani V, Pathe C, et al. Ubiquitylation of lipopolysaccharide by RNF213 during bacterial infection. Nature. 2021;594:111-6.

[16] Kelsall IR, McCrory EH, Xu Y, Scudamore CL, Nanda SK, Mancebo-Gamella P, et al. HOIL-1-catalysed ubiquitylation of unbranched glucosaccharides and its activation by ubiquitin oligomers. BioRxiv (preprint). 2021.

[17] Mukhopadhyay D, Riezman H. Proteasome-independent functions of ubiquitin in endocytosis and signaling. Science. 2007;315:201-5.

[18] van der Veen AG, Ploegh HL. Ubiquitin-like proteins. Annu Rev Biochem. 2012;81:323-57.

[19] Komander D, Rape M. The ubiquitin code. Annu Rev Biochem. 2012;81:203-29.

[20] Vijay-Kumar S, Bugg CE, Wilkinson KD, Cook WJ. Three-dimensional structure of ubiquitin at 2.8 A resolution. Proc Natl Acad Sci U S A. 1985;82:3582-5.

[21] Husnjak K, Dikic I. Ubiquitin-binding proteins: decoders of ubiquitin-mediated cellular functions. Annu Rev Biochem. 2012;81:291-322.

[22] Oh E, Akopian D, Rape M. Principles of Ubiquitin-Dependent Signaling. Annu Rev Cell Dev Biol. 2018;34:137-62.

[23] Cappadocia L, Lima CD. Ubiquitin-like Protein Conjugation: Structures, Chemistry, and Mechanism. Chem Rev. 2018;118:889-918.

[24] McDowell GS, Philpott A. Non-canonical ubiquitylation: mechanisms and consequences. Int J Biochem Cell Biol. 2013;45:1833-42.

[25] Swatek KN, Komander D. Ubiquitin modifications. Cell Res. 2016;26:399-422.

[26] Herhaus L, Dikic I. Expanding the ubiquitin code through post-translational modification. Embo Reports. 2015;16:1071-83.

[27] Schulman BA, Harper JW. Ubiquitin-like protein activation by E1 enzymes: the apex for downstream signalling pathways. Nat Rev Mol Cell Bio. 2009;10:319-31.

[28] Stewart MD, Ritterhoff T, Klevit RE, Brzovic PS. E2 enzymes: more than just middle men. Cell Research. 2016;26:423-40.

[29] Li W, Bengtson MH, Ulbrich A, Matsuda A, Reddy VA, Orth A, et al. Genome-wide and functional annotation of human E3 ubiquitin ligases identifies MULAN, a mitochondrial E3 that regulates the organelle's dynamics and signaling. PLoS One. 2008;3:e1487.

[30] Buetow L, Huang DT. Structural insights into the catalysis and regulation of E3 ubiquitin ligases. Nat Rev Mol Cell Bio. 2016;17:626-42.

[31] Pao KC, Wood NT, Knebel A, Rafie K, Stanley M, Mabbitt PD, et al. Activity-based E3 ligase profiling uncovers an E3 ligase with esterification activity. Nature. 2018;556:381-5.

[32] Horn-Ghetko D, Krist DT, Prabu JR, Baek K, Mulder MPC, Klugel M, et al. Ubiquitin ligation to F-box protein targets by SCF-RBR E3-E3 super-assembly. Nature. 2021;590:671-6.

[33] Kostrhon S, Prabu JR, Baek K, Horn-Ghetko D, von Gronau S, Klugel M, et al. CUL5-ARIH2 E3-E3 ubiquitin ligase structure reveals cullin-specific NEDD8 activation. Nat Chem Biol. 2021.

[34] Eletr ZM, Huang DT, Duda DM, Schulman BA, Kuhlman B. E2 conjugating enzymes must disengage from their E1 enzymes before E3-dependent ubiquitin and ubiquitin-like transfer. Nat Struct Mol Biol. 2005;12:933-4.

[35] Metzger MB, Pruneda JN, Klevit RE, Weissman AM. RING-type E3 ligases: master manipulators of E2 ubiquitin-conjugating enzymes and ubiquitination. Biochim Biophys Acta. 2014;1843:47-60.

[36] Varshavsky A. Naming a targeting signal. Cell. 1991;64:13-5.

[37] Varshavsky A. The N-end rule: Functions, mysteries, uses. P Natl Acad Sci USA. 1996;93:12142-9.

[38] Timms RT, Koren I. Tying up loose ends: the N-degron and C-degron pathways of protein degradation. Biochem Soc Trans. 2020;48:1557-67.

[39] Bachmair A, Finley D, Varshavsky A. In vivo half-life of a protein is a function of its amino-terminal residue. Science. 1986;234:179-86.

[40] Dougan DA, Micevski D, Truscott KN. The N-end rule pathway: from recognition by N-recognins, to destruction by AAA+proteases. Biochim Biophys Acta. 2012;1823:83-91.

[41] Varshavsky A. N-degron and C-degron pathways of protein degradation. Proc Natl Acad Sci U S A. 2019;116:358-66.

[42] Varshavsky A. The N-end rule pathway and regulation by proteolysis. Protein Sci. 2011;20:1298-345.

[43] Hwang CS, Shemorry A, Varshavsky A. N-terminal acetylation of cellular proteins creates specific degradation signals. Science. 2010;327:973-7.

[44] Koren I, Timms RT, Kula T, Xu QK, Li MMZ, Elledge SJ. The Eukaryotic Proteome Is Shaped by E3 Ubiquitin Ligases Targeting C-Terminal Degrons. Cell. 2018;173:1622-+.

[45] Lin HC, Yeh CW, Chen YF, Lee TT, Hsieh PY, Rusnac DV, et al. C-Terminal End-Directed Protein Elimination by CRL2 Ubiquitin Ligases. Mol Cell. 2018;70:602-13 e3.

[46] Arnesen T, Van Damme P, Polevoda B, Helsens K, Evjenth R, Colaert N, et al. Proteomics analyses reveal the evolutionary conservation and divergence of N-terminal acetyltransferases from yeast and humans. Proc Natl Acad Sci U S A. 2009;106:8157-62.

[47] Aksnes H, Drazic A, Marie M, Arnesen T. First Things First: Vital Protein Marks by N-Terminal Acetyltransferases. Trends Biochem Sci. 2016;41:746-60.

[48] Cornish-Bowden A. Understanding allosteric and cooperative interactions in enzymes. FEBS J. 2014;281:621-32.

[49] Plaxton W. Principles of metabolic control. . In: Storey K, editor. Functional Metabolism: Regulation and Adaptation: John Wiley & Sons, Inc.; 2004. p. 1-24.

[50] Zaman S, Lippman SI, Zhao X, Broach JR. How Saccharomyces Responds to Nutrients. Annu Rev Genet. 2008;42:27-81.

[51] Johnston M, Kim JH. Glucose as a hormone: receptor-mediated glucose sensing in the yeast Saccharomyces cerevisiae. Biochem Soc T. 2005;33:247-52.

[52] Gancedo JM. Yeast carbon catabolite repression. Microbiol Mol Biol Rev. 1998;62:334-61.

[53] Wolf DH. From lysosome to proteasome: the power of yeast in the dissection of proteinase function in cellular regulation and waste disposal. Cell Mol Life Sci. 2004;61:1601-14.

[54] Hammerle M, Bauer J, Rose M, Szallies A, Thumm M, Dusterhus S, et al. Proteins of newly isolated mutants and the amino-terminal proline are essential for ubiquitin-proteasome-catalyzed catabolite degradation of fructose-1,6-bisphosphatase of Saccharomyces cerevisiae. J Biol Chem. 1998;273:25000-5.

[55] Regelmann J, Schule T, Josupeit FS, Horak J, Rose M, Entian KD, et al. Catabolite degradation of fructose-1,6-bisphosphatase in the yeast Saccharomyces cerevisiae: a genome-wide screen identifies eight novel GID genes and indicates the existence of two degradation pathways. Mol Biol Cell. 2003;14:1652-63.

[56] Santt O, Pfirrmann T, Braun B, Juretschke J, Kimmig P, Scheel H, et al. The yeast GID complex, a novel ubiquitin ligase (E3) involved in the regulation of carbohydrate metabolism. Mol Biol Cell. 2008;19:3323-33.

[57] Menssen R, Schweiggert J, Schreiner J, Kusevic D, Reuther J, Braun B, et al. Exploring the topology of the Gid complex, the E3 ubiquitin ligase involved in catabolite-induced degradation of gluconeogenic enzymes. J Biol Chem. 2012;287:25602-14.

[58] Schule T, Rose M, Entian KD, Thumm M, Wolf DH. Ubc8p functions in catabolite degradation of fructose-1, 6-bisphosphatase in yeast. EMBO J. 2000;19:2161-7.

[59] Amerik A, Swaminathan S, Krantz BA, Wilkinson KD, Hochstrasser M. In vivo disassembly of free polyubiquitin chains by yeast Ubp14 modulates rates of protein degradation by the proteasome. EMBO J. 1997;16:4826-38.

[60] Braun B, Pfirrmann T, Menssen R, Hofmann K, Scheel H, Wolf DH. Gid9, a second RING finger protein contributes to the ubiquitin ligase activity of the Gid complex required for catabolite degradation. FEBS Lett. 2011;585:3856-61.

[61] Chen SJ, Wu X, Wadas B, Oh JH, Varshavsky A. An N-end rule pathway that recognizes proline and destroys gluconeogenic enzymes. Science. 2017;355.

[62] Qiao S, Langlois CR, Chrustowicz J, Sherpa D, Karayel O, Hansen FM, et al. Interconversion between Anticipatory and Active GID E3 Ubiquitin Ligase Conformations via Metabolically Driven Substrate Receptor Assembly. Mol Cell. 2020;77:150-63 e9.

[63] Menssen R, Bui K, Wolf DH. Regulation of the Gid ubiquitin ligase recognition subunit Gid4. FEBS Lett. 2018;592:3286-94.

[64] Melnykov A, Chen SJ, Varshavsky A. Gid10 as an alternative N-recognin of the Pro/N-degron pathway. Proc Natl Acad Sci U S A. 2019;116:15914-23.

[65] Kong KE, Fischer B, Meurer M, Kats I, Li Z, Ruhle F, et al. Timer-based proteomic profiling of the ubiquitin-proteasome system reveals a substrate receptor of the GID ubiquitin ligase. Mol Cell. 2021;81:2460-76 e11.

[66] Xiao Q, Zhang F, Nacev BA, Liu JO, Pei D. Protein N-terminal processing: substrate specificity of Escherichia coli and human methionine aminopeptidases. Biochemistry. 2010;49:5588-99.

[67] Chen SJ, Kim L, Song HK, Varshavsky A. Aminopeptidases trim Xaa-Pro proteins, initiating their degradation by the Pro/N-degron pathway. Proc Natl Acad Sci U S A. 2021;118.

[68] Dong C, Zhang H, Li L, Tempel W, Loppnau P, Min J. Molecular basis of GID4-mediated recognition of degrons for the Pro/N-end rule pathway. Nat Chem Biol. 2018;14:466-73.

[69] Dong C, Chen SJ, Melnykov A, Weirich S, Sun K, Jeltsch A, et al. Recognition of nonproline N-terminal residues by the Pro/N-degron pathway. Proc Natl Acad Sci U S A. 2020;117:14158-67.

[70] Lampert F, Stafa D, Goga A, Soste MV, Gilberto S, Olieric N, et al. The multi-subunit GID/CTLH E3 ubiquitin ligase promotes cell proliferation and targets the transcription factor Hbp1 for degradation. Elife. 2018;7.

[71] Francis O, Han F, Adams JC. Molecular phylogeny of a RING E3 ubiquitin ligase, conserved in eukaryotic cells and dominated by homologous components, the muskelin/RanBPM/CTLH complex. PLoS One. 2013;8:e75217.

[72] Umeda M, Nishitani H, Nishimoto T. A novel nuclear protein, Twa1, and Muskelin comprise a complex with RanBPM. Gene. 2003;303:47-54.

[73] Kobayashi N, Yang J, Ueda A, Suzuki T, Tomaru K, Takeno M, et al. RanBPM, Muskelin, p48EMLP, p44CTLH, and the armadillo-repeat proteins ARMC8alpha and ARMC8beta are components of the CTLH complex. Gene. 2007;396:236-47.

[74] Yuan S, Zhu H, Gou H, Fu W, Liu L, Chen T, et al. A ubiquitin ligase of symbiosis receptor kinase involved in nodule organogenesis. Plant Physiol. 2012;160:106-17.

[75] Cao WX, Kabelitz S, Gupta M, Yeung E, Lin S, Rammelt C, et al. Precise Temporal Regulation of Post-transcriptional Repressors Is Required for an Orderly Drosophila Maternal-to-Zygotic Transition. Cell Rep. 2020;31:107783.

[76] Zavortink M, Rutt LN, Dzitoyeva S, Henriksen JC, Barrington C, Bilodeau DY, et al. The E2 Marie Kondo and the CTLH E3 ligase clear deposited RNA binding proteins during the maternal-to-zygotic transition. Elife. 2020;9.

[77] Pfirrmann T, Villavicencio-Lorini P, Subudhi AK, Menssen R, Wolf DH, Hollemann T. RMND5 from Xenopus laevis is an E3 ubiquitin-ligase and functions in early embryonic forebrain development. PLoS One. 2015;10:e0120342.

[78] Soni S, Bala S, Gwynn B, Sahr KE, Peters LL, Hanspal M. Absence of erythroblast macrophage protein (Emp) leads to failure of erythroblast nuclear extrusion. J Biol Chem. 2006;281:20181-9.

[79] Zhen R, Moo C, Zhao Z, Chen M, Feng H, Zheng X, et al. Wdr26 regulates nuclear condensation in developing erythroblasts. Blood. 2020;135:208-19.

[80] Leal-Esteban LC, Rothe B, Fortier S, Isenschmid M, Constam DB. Role of Bicaudal C1 in renal gluconeogenesis and its novel interaction with the CTLH complex. PLoS Genet. 2018;14:e1007487.

[81] Maitland MER, Kuljanin M, Wang X, Lajoie GA, Schild-Poulter C. Proteomic analysis of ubiquitination substrates reveals a CTLH E3 ligase complex-dependent regulation of glycolysis. FASEB J. 2021;35:e21825.

[82] Liu H, Ding J, Kohnlein K, Urban N, Ori A, Villavicencio-Lorini P, et al. The GID ubiquitin ligase complex is a regulator of AMPK activity and organismal lifespan. Autophagy. 2020;16:1618-34.

[83] McTavish CJ, Berube-Janzen W, Wang X, Maitland MER, Salemi LM, Hess DA, et al. Regulation of c-Raf Stability through the CTLH Complex. Int J Mol Sci. 2019;20.

[84] Salemi LM, Maitland MER, Yefet ER, Schild-Poulter C. Inhibition of HDAC6 activity through interaction with RanBPM and its associated CTLH complex. BMC Cancer. 2017;17:460.

[85] Huffman N, Palmieri D, Coppola V. The CTLH Complex in Cancer Cell Plasticity. J Oncol. 2019;2019:4216750.

[86] Gibson DG, Young L, Chuang RY, Venter JC, Hutchison CA, 3rd, Smith HO. Enzymatic assembly of DNA molecules up to several hundred kilobases. Nat Methods. 2009;6:343-5.

[87] Weissmann F, Petzold G, VanderLinden R, Huis In 't Veld PJ, Brown NG, Lampert F, et al. biGBac enables rapid gene assembly for the expression of large multisubunit protein complexes. Proc Natl Acad Sci U S A. 2016;113:E2564-9.

[88] Lobanov MY, Furletova EI, Bogatyreva NS, Roytberg MA, Galzitskaya OV. Library of disordered patterns in 3D protein structures. PLoS Comput Biol. 2010;6:e1000958.

[89] Kaiser SE, Riley BE, Shaler TA, Trevino RS, Becker CH, Schulman H, et al. Protein standard absolute quantification (PSAQ) method for the measurement of cellular ubiquitin pools. Nature Methods. 2011;8:691.

[90] Chen I, Dorr BM, Liu DR. A general strategy for the evolution of bond-forming enzymes using yeast display. Proc Natl Acad Sci U S A. 2011;108:11399-404.

[91] Mastronarde DN. SerialEM: A Program for Automated Tilt Series Acquisition on Tecnai Microscopes Using Prediction of Specimen Position. Microscopy and Microanalysis. 2003;9:1182-3.

[92] Biyani N, Righetto RD, McLeod R, Caujolle-Bert D, Castano-Diez D, Goldie KN, et al. Focus: The interface between data collection and data processing in cryo-EM. J Struct Biol. 2017;198:124-33.

[93] Fernandez-Leiro R, Scheres SHW. A pipeline approach to single-particle processing in RELION. Acta Crystallogr D Struct Biol. 2017;73:496-502.

[94] Scheres SH. RELION: implementation of a Bayesian approach to cryo-EM structure determination. J Struct Biol. 2012;180:519-30.

[95] Zivanov J, Nakane T, Forsberg BO, Kimanius D, Hagen WJ, Lindahl E, et al. New tools for automated high-resolution cryo-EM structure determination in RELION-3. Elife. 2018;7.

[96] Zheng SQ, Palovcak E, Armache JP, Verba KA, Cheng Y, Agard DA. MotionCor2: anisotropic correction of beam-induced motion for improved cryo-electron microscopy. Nat Methods. 2017;14:331-2.

[97] Zhang K. Gctf: Real-time CTF determination and correction. J Struct Biol. 2016;193:1-12.

[98] Sanchez-Garcia R, Gomez-Blanco J, Cuervo A, Carazo JM, Sorzano COS, Vargas J. DeepEMhancer: a deep learning solution for cryo-EM volume post-processing. Commun Biol. 2021;4:874.

[99] Emsley P, Cowtan K. Coot: model-building tools for molecular graphics. Acta Crystallogr D Biol Crystallogr. 2004;60:2126-32.

[100] Emsley P, Lohkamp B, Scott WG, Cowtan K. Features and development of Coot. Acta Crystallogr D Biol Crystallogr. 2010;66:486-501.

[101] Adams PD, Afonine PV, Bunkoczi G, Chen VB, Davis IW, Echols N, et al. PHENIX: a comprehensive Python-based system for macromolecular structure solution. Acta Crystallogr D Biol Crystallogr. 2010;66:213-21.

[102] Afonine PV, Klaholz BP, Moriarty NW, Poon BK, Sobolev OV, Terwilliger TC, et al. New tools for the analysis and validation of cryo-EM maps and atomic models. Acta Crystallogr D Struct Biol. 2018;74:814-40.

[103] DiMaio F, Echols N, Headd JJ, Terwilliger TC, Adams PD, Baker D. Improved low-resolution crystallographic refinement with Phenix and Rosetta. Nat Methods. 2013;10:1102-4.

[104] Pettersen EF, Goddard TD, Huang CC, Couch GS, Greenblatt DM, Meng EC, et al. UCSF Chimera--a visualization system for exploratory research and analysis. J Comput Chem. 2004;25:1605-12.

[105] Pettersen EF, Goddard TD, Huang CC, Meng EC, Couch GS, Croll TI, et al. UCSF ChimeraX: Structure visualization for researchers, educators, and developers. Protein Sci. 2021;30:70-82.

[106] Kelley LA, Mezulis S, Yates CM, Wass MN, Sternberg MJ. The Phyre2 web portal for protein modeling, prediction and analysis. Nat Protoc. 2015;10:845-58.

[107] Cowtan K. The Buccaneer software for automated model building. 1. Tracing protein chains. Acta Crystallogr D Biol Crystallogr. 2006;62:1002-11.

[108] Waterhouse A, Bertoni M, Bienert S, Studer G, Tauriello G, Gumienny R, et al. SWISS-MODEL: homology modelling of protein structures and complexes. Nucleic Acids Res. 2018;46:W296-W303.

[109] Sherpa D, Chrustowicz J, Qiao S, Langlois CR, Hehl LA, Gottemukkala KV, et al. GID E3 ligase supramolecular chelate assembly configures multipronged ubiquitin targeting of an oligomeric metabolic enzyme. Mol Cell. 2021;81:2445-59 e13.

[110] Chrustowicz J, Sherpa D, Teyra J, Loke M, Popowicz G, Basquin J, et al. Multifaceted N-degron recognition and ubiquitylation by GID/CTLH E3 ligases. Journal of Molecular Biology. 2021.

[111] Langlois CR, Beier V, Karayel O, Chrustowicz J, Sherpa D, Mann M, et al. A GID E3 ligase assembly ubiquitinates an Rsp5 E3 adaptor and regulates plasma membrane transporters. bioRxiv [Preprint].

[112] Shin JS, Park SH, Kim L, Heo J, Song HK. Crystal structure of yeast Gid10 in complex with Pro/N-degron. Biochem Biophys Res Commun. 2021;582:86-92.

[113] Cappell SD, Mark KG, Garbett D, Pack LR, Rape M, Meyer T. EMI1 switches from being a substrate to an inhibitor of APC/C(CDH1) to start the cell cycle. Nature. 2018;558:313-7.

[114] Davis M, Hatzubai A, Andersen JS, Ben-Shushan E, Fisher GZ, Yaron A, et al. Pseudosubstrate regulation of the SCF(beta-TrCP) ubiquitin ligase by hnRNP-U. Genes Dev. 2002;16:439-51.

[115] Manford AG, Rodriguez-Perez F, Shih KY, Shi Z, Berdan CA, Choe M, et al. A Cellular Mechanism to Detect and Alleviate Reductive Stress. Cell. 2020;183:46-61 e21.

[116] Miller JJ, Summers MK, Hansen DV, Nachury MV, Lehman NL, Loktev A, et al. Emi1 stably binds and inhibits the anaphase-promoting complex/cyclosome as a pseudosubstrate inhibitor. Genes Dev. 2006;20:2410-20.

[117] Welcker M, Larimore EA, Frappier L, Clurman BE. Nucleolar targeting of the fbw7 ubiquitin ligase by a pseudosubstrate and glycogen synthase kinase 3. Mol Cell Biol. 2011;31:1214-24.

[118] Winter N, Novatchkova M, Bachmair A. Cellular Control of Protein Turnover via the Modification of the Amino Terminus. Int J Mol Sci. 2021;22.

[119] Tasaki T, Sriram SM, Park KS, Kwon YT. The N-end rule pathway. Annu Rev Biochem. 2012;81:261-89.

[120] Balaji V, Hoppe T. Regulation of E3 ubiquitin ligases by homotypic and heterotypic assembly. F1000Res. 2020;9.

[121] Bauer A, Jagannathan V, Hogler S, Richter B, McEwan NA, Thomas A, et al. MKLN1 splicing defect in dogs with lethal acrodermatitis. PLoS Genet. 2018;14:e1007264.

[122] Nassan M, Li Q, Croarkin PE, Chen W, Colby CL, Veldic M, et al. A genome wide association study suggests the association of muskelin with early onset bipolar disorder: Implications for a GABAergic epileptogenic neurogenesis model. J Affect Disord. 2017;208:120-9.

[123] Skraban CM, Wells CF, Markose P, Cho MT, Nesbitt AI, Au PYB, et al. WDR26 Haploinsufficiency Causes a Recognizable Syndrome of Intellectual Disability, Seizures, Abnormal Gait, and Distinctive Facial Features. Am J Hum Genet. 2017;101:139-48.

[124] Hasegawa M, Parkos CA, Nusrat A. WD40 Repeat Protein 26 Negatively Regulates Formyl Peptide Receptor-1 Mediated Wound Healing in Intestinal Epithelial Cells. Am J Pathol. 2020;190:2029-38.

[125] Erlendsson S, Teilum K. Binding Revisited-Avidity in Cellular Function and Signaling. Front Mol Biosci. 2020;7:615565.

[126] Uckelmann M, Sixma TK. Histone ubiquitination in the DNA damage response. DNA Repair (Amst). 2017;56:92-101.

[127] Schapira M, Calabrese MF, Bullock AN, Crews CM. Targeted protein degradation: expanding the toolbox. Nat Rev Drug Discov. 2019;18:949-63.

[128] Bondeson DP, Smith BE, Burslem GM, Buhimschi AD, Hines J, Jaime-Figueroa S, et al. Lessons in PROTAC Design from Selective Degradation with a Promiscuous Warhead. Cell Chem Biol. 2018;25:78-87 e5.

[129] Smith BE, Wang SL, Jaime-Figueroa S, Harbin A, Wang J, Hamman BD, et al. Differential PROTAC substrate specificity dictated by orientation of recruited E3 ligase. Nat Commun. 2019;10:131.

[130] Inobe T, Fishbain S, Prakash S, Matouschek A. Defining the geometry of the two-component proteasome degron. Nat Chem Biol. 2011;7:161-7.

[131] Mattiroli F, Sixma TK. Lysine-targeting specificity in ubiquitin and ubiquitin-like modification pathways. Nat Struct Mol Biol. 2014;21:308-16.

[132] Boldt K, van Reeuwijk J, Lu Q, Koutroumpas K, Nguyen TM, Texier Y, et al. An organelle-specific protein landscape identifies novel diseases and molecular mechanisms. Nat Commun. 2016;7:11491.

[133] Huttlin EL, Bruckner RJ, Paulo JA, Cannon JR, Ting L, Baltier K, et al. Architecture of the human interactome defines protein communities and disease networks. Nature. 2017;545:505-9.

[134] Huttlin EL, Ting L, Bruckner RJ, Gebreab F, Gygi MP, Szpyt J, et al. The BioPlex Network: A Systematic Exploration of the Human Interactome. Cell. 2015;162:425-40.

[135] Mohamed WI, Park SL, Rabl J, Leitner A, Boehringer D, Peter M. The human GID complex engages two independent modules for substrate recruitment. EMBO Rep. 2021:e52981.

7. List of publications

- **Chrustowicz J***, Sherpa D*, Teyra J, Loke M, Popowicz G, Basquin J, Sattler M, Prabu JR, Sidhu SS, Schulman BA. Multifaceted N-degron recognition and ubiquitylation by GID/CTLH E3 ligases. J Mol Biol. 2021.

- Sherpa D*, **Chrustowicz J***, Qiao S, Langlois CR, Hehl LA, Gottemukkala KV, Hansen FM, Karayel O, von Gronau S, Prabu JR, Mann M, Alpi AF, Schulman BA. GID E3 ligase supramolecular chelate assembly configures multipronged ubiquitin targeting of an oligomeric metabolic enzyme. Mol Cell. 2021.

- Langlois CR, Beier V, Karayel O, **Chrustowicz J**, Sherpa D, Mann M, Schulman BA. A GID E3 ligase assembly ubiquitinates an Rsp5 E3 adaptor and regulates plasma membrane transporters. EMBO Rep. 2022.

- Qiao S, Langlois CR*, **Chrustowicz J***, Sherpa D*, Karayel O, Hansen FM, Beier V, von Gronau S, Bollschweiler D, Schäfer T, Alpi AF, Mann M, Prabu JR, Schulman BA. Interconversion between Anticipatory and Active GID E3 Ubiquitin Ligase Conformations via Metabolically Driven Substrate Receptor Assembly. Mol Cell. 2020.

* Authors contributed equally

8. Acknowledgments

First and foremost, I would like to express my deepest gratitude to my supervisor, Brenda Schulman, for always being there for me as an inspiring mentor and leader, providing continuous support in both my professional and private life. Thanks for teaching me how to be a good scientist and seek alternative approaches to every scientific problem. I could never have imagined a more thorough and fruitful PhD training.

I would like to thank Dawa Sherpa, for being an amazing lab partner with whom I shared the joy of many exciting discoveries.

Arno Alpi for numerous scientific discussions and bringing words of encouragement every day.

All members of the Schulman lab for advice and creating a great environment for doing science. I am incredibly grateful to Rajan Prabu for guidance with all aspects of the structural work and Joseph Kellermann for ensuring smooth operation of the department.

The staff of MPIB Biochemistry, Crystallography and CryoEM Facilities, especially Stephan Uebel, for teaching me the principles of many biophysical methods as well as Daniel Bollschweiler and Tillman Schäfer for assistance with cryoEM.

The members of my thesis advisory committee, Elena Conti and Michael Sattler, for critical comments and suggestions.

I was lucky to supervise two talented Master's students – Max Duennebacke and Melissa Loke. Thanks a lot for your contributions to the project!

My friends, Błażej and Asia, for being the ones I could always count on.

My parents for always believing in me and supporting me at all stages of my life.

And last but not least, my beloved wife and son – you have been an endless source of motivation and energy reinforcing me to overcome all the challenges of my PhD journey.